Master Thesis

Research and Development on Calibration of MEG II Gamma Ray Detector

（MEG II実験ガンマ線検出器の較正に関する研究開発）

Department of Physics, School of Science,
The University of Tokyo

35-186077
Kazuki Toyoda

31st, January, 2020

Abstract

It is the main interest in the field of particle physics to search for a clue to new physics. The MEG II experiment searches for the $\mu \to e\gamma$ decay, which can be observed only under new physics. High resolution detectors have been developed to measure the decay products precisely. A liquid xenon scintillator calorimeter measures the direction, energy and timing of the gamma ray. In order to achieve high resolution, precise calibration of photosensors and complete understanding of detector response are necessary.

In this thesis three topics on calibration of the gamma ray detector are discussed. First one is a general study on photosensor calibration methods. Two different methods of monitoring gain of silicon photomultipliers are discussed. One uses the statistical characteristics of the charge distribution, which is robust to noise. In the other method, gain variation is monitored by waveform shapes, which allows calibration without a special setup. The second one is calibration and monitoring of the photosensors in the liquid xenon calorimeter. The gain from both methods was confirmed to be correlated to the one obtained from the usual one-photoelectron method. The response of photomultiplier tubes in the calorimeter in operation were monitored by alpha rays and LED light with the precision of 4%, which satisfies the requirement. The problem of aging of the photomultiplier tubes was also solved by lowering the high voltage. The third one is about calibration of the detector response using gamma rays. A new pion beam detector is proposed and is being developed for a possible improvement in the most important calibration method for the liquid xenon calorimeter.

Contents

1 Preface **1**

I Introduction **2**

2 Physics of $\mu \to e\gamma$ **3**

2.1 Standard Model and New Physics . . . 3
2.2 Lepton Flavor Violation . . . 4
2.3 Theory of $\mu \to e\gamma$ Decay . . . 5
2.3.1 $\mu \to e\gamma$ in Standard Model . . . 5
2.3.2 $\mu \to e\gamma$ in New Physics . . . 6
2.4 $\mu \to e\gamma$ Search . . . 7
2.4.1 Signal . . . 7
2.4.2 Background . . . 8

3 MEG II Experiment **10**

3.1 MEG Experiment . . . 10
3.1.1 Beam . . . 10
3.1.2 Target . . . 12
3.1.3 COBRA Magnet . . . 12
3.1.4 Drift Chamber . . . 12
3.1.5 Timing Counter . . . 13
3.1.6 LXe Calorimeter . . . 13
3.1.7 Data Acquisition . . . 13
3.1.8 Result . . . 14
3.2 MEG II Experiment . . . 14
3.2.1 Target . . . 15
3.2.2 Cylindrical Drift Chamber . . . 15
3.2.3 Pixelated Timing Counter . . . 16
3.2.4 LXe Calorimeter . . . 17
3.2.5 Radiative Decay Counter . . . 19
3.2.6 Trigger and Data Acquisition . . . 19
3.2.7 Expected Sensitivity . . . 20

4 LXe Calorimeter **22**
4.1 Hardware . . . 22
4.1.1 Characteristics of LXe . . . 22
4.1.2 Photomultiplier Tube . . . 25
4.1.3 Silicon Photomultiplier . . . 27
4.2 Event Reconstruction . . . 32
4.2.1 Waveform Analysis . . . 32
4.2.2 Position Reconstruction . . . 35
4.2.3 Energy Reconstruction . . . 36
4.2.4 Timing Reconstruction . . . 36
4.3 Calibration . . . 37
4.3.1 Photosensor . . . 37
4.3.2 Cockcroft-Walton-Litheum Calibration . . . 42
4.3.3 Charge Exchange Calibration . . . 42
4.4 Status . . . 43

II Photosensor Calibration **45**

5 Comparison of Gain Monitoring Methods for SiPM **46**
5.1 Gain of SiPM . . . 46
5.2 Statistical Method . . . 46
5.2.1 Previous Study . . . 47
5.2.2 Validation Test . . . 48
5.2.3 Relation between Variance and Mean . . . 49
5.3 Waveform Method . . . 52
5.3.1 Previous Study . . . 52
5.3.2 Validation Test . . . 54
5.3.3 Application for SiPM . . . 55
5.4 Conclusion . . . 59

6 PMT Monitoring **60**
6.1 Pre-Engineering Run . . . 60
6.1.1 2018 . . . 60
6.1.2 2019 . . . 61
6.1.3 Readout Region . . . 61
6.1.4 Requirement . . . 62
6.2 Calibration Methods and Precision . . . 64
6.2.1 Alpha Ray . . . 64
6.2.2 LED . . . 65
6.3 Cause of Variation . . . 65
6.3.1 Effect of Magnetic Field . . . 65
6.3.2 Short-term Variation under Muon Beam . . . 66
6.3.3 Aging Caused by Muon Beam . . . 71

6.4 Gain Decrease 72
6.4.1 Expectation from MEG 72
6.4.2 Beam Rate Dependence 73
6.4.3 Gain Dependence 76
6.4.4 Discussion 76
6.5 Conclusion 78

III Calibration of Detector Response **79**

7 Improvement of Charge Exchange Calibration **80**
7.1 Motivation 80
7.2 Requirement 81
7.3 Scintillating Fiber 82
7.3.1 Concept 82
7.3.2 Particle Identification 83
7.3.3 Radiation Hardness 84
7.4 Active Target 88
7.4.1 Concept 89
7.4.2 Charge Exchange Reaction in Scintillator 91
7.4.3 Rate 91
7.4.4 Energy Spectrum 91
7.5 Test of Active Target 93
7.5.1 Purpose 93
7.5.2 Construction of Prototype 94
7.6 Conclusion 94

IV Conclusion **96**

8 Conclusion **97**
8.1 SiPM Gain Monitoring 97
8.2 PMT Monitoring during Pilot Run 97
8.3 Development of Pion Beam Detector 98

Acknowledgement **99**

Bibliography **105**

Chapter 1

Preface

Searching for a clue to new physics is the main interest in the field of particle physics. One of the most powerful ways of looking for a signature of new physics is the $\mu \to e\gamma$ search, and its physics overview is explained in Chapter 2. The MEG II experiment is the upgrade of the MEG experiment, which searched for the decay with the best sensitivity in the world, and they are explained in Chapter 3.

For the MEG II experiment, high resolution detectors have been developed to measure the decay products precisely. The dedicated detectors have been developed, and all the components will be ready in 2020 at the earliest.

The liquid xenon scintillator calorimeter (LXe Calorimeter) measures the direction, energy and timing of the gamma ray. The detector construction was finished in 2017, and the next step is to understand the detector response and to evaluate the performance. In order to achieve high resolution, precise calibration of photosensors and complete understanding of detector response are necessary. The detector and the calibration are explained in Chapter 4.

This study aims at developing the calibration methods of the MEG II LXe Calorimeter. In this paper some topics on the calibration are discussed. The first topic is a general study on photosensor calibration methods, and two different methods of monitoring gain of silicon photomultipliers are discussed in Chapter 5. The second is the calibration and monitoring of the photosensors in the LXe Calorimeter. The gain of photomultiplier tubes are monitored and their sustainability is discussed in Chapter 6. The third is about the overall calibration of the detector response. A new pion beam detector is proposed and is being developed for a possible improvement in the most important calibration method for the LXe Calorimeter. This is reported in Chapter 7.

The study is summarized and concluded in Chapter 8.

Part I

Introduction

Chapter 2

Physics of $\mu \to e\gamma$

In this chapter the physics and the motivation of the $\mu \to e\gamma$ search are described. In Sec. 2.1, the current status of the particle physics and methods of searches for new physics are introduced. One of the most powerful probes for new physics is the search for charged lepton flavor violation (cLFV) and it is explained in Sec. 2.2. Among some cLFV modes, the target of the MEG II experiment is $\mu \to e\gamma$ decay, whose physics and experimental characteristics are discussed in Sec. 2.3

2.1 Standard Model and New Physics

The theory of everything has been explored by particle physicists for years, and they established the Standard Model (SM). Although the SM explains low energy phenomena very precisely, it does not seem to be the complete theory. There are some experimental facts that cannot be explained by the SM such as the neutrino oscillation [1]. From the theoretical point of view, it contains some unnatural properties in itself such as the light Higgs mass and three generations of the fermion. Moreover, cosmological mysteries such as baryogenesis, dark matter and dark energy still remain to be solved.

Theorists have been trying to construct an improved theory which compensates for some cracks of the SM. Most of the new physics models contain some new particles, which have not been observed owing to their high energy scale or their small coupling to SM particles.

All we experimentalists have to do is to find the evidence of the new physics, or the non SM particles. One major approach is to search for the new particles directly, either by achieving the ultra low background from SM particles, or by producing a new particle artificially by colliding SM particles in very high energy. The other approach is to search for a small discrepancy of an observable from the prediction of the SM. Loop effects from a new particle can induce a deviation, or even bring about a prohibited reaction in the SM. A violation of a conservation law of the SM is one of the most effective tools because the SM background is highly suppressed. Lepton flavor conservation is such a representative conservation law of the SM and explained in detail in the next section.

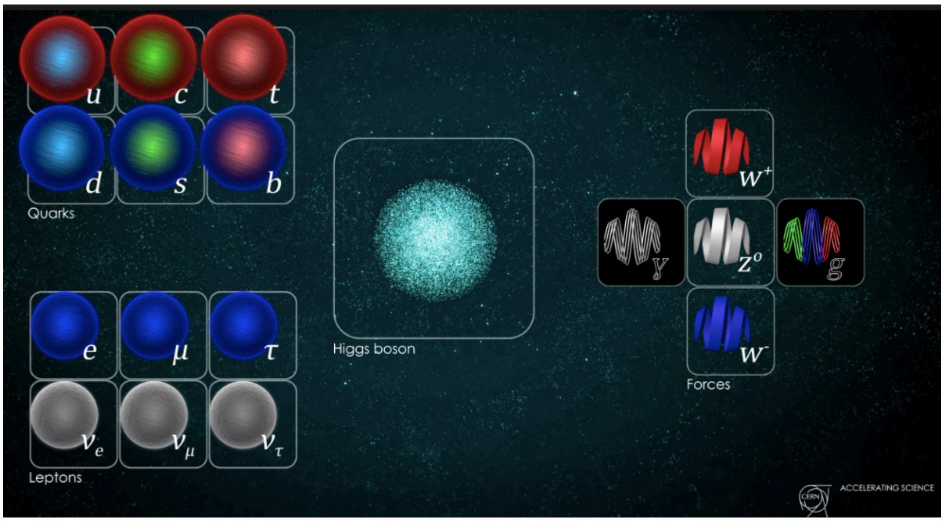

Figure 2.1: Elementary particles in the SM [2]. The particles in the left side are those which compose matter. Those in the left bottom are not subject to the strong interaction and called leptons.

2.2 Lepton Flavor Violation

Figure 2.1 shows the elementary particles in the SM. The particles in the left tables are those which compose matter and they are called fermions. They have three generations and each generation is represented as a column. The quarks are fermions which are subject to the strong interaction while the leptons do not interact by that interaction. In the SM, quarks can change between themselves over generations while leptons cannot do so. This property is called the lepton flavor conservation.

The lepton flavor conservation in the electrically neutral sector was found to be violated by the discovery of the neutrino oscillation [3]. The oscillation attributes to the existence of mass of neutral leptons, and it can also originate the violation of the charged lepton flavor conservation. However, a naive extension of the SM cannot make the charged lepton flavor violation (cLFV) in an observable scale because the masses of neutrinos are too small to mix the charged leptons enough, as discussed in the next section.

There are a number of extension models of the SM and some of them predict sizable violation of charged lepton flavor conservation. Although it depends on the size of the couplings or the details of each model, the search for cLFV can probe up to more than PeV scale physics as shown in Fig. 2.2. The reach is much higher than the future direct production experiment using high energy colliders.

The muon is a suitable object for a cLFV search. It can be easily produced becuase it is not so heavy. The physics processes are simple because it is not subject to the strong interaction. The most powerful historical search is the search for its rare decay $\mu \to e\gamma$, and explained in the next section.

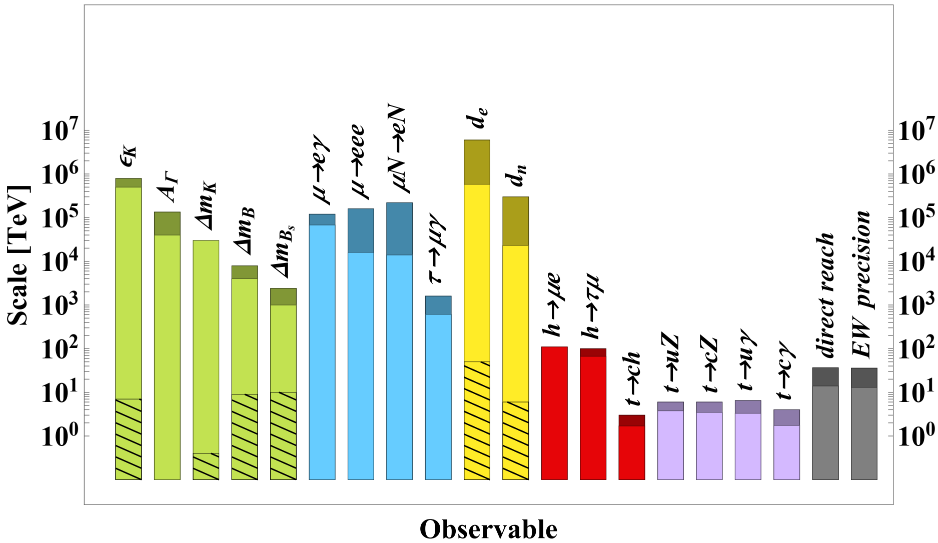

Figure 2.2: Reach in the new physics scale of various searches of current and future facilities estimated from generic six-dimensional operators [4]. The operator coefficients are taken to be either ~ 1 (plain colored) or suppressed by Minimal Flavor Violation factors (hatch filled). Light colors correspond to present data. Cancellations among higher-dimension operators or the effect of one-loop diagram mediated by SM particles are not taken into account. Some observables combine the insights from other flavor physics.

2.3 Theory of $\mu \to e\gamma$ Decay

2.3.1 $\mu \to e\gamma$ in Standard Model

In the minimal extended Standard Model, the main contribution to the $\mu \to e\gamma$ decay is the one-loop process caused by neutrino oscillation as shown in Fig. 2.3. This process is severely suppressed owing to the tiny masses of neutrinos, and so the branching ratio is

$$\mathcal{B}(\mu \to e\gamma) = \frac{3\alpha}{32\pi} \left| \sum_{i=2,3} U^*_{\mu i} U_{ei} \frac{\Delta m^2_{i1}}{M_W} \right|^2 < 10^{-50}, \tag{2.1}$$

where α is fine-structure constant, U_{ij} is the Pontecorvo-Maki-Nakagawa-Sakata matrix, Δm_{ij} is the mass difference of neutrinos, and M_W is the mass of the W boson [6]. This branching ratio is quite small compared to the experimental reach, and so the discovery of this process is direct evidence of the new physics.

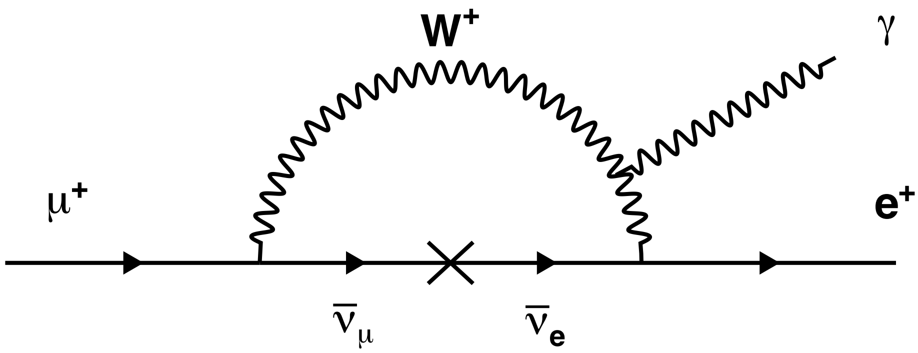

Figure 2.3: Feynman diagram of the $\mu \to e\gamma$ process in the minimal extended Standard Model [5].

2.3.2 $\mu \to e\gamma$ in New Physics

The SM Lagrangian can be extended as follows using the Effective Field Theory assuming only that the scale of the new physics is much larger than the electromagnetic scale [7];

$$\mathcal{L} = \mathcal{L}_{\mathrm{SM}} + \frac{1}{\Lambda}\sum_a C_a^{(5)} Q_a^{(5)} + \frac{1}{\Lambda^2}\sum_a C_a^{(6)} Q_a^{(6)} + \cdots , \tag{2.2}$$

where $\mathcal{L}_{\mathrm{SM}}$ is the Lagrangian of the SM, Λ is the energy scale of new degrees of freedom that give rise to the operators once integrated out, $C_a^{(D)}$ are dimensionless coefficients, and $Q_a^{(D)}$ are non-renormalizable operators. Since the operators with $D = 5$ can induce cLFV only at the loop level, the effects arise at the dimension-six level. Considering only dimension-six dipole operators for simplicity, the following expression for the decay rate can be obtained;

$$\Gamma(\mu \to e\gamma) = \frac{m_\mu^3 v^2}{8\pi\Lambda^4}(|C_{e\gamma}^{e\mu}|^2 + |C_{e\gamma}^{\mu e}|^2), \tag{2.3}$$

where m_μ is the muon mass and v is the vacuum expectation value of the Higgs field. Thus $\mu \to e\gamma$ can occur under new physics where the energy scale is relatively small or the coefficients of the relevant operators are large.

These parameters depend largely on each model. One of the main theoretical frameworks which motivates experimental efforts is the Supersymmetry (SUSY) models, which are attractive because they explain the Higgs naturalness problems. Under some of the SUSY models three kinds of (electromagetic, weak and strong) interactions are unified. SUSY combined with the seesaw mechanism can explain the origin of the observed small neutrino masses.

SUSY models enhance the $\mu \to e\gamma$ decay because neutrinos in the Fig. 2.3 can be replaced by SUSY particles and W bosons, and the suppression caused by the separation between the electromagnetic scale and the neutrino mass scale now disappears. The size of the cLFV effect caused by the SUSY has been studied in various models. Figure 2.4 shows branching

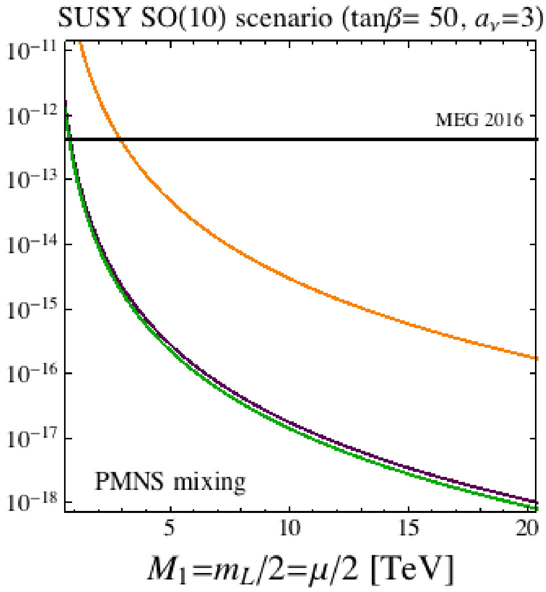

Figure 2.4: Rates of $\mu \to e$ processes predicted in a SUSY seesaw with large slepton mixing [7]. The orange line is the branching ratio of the $\mu \to e\gamma$ decay. The purple and green lines are the branching ratio of the $\mu \to eee$ and the conversion rate of $\mu N \to eN$, respectively. The parameters are chosen aiming at maximising the cLFV effects.

ratios expected from one of the SUSY models, SUSY-seesaw under SO(10) gauge symmetry. When choosing some parameters to maximize the cLFV effect, the MEG experiment has already explored new physics up to the SUSY scale of a few TeV, and the $\mu \to e\gamma$ decay can be observed at anytime by succeeding experiments. It shows the importance of increasing the precision of the $\mu \to e\gamma$ search to find the new physics.

2.4 $\mu \to e\gamma$ Search

2.4.1 Signal

Since $\mu \to e\gamma$ is a two-body decay, the decay products have the following signatures in the rest frame of the muon:

- coming out in the opposite directions
- being produced at the same timing
- having the same amount of momentum ($m_\mu/2$)

as shown in Fig. 2.5. These distinctive characteristics make it possible to distinguish a signal from SM decays of the muon.

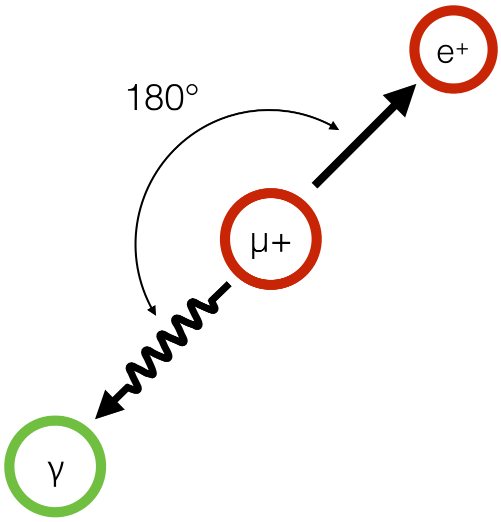

Figure 2.5: Kinematics of the signal event [5]. The decay particles are generated at the same timing and go to the opposite directions having the same amount of momentum.

2.4.2 Background

There are two kinds of backgrounds, a physical background and an accidental background.

Physics Background

The muon has a decay mode which emits both a gamma ray and an electron, $\mu \to e\nu\bar{\nu}\gamma$ (Fig. 2.6), which is called the Radiative Muon Decay (RMD). When the energy of the two neutrinos are small, this decay looks similar to the two-body decay signal. The branching ratio of the RMD is $(6.0 \pm 0.5) \times 10^{-8}$ when looking at the energy range of $E_e > 45$ MeV and $E_\gamma > 40$ MeV [8].

Accidental Background

Even when a gamma ray and an electron are not generated from a single source, they can imitate the signal when they accidentally fly in the opposite directions with the same amount of momentum at the same time. The most common source of an electron is the Michel decay of muons, which accounts for almost 100% of the muon decay branching ratio [9]. The gamma ray comes mainly from the following two sources. One is the RMD, which is also a source of the physics background. The other is the annihilation of positrons in flight of a positron generated by the Michel decay, which is depicted in Fig. 2.7. The decay positron can annihilate combining with an electron and generate a gamma ray in material such as a muon stopping target, detectors or beamline components.

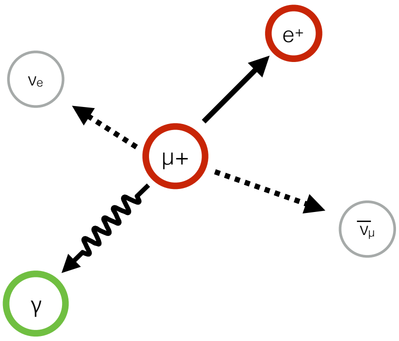

Figure 2.6: Kinematics of the physics background, the Radiative Muon Decay [5]. It can also be a gamma ray source of an accidental background.

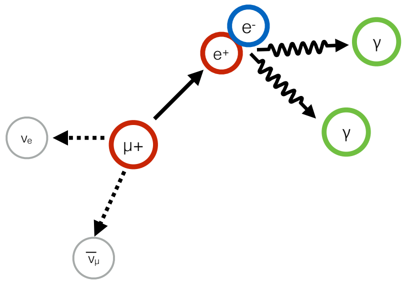

Figure 2.7: Kinematics of the annihilation in flight of the positron from a Michel decay [5].

The number of the accidental backgrounds N_{BG} can be written as follows [10];

$$N_{\mathrm{BG}} \propto R_\mu^2 \cdot \Delta E_\gamma^2 \cdot \Delta p_e \cdot \Delta\theta_{e\gamma}^2 \cdot \Delta t_{e\gamma} \tag{2.4}$$

where R_μ is the number of the muons decayed in unit time, E_γ is the energy of the gamma ray, p_e is the momentum of the positron, $\theta_{e\gamma}$ is the opening angle of the two decay particles, $t_{e\gamma}$ is the generation time difference between the gamma ray and the positron, and Δ represents the resolution of detectors for each variable. It is necessary to increase the statistics to improve the sensitivity with limited time, but the number of the background events increases with the square of the beam rate. Thus, detectors which have very high resolution are needed to effectively increase the statistics by utilizing a high rate beam.

Chapter 3

MEG II Experiment

3.1 MEG Experiment

The current best limit of the branching ratio of the $\mu \to e\gamma$ decay is set by the MEG experiment, which was operated from 2008 to 2013 at Paul Scherrer Institute (PSI) in Switzerland.

Figure 3.1 shows a schematic view of the experiment. Right-handed coordinate was defined so that the z axis coincided with the muon beam direction, and the y axis directed upward vertically. An antimuon beam was generated by a proton accelerator complex at PSI. An antimuon stopped at a plastic target and it decayed into some particles: positrons, gamma rays and neutrinos. Positrons flew in a spiral trajectory due to a gradient magnetic field created by the constant bending radius (COBRA) magnet. Positron tracks were recorded by the Drift Chamber and the timing is measured by the Timing Counter. Gamma rays were detected by the LXe Calorimeter after going through a thin aluminum window on the COBRA wall. All waveforms were recorded using waveform digitizers. Each component is briefly described below.

3.1.1 Beam

PSI has provided 590 MeV proton beam accelerated by the large proton cyclotron (Fig. 3.2). The current of the proton was 2.2 mA at maximum. The protons collided into a graphite target and generated positive pions. The pions decayed into antimuons through the reaction $\pi^+ \to \mu^+ + \nu_\mu$. When the pion was at rest when it decays, a completely polarized muon ($P_\mu = -1$) was generated whose momentum was 29.8 MeV/c. Those produced around the surface of the target selectively went into the πE5 beamline, and went through a separator and the Beam Transport Solenoid (BTS), and finally were stopped by a plastic target. They were unpolarized during this transportation, and their polarization became $P_\mu \simeq -0.85$ at the target [13]. Figure 3.3 shows a schematic view of the MEG beamline.

At the πE5 beamline the world's highest DC muon beam intensity was available. However, beam rate was reduced because the number of accidental backgrounds increases proportional to the square of the beam rate as discussed in Sec. 2.4.2, and it was better to operate at lower intensity considering the detector performance.

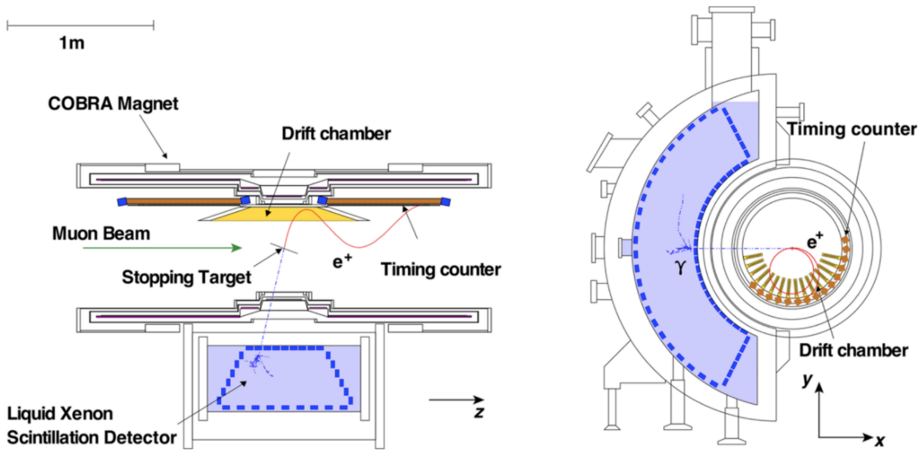

Figure 3.1: Schematic view of the MEG experiment [11]. Positrons and gamma rays generated from muons were detected using three different detectors: the Drift Chamber, the Timing Counter and the LXe Calorimeter.

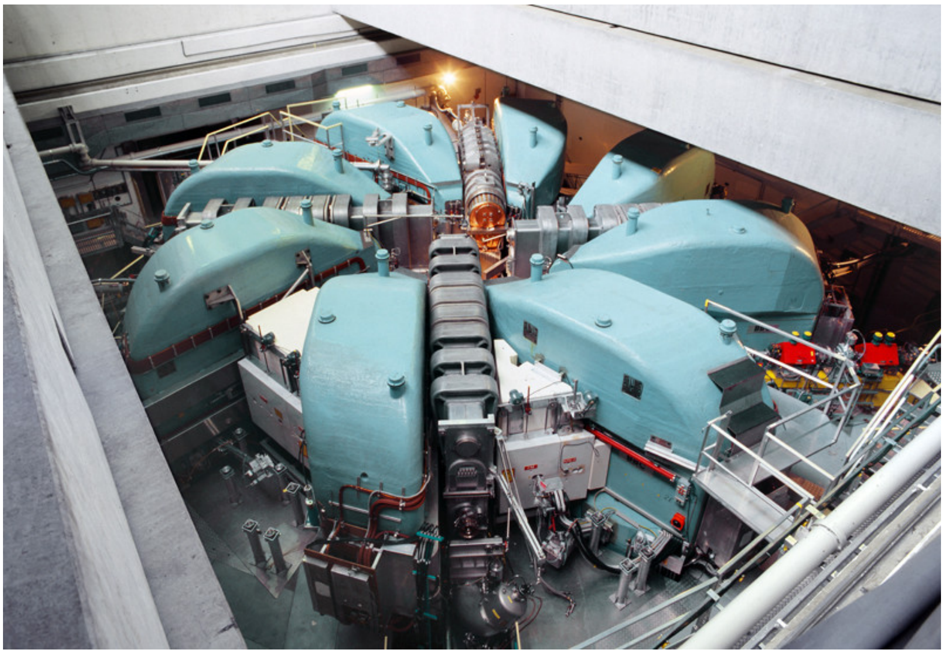

Figure 3.2: Large proton cyclotron at PSI. [12] It produces protons of which energy is 590 MeV and the current is 2.2 mA at maximum.

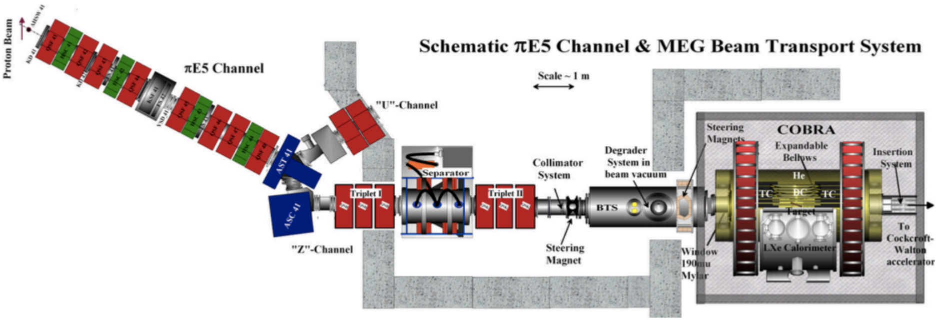

Figure 3.3: Schematic view of the MEG beamline [10]. Protons generated from a cyclotron were converted into pions and they decayed into muons. The muons were transported to the target through the πE5 beamline, a separator and the BTS.

3.1.2 Target

The target was 205 μm thick and has an elliptical shape. It was tilted by 20° to the beam axis in order to increase the muon stopping efficiency while suppressing interactions with the decay products.

3.1.3 COBRA Magnet

The COnstant Bending RAdius (COBRA) magnet was designed to make a gradient magnetic field which kept the radius of the positron constant independent of the emission angle at the target as schematically depicted in Fig. 3.4. Thus, the radius only depended on the positron momentum, and only those with the momentum around that of signal (52.8MeV/c) could reach the detectors. Positrons emitted almost perpendicular to the beam axis did not stay in the spectrometer and they were quickly swept away. This mechanism reduced the pileup in the spectrometer caused by the large number of Michel positron backgrounds.

The magnetic field strength was 1.27 T at the center and 0.5 T at each end. The photomultiplier tubes (PMTs) used in the LXe Calorimeter were affected by the magnetic field. Therefore there were compensation coils which reduced the magnetic field around the calorimeter to under 5 mT.

3.1.4 Drift Chamber

Positron tracks were recorded by the Drift Chamber. Gas in the chamber was ionized by a positron and charge was induced to wires. Sixteen drift chambers were installed inside the COBRA magnet and wires were stretched parallel to the beam axis. The signals were read out by anode wires and zigzag-shaped cathode pads.

The chambers are placed a little away from the beam axis in order to avoid pileups from low momentum Michel positrons which flew in a small radius region.

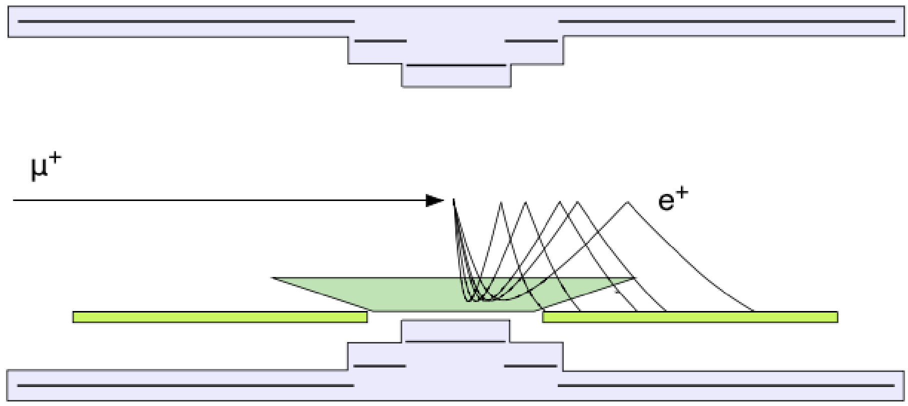

Figure 3.4: Schematic view of the cross section of the COBRA magnet and the positron spectrometer [14]. The gradient magnetic field made the radius of the positron track independent of the emission angle.

3.1.5 Timing Counter

The time of the positron was measured by the Timing Counter. It was made of 80 cm long plastic scintillator bars. The scintillation photons were read out by fine-mesh PMTs attached at either side of the scintillator bars. Thirty bars were installed just outside the Drift Chamber and inside COBRA magnet, and the bars measured the azimuthal angle of a positron hit discretely. The position in the beam direction was measured by the time difference between the PMTs at either side. The information about the reconstructed positions was used to match each hit with the Drift Chamber track.

3.1.6 LXe Calorimeter

The gamma ray detection is the key for the background reduction because the number of accidental backgrounds is proportional to the square of the energy and position resolution of the gamma ray as shown in Eq. (2.4). In the MEG experiment, LXe was used as a scintillator and PMTs detected the scintillation photons. The main component of the calorimeter was 900 L LXe and it was stored in a C-shaped cryostat shown in Fig. 3.5, which covered 11% of the solid angle from the target. The PMTs are on all of the 6 inner faces: inner, outer, lateral (upstream and downstream), top and bottom. The detail will be explained in Chap. 4 because the gamma ray detector of the MEG II experiment, which is the main topic of this thesis, is based on this MEG LXe Calorimeter.

3.1.7 Data Acquisition

A fast waveform digitizer was utilized in the MEG experiment, because pileup identification was important under the high intensity muon beam. The digitizer is named Domino Ring Sampler (DRS).

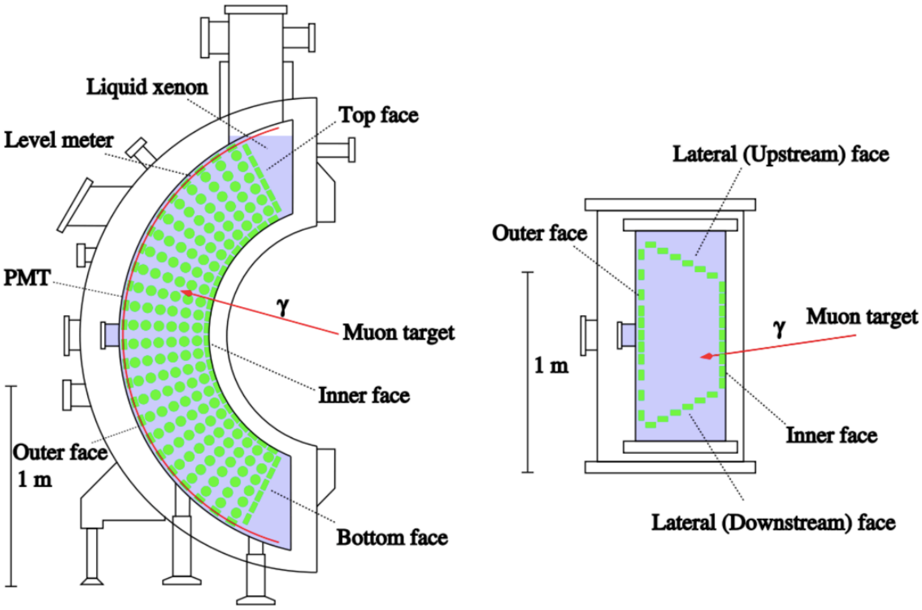

Figure 3.5: Outlook of the LXe Calorimeter [14]. It has a unique C-shape to cover a large solid angle.

Fig. 3.6 shows the principle of the DRS. The voltage information is sampled in high speed and the sampling signals transfer through the inverter delay chain circle. When a trigger signal is input, the rotation of the signals stops and the voltage value is sequently read out by a shift resister. The sampling frequency can be chosen from 0.5 GHz to 5 GHz. The LXe Calorimeter and the Timing Counter, which were responsible for the timing measurement, used 1.6 GHz sampling, and the Drift Chamber used 0.8 GHz.

The MIDAS system [16] was used as a data acquisition system.

3.1.8 Result

During the physics run period from 2008 to 2013, 7.5×10^{14} muons were stopped at the target [11]. A blind and maximum likelihood analysis resulted in the null consistent number of signals, and the world best upper limit was set on the branching ratio: $\mathcal{B}(\mu \to e\gamma) < 4.2 \times 10^{-13}$ (90% C.L.) [11], while the sensitivity was estimated to be 5.3×10^{-13}. The main source of the systematic uncertainty was the target deformation. It degraded the sensitivity by about 13% while the total contribution of the other systematics were less than 1%.

3.2 MEG II Experiment

The MEG collaboration decided to terminate the MEG experiment in 2013 and to concentrate on the upgrade of the experiment because they considered it inefficient to continue

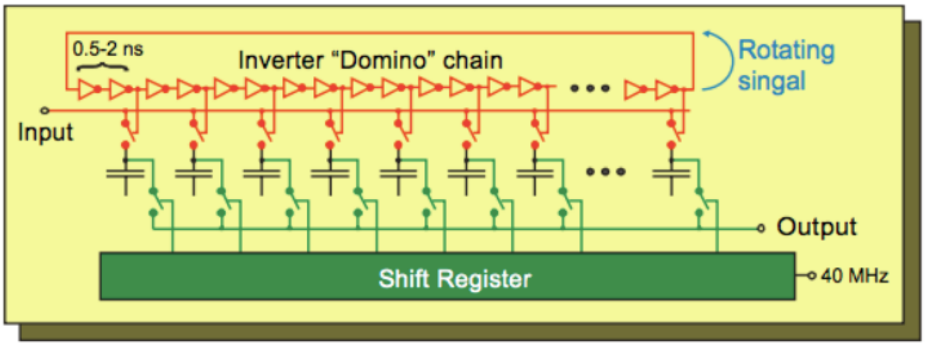

Figure 3.6: Principle of DRS [15]. Rotating inverter chain stores the voltage in condensers, and it is read out by a shift resister.

it with the reduced muon beam rate. The upgraded experiment was named the MEG II experiment and the key point of this upgrade is to utilize the full muon beam intensity. The muon stopping rate at the target will reach 7×10^7 μ/s, which is more than twice larger than that in the MEG experiment. As discussed in Sec. 2.4.2, the number of accidental background is proportional to the square of the beam rate. In order to overcome this problem, the resolution of each measured variable is supposed to be twice better than in the MEG experiment. The detectors also have to become robust aginst the increase of pileup events. The upgrade of each components is summarized below.

3.2.1 Target

The MEG II stopping target is made of a scintillating plastic film with the average thickness of 174 μm, and it is placed at 15.0° to the beam axis. The smaller thickness and angle reduce the material budget. Stopping efficiency is maximized by adjusting the beam degrader thickness.

The main source of the systematic uncertainty of the MEG experiment was the vertex estimation resulting from the target distortion. Therefore, two cameras are installed for the monitoring of the target shape in the MEG II experiment, and the deformation will be monitored by the dots printed on the target. Figure 3.7 is the picture of the target and the two cameras in the beamline.

3.2.2 Cylindrical Drift Chamber

In the MEG experiment, positron detection efficiency was reduced by scattering of the positrons by the mechanical frame or the electronics of the Drift Chamber before entering the Timing Counter. For the MEG II experiment a single-volume drift chamber, the Cylindrical Drift Chamber, has been developed and there is no unnecessary material between the Cylindrical Drift Chamber and the timing counter. The length of the chamber is 193 cm and the inner (outer) radius is 17 cm (29 cm). The stereo angle structure of the wires provides

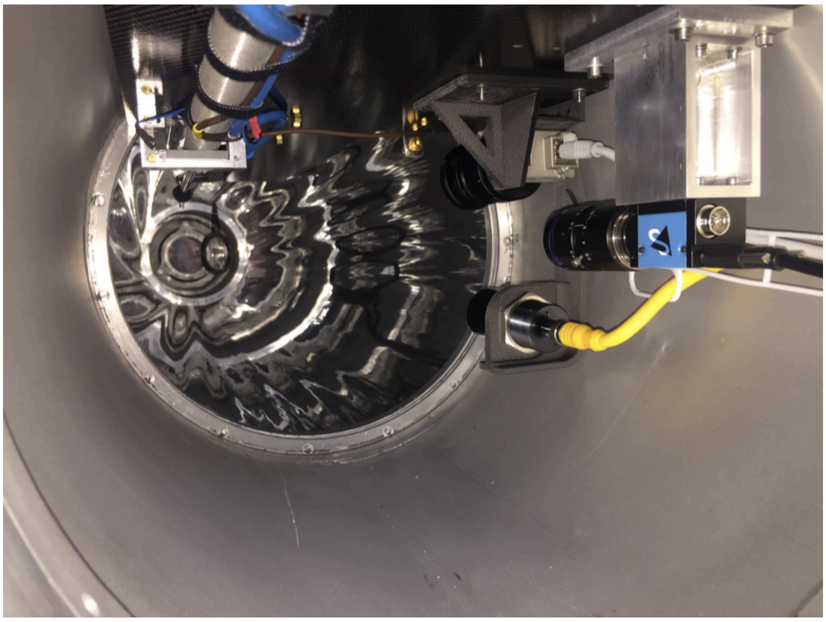

Figure 3.7: Picture of the target and the two cameras installed in the beamline [17].

the position information along the beam axis. The hyperbolic shape due to the stereo angle wiring is visible in Fig. 3.8. It can endure the high rate backgrounds owing to the small drift cells (6.6–9 mm). In a cell a 20 μm-diameter gold-plated W sense wire is surrounded by 40 μm-diameter silver-plated Al field wires. A radiation length per track turn is $1.58 \times 10^{-3} X_0$ when the chamber is filled with a gas mixture of helium and isobutane in the ratio 90:10, compared to $2.0 \times 10^{-3} X_0$ in the MEG experiment.

It was mounted inside COBRA magnet in 2018, and the stability of the current under the intense muon beam is studied with the limited number of readout channels in 2019.

3.2.3 Pixelated Timing Counter

The scintillators used for the Timing Counter of the MEG experiment was so large that there was large variation of the optical photon paths, leading to worse resolution. It would also lead to more pileups if it was used in the higher rate environment.

The timing of the positron is measured by the Pixelated Timing Counter in the MEG II experiment. Each counter is made of a small plastic scintillator read out by series-connected 6 SiPMs at either side. The size of each counter is (40 or 50) $\times$ 120 $\times$ 5 mm^3. The timing resolution of a single counter is about 80 ps [10]. One module consists of 256 counters as shown in 3.9 and it was placed at each of the upstream and the downstream side of the target. By measuring the timing by 9 counters per track on average, even better timing resolution can be achieved. The measured resolution at a pilot run in 2017 was 38.5 ps [18]. The pixelated structure also enables the operation under a large number of backgrounds because there are a small number of pileups at each counter. This structure also enables the tracking of the positron only by the Timing Counter itself, possibly resulting in the improvement of

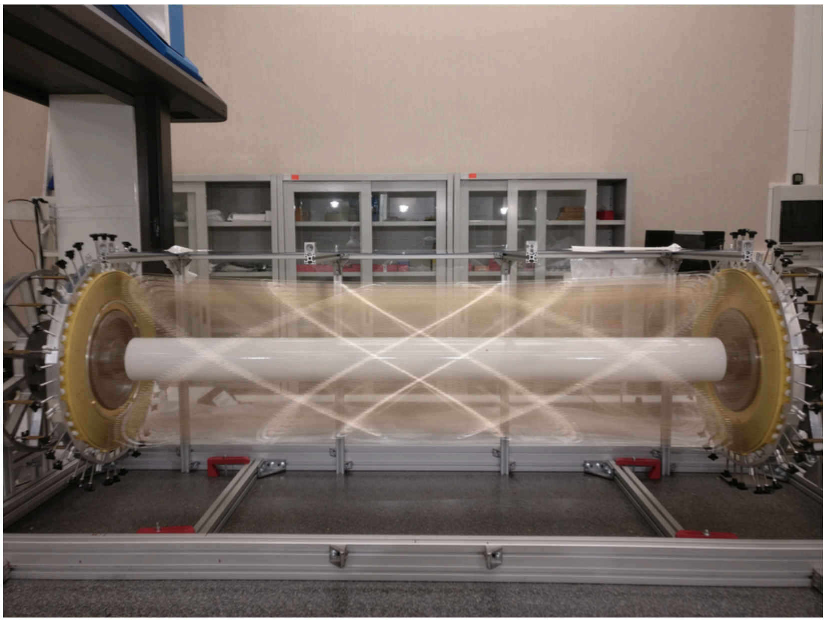

Figure 3.8: Cylindrical Drift Chamber of the MEG II experiment [10]. There is no unnecessary material in the path to the Pixelated Timing Counter.

the matching efficiency with the Cylindrical Drift Chamber.

3.2.4 LXe Calorimeter

The largest change of the gamma ray detector from the MEG experiment is the photosensors at the gamma ray incident face. In the MEG experiment, gamma rays which converted in the shallow region had worse resolution than those in the deep region on account of the non-uniformity caused by large PMTs. The MEG II experiment employs smaller sensors, silicon photomultipliers (SiPMs), at the incident face. The sizes can be compared with each other in Fig. 3.10 which shows inside the calorimeter. The SiPM is only 15×15 mm^2 while the PMT is 57 mm in diameter. The uniformity improves by placing sensors with smaller gaps, which leads to the better energy resolution for shallow events and twice better position resolution. Furthermore, the high granularity will also improve the performance of the pileup identification. Owing to the decrease of the amount of material at the incident face, the detection efficiency of the gamma rays is expected to become higher by absolutely about 5% than the MEG experiment.

Another upgrade is the change in the placement of the photosensors. The incident face has become wider by 10% in the beam direction, which reduces the energy leakage for events near the lateral face. The PMTs on the lateral faces are tilted so that all the photocathodes will lie in the same plane, which minimizes the effect of the fluctuation in the electromagnetic shower development.

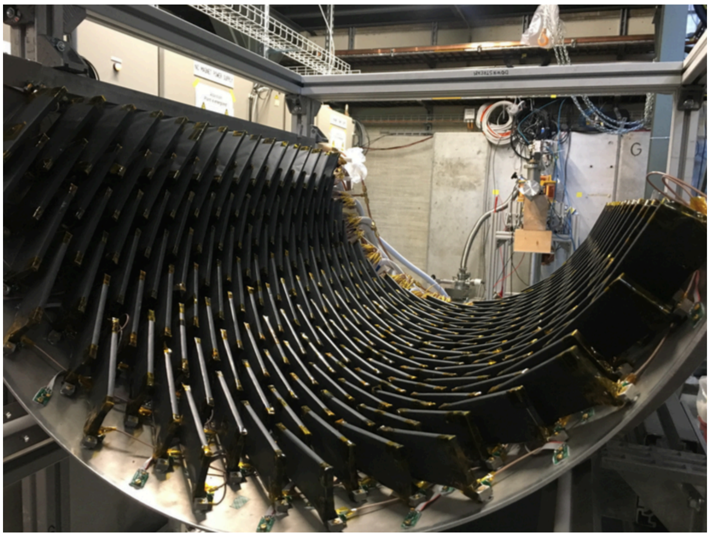

Figure 3.9: Pixelated Timing Counter of the MEG II experiment. The pixelated configuration reduces the pileups, improves the resolution, and enables the self tracking.

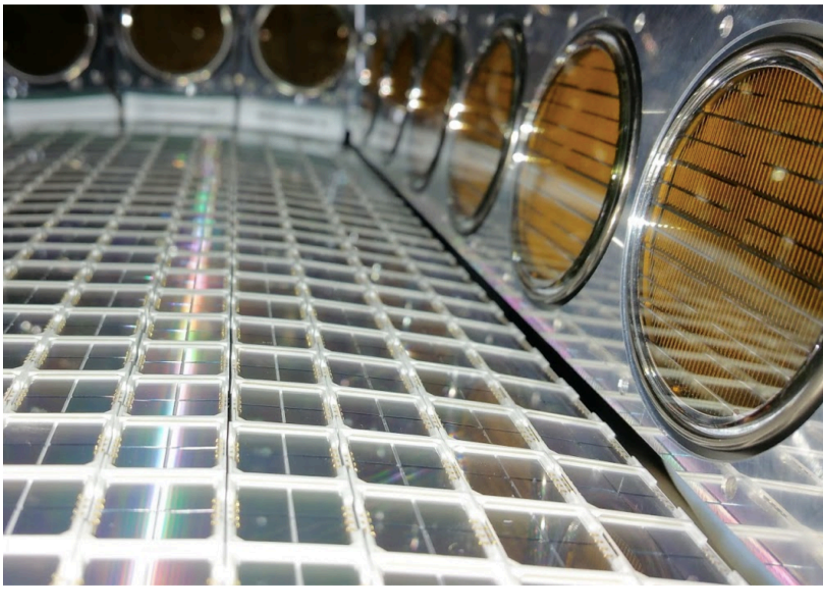

Figure 3.10: Inside of the LXe Calorimeter of the MEG II experiment. The PMTs on the incident face (bottom of this picture) are replaced with small SiPMs.

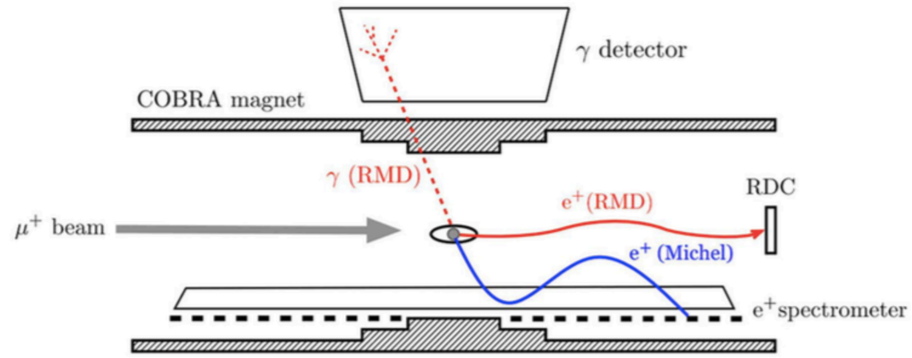

Figure 3.11: Concept of the RMD active detection [10]. The low energy positron from the RMD is be detected by a counter put on the beam axis.

3.2.5 Radiative Decay Counter

A radiative decay counter is newly introduced in the MEG II experiment for the purpose of the active detection of the RMD background events, which are the main source of a gamma ray background. RMD emits a positron whose energy is around 3 MeV, corresponding to the gamma ray which has energy similar to that of the signal (52.8 MeV). This low energy positron is trapped around the beam axis owing to the magnetic field produced by the COBRA magnet. Therefore, a detector put on the beam axis can detect the RMD positrons selectively as schematically depicted in Fig. 3.11. A low energy positron detected simultaneously with a gamma ray will be recognized as the RMD positron.

The half of the RMD positrons go toward upstream. The upstream counter must be put on the muon beam path in order to detect low energy positrons. On account of the difficulty in avoiding the interaction with muon beam, development of only the downstream side counter has been already finished. It consists of two parts, a timing counter made of 12 plastic scintillators, and a calorimeter made of 76 Lutetium Yttrium Orthosilicate (LYSO) crystals, as shown in Fig. 3.12. The photons are read out by SiPMs. The timing information is used to take a coincidence with the gamma ray signal, and the energy information is used to distinguish lower energy RMD events from higher energy Michel events.

3.2.6 Trigger and Data Acquisition

Owing to the higher segmentation of each detector, signals from about 9000 channels must be read out, which are three times more than those in the MEG experiment. Channels for SiPMs should have the function of a high voltage supply. In addition, a flexible amplification was necessary for SiPMs because small gain is used to observe gamma ray signals without saturation while large gain is needed for calibration by a single-photoelectron peak explained in Sec. 4.3.1.

For these reasons, the WaveDAQ system has been developed for the MEG II experiment. It is an integrated system of triggering and data acquisition. The DRS4 based readout module

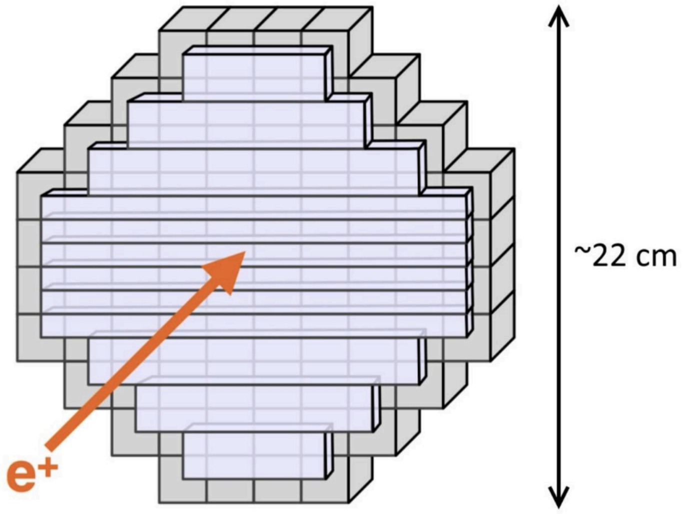

Figure 3.12: Schematic image of the radiative decay counter in the downstream side [10]. A timing counter made of plastic scintillators is in front of a calorimeter which consists of LYSO crystals.

(WaveDREAM) boards are used for data acquisition, and they have several components such as amplifiers, DRS chips, shapers and a high voltage source. The gain of the amplifier can be chosen from 0.5 to 100. Sixteen channels are read out by one board, and 16 boards are put in one crate. They are synchronized within 20 ps over different crate modules [19]. The MIDAS system [16] is used as a data acquisition system.

3.2.7 Expected Sensitivity

The expected performance of the MEG II detector is shown in Tab. 3.1. Based on this performance evaluation, the 90% confidence level sensitivity of the $\mu \to e\gamma$ branching ratio is calculated as a function of the data acquisition time as shown in Fig. 3.13. After three years operation, the sensitivity will reach 6×10^{-14}.

Table 3.1: Expected performance of the MEG II detectors [10].

parameter		MEG	MEG II
energy resolution of e^+	σ_{E_e}	306 keV	130 keV
angular resolution of e^+ at target	σ_{θ_e}, σ_{e_ϕ}	9.4 mrad, 8.7 mrad	5.3 mrad, 3.7 mrad
position resolution of e^+ at target	$\sigma_{\boldsymbol{x}_e}$	1.2 mm, 2.4 mm	0.7 mm, 1.6 mm
energy resolution of γ (at deep, at shallow)	$\sigma_{E_\gamma}/E_\gamma$	1.7%, 2.4%	1.0%, 1.1%
position resolution of γ conversion point	σ_u, σ_v, σ_w	5 mm, 5 mm, 6 mm	2.6 mm, 2.2 mm, 5 mm
resolution of decay time difference	$\sigma_{t_{e\gamma}}$	122 ps	84 ps
detection efficiency of γ	ϵ_γ	63%	69%
detection efficiency of e^+	ϵ_{e^+}	30%	70%

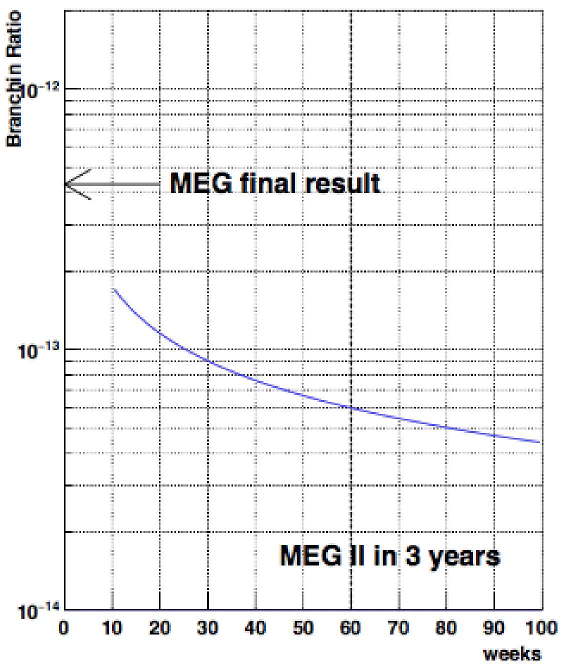

Figure 3.13: Sensitivity for the branching ratio of $\mu \to e\gamma$ decay [10]. 6×10^{-14} is expected after three years operation.

Chapter 4

LXe Calorimeter

Since the studies in this thesis aims at the improvement of the performance of the gamma ray reconstruction, the gamma ray detector is explained in more detail here. The first section is about the hardware. The event reconstruction is explained in the next section. The calibration, which is necessary for the proper reconstruction and is the main topic of this study, is explained in the third section.

4.1 Hardware

The gamma ray detector of the MEG II experiment is a LXe scintillation calorimeter, and scintillation photons are read out by PMTs and SiPMs located on the inner wall.

4.1.1 Characteristics of LXe

LXe is an optimal scintillator for the MEG experiment. The basic properties of LXe is summarized in Tab. 4.1.

The advantages of LXe as a scintillator are as follows;

- uniformity
- no self absorption

Table 4.1: Characteristics of LXe.

atomic number	54
atomic weight	131.293 [9]
density	2.98 g/cm^3 [20]
radiative length	2.77 cm [9]
W value for electron	21.6 eV/photon [21]
W value for α particle	19.6 eV/photon [22]
wavelength of scintillation light	174.8 nm [23]
Rayleigh scattering length	45 cm [24]

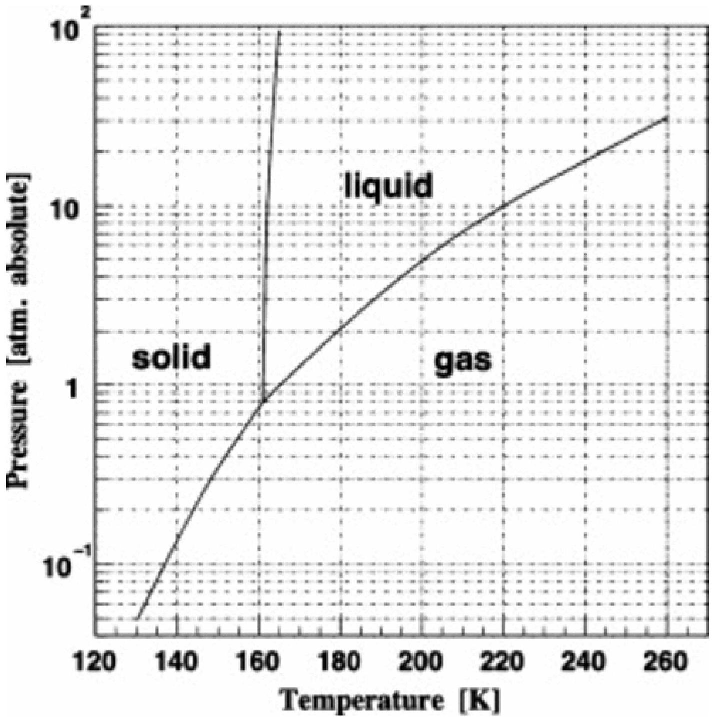

Figure 4.1: Phase diagram of the LXe [25]. A careful operation is needed to keep the liquid phase.

- short radiation length (2.77 cm)
- short time constant for gamma ray (45 ns)
- particle identification by waveforms

In contrast, following concerns should be carefully treated;

- necessity of being kept in low temperature (165 K)
- short wavelength of the scintillation photon (175 nm)
- short Rayleigh scattering length (45 cm)
- change of properties such as a light yield and light propagation by impurity

As shown in Fig. 4.1 the pressure and the temperature must be kept in a quite narrow region in the phase diagram in order to keep the liquid phase. For example, the temperature should be kept between 161 K and 165 K at 1 atom. Figure 4.2 shows that the absorption length is quite sensitive to the impurity.

When an energetic particle interacts with xenon, xenon atoms can be excited or ionized [27]. The excitation leads to fast scintillation. The excited xenon atom combines to

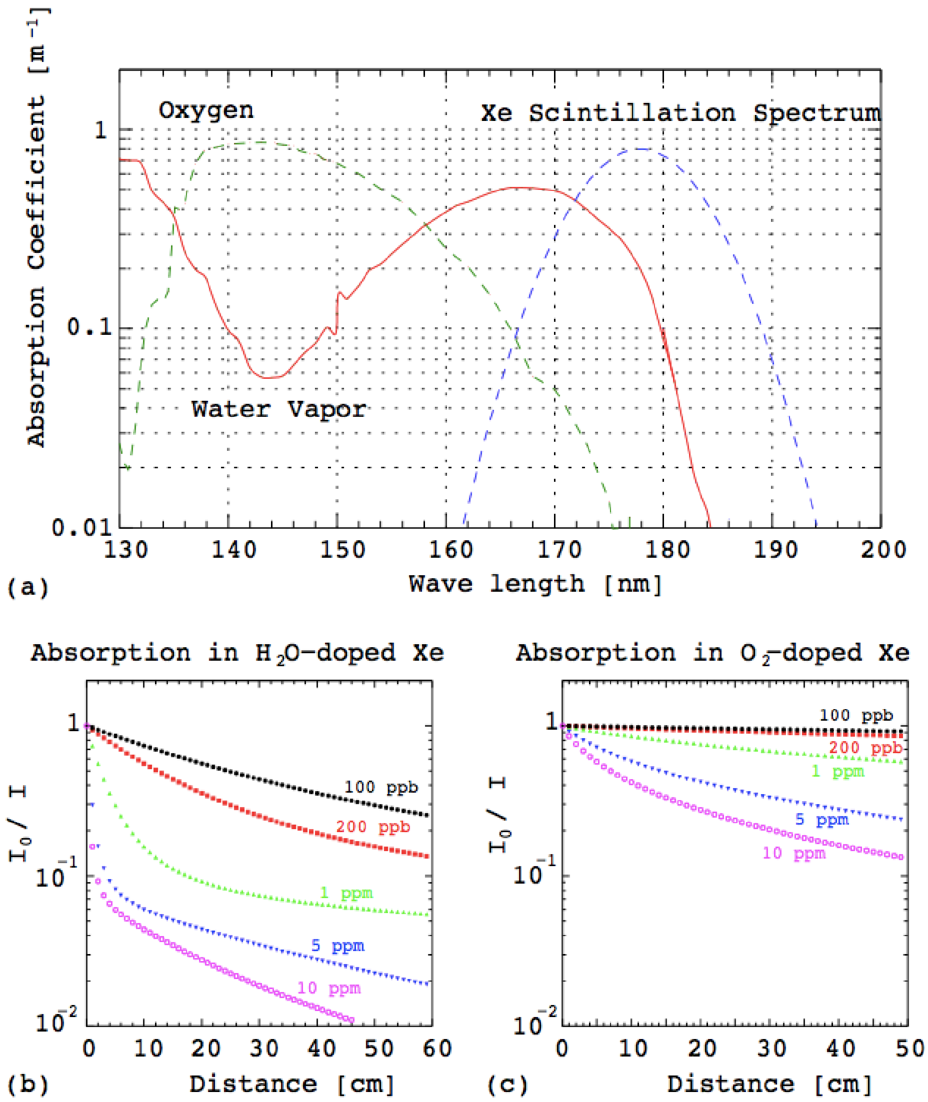

Figure 4.2: Effect of impurity on the absorption length of LXe [26]. The absorption length becomes comparable with the detector size especially when large amount of H_2O is contaminated.

Table 4.2: Basic properties of the PMT used in the MEG II experiment (R9869) [29].

size	57 mmϕ
size of sensitive area	45 mmϕ
length	32 mm
material of photocathode	K-Cs-Sb
type of dynode	metal channel
number of dynode	12

another atom to make excited molecular state. This state immediately de-excites and emits a scintillation photon;

$$\mathrm{Xe}^* + \mathrm{Xe} + \mathrm{Xe} \to \mathrm{Xe}_2^* + \mathrm{Xe}, \tag{4.1a}$$

$$\mathrm{Xe}_2^* \to 2\mathrm{Xe} + h\nu. \tag{4.1b}$$

On the other hand, the ionization leads to slow scintillation. Although the ionized xenon also finally results in the emission of a scintillation photon, the process chain is more complicated than that of the excited xenon atom.

$$\mathrm{Xe}^+ + \mathrm{Xe} \to \mathrm{Xe}_2^+, \tag{4.2a}$$

$$\mathrm{Xe_2}^+ + e^- \to \mathrm{Xe}^{**} + \mathrm{Xe}, \tag{4.2b}$$

$$\mathrm{Xe}^{**} \to \mathrm{Xe}^* + \mathrm{heat}, \tag{4.2c}$$

$$\mathrm{Xe}^* + \mathrm{Xe} + \mathrm{Xe} \to \mathrm{Xe}_2^* + \mathrm{Xe}, \tag{4.2d}$$

$$\mathrm{Xe}_2^* \to 2\mathrm{Xe} + h\nu. \tag{4.2e}$$

The fraction of these processes depends on the size of the energy deposit in unit volume, and different depending on the particle as shown in Fig. 4.3. The alpha ray deposits large energy in unit volume and it makes fast scintillation, whose time constant is 4.2 ns or 22 ns. The gamma ray generates electrons in LXe and they deposit smaller energy in unit volume. It makes slow scintillation, whose time constant is 45 ns. This difference in the scintillation time constant enables particle identification. Since the final process is the same as that of the excitation case, the wavelength of the scintillation light is the same.

4.1.2 Photomultiplier Tube

The photomultiplier tubes (PMTs) for the MEG experiment were developed with Hamamatsu photonics [28] to have enough sensitivity for the scintillation photons from xenon whose wavelength is around 175 nm. The basic properties is shown in Tab. 4.2. The window of the PMT is synthetic quartz glass and it is transparent for the wavelength down to 160 nm. The transmittance for the xenon scintillation wavelength (175 nm) is about 80%. To keep high quantum efficiency even at LXe temperature (165 K), an aluminum strip pattern is printed on the photocathode as can be seen in Fig. 4.4, which keeps low surface resistance. The metal channel dynode structure realizes the fast response and the compactness, and it enables the operation under the COBRA magnetic field (50 Gauss).

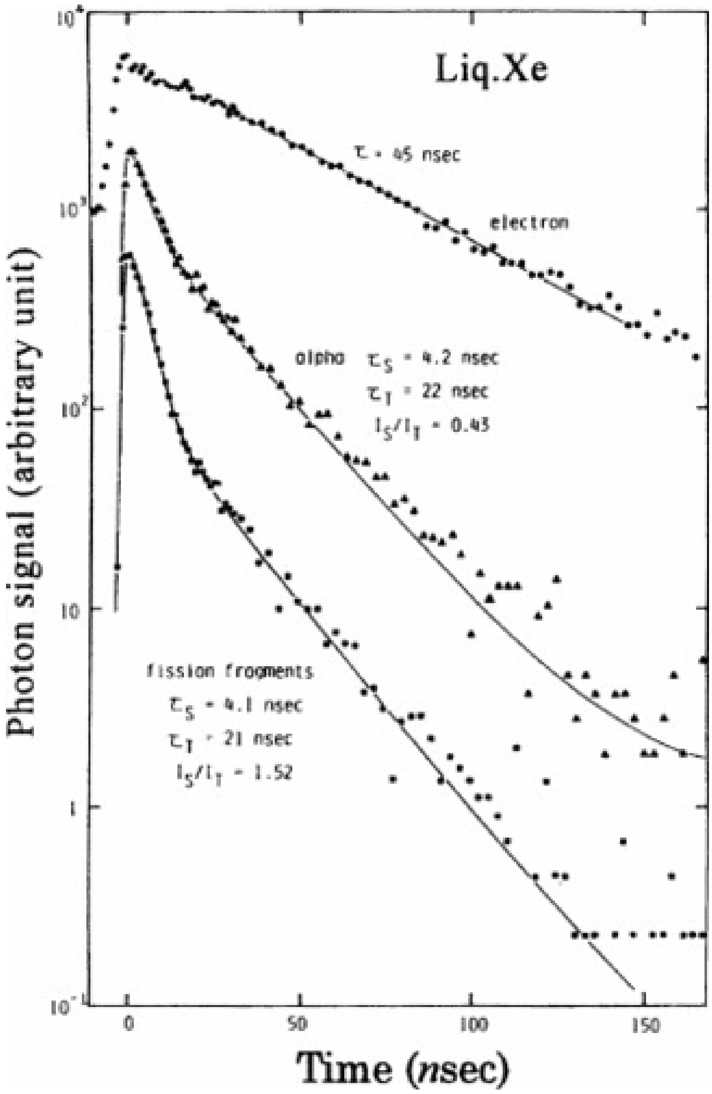

Figure 4.3: Time constant of the scintillation of LXe [27]. The response to alpha particles is fast while that to electrons are slow.

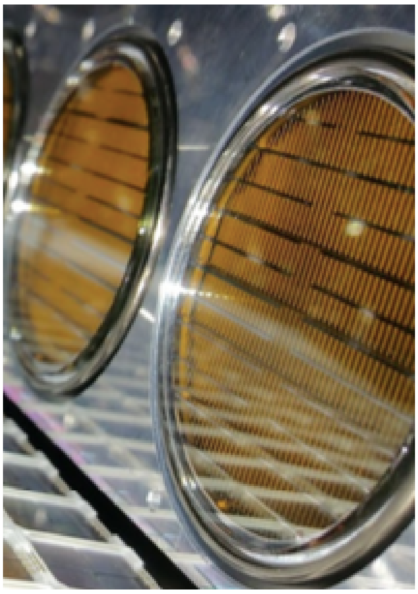

Figure 4.4: PMT used in the LXe Calorimeter (R9869). An Aluminum strip pattern maintains high quantum efficiency even at low temperature.

The divider circuit is shown in Fig. 4.5. Two Zener diodes play a role in keeping the voltage applied to the latter dynodes constant. It prevents from the voltage drop caused by large current, and the uniform distribution of the voltage between the dynodes is secured even under high rate signals.

4.1.3 Silicon Photomultiplier

In the MEG II experiment, silicon photomultipliers are newly introduced to increase the granularity and the uniformity of the photon detection on the gamma ray incident face.

Operating Principle

A SiPM is a kind of semiconductor photon detector. By applying inverse bias voltage on p-n junction, a depletion layer is made. The photon entering the layer makes an electron-hole pair and it works as the seed of the signal. This electron is also called photoelectron. The photoelectron is accelerated by the electric field and make an avalanche multiplication. During the multiplication process, electrons and holes collide with the lattice of the silicon crystal, and new electron-hole pairs are sequently produced. SiPMs work in the Geiger mode and the operating voltage is larger than the breakdown voltage. The operation under the Geiger mode results in multiplication whose gain is about 10^6, and it is called a Geiger discharge. The principle of an avalanche multiplication is schematically depicted in Fig. 4.6.

In order to control the multiplication, each pixel is connected in series to a quenching resister (Fig. 4.7), which makes the voltage drop and finishes the multiplication. Since each

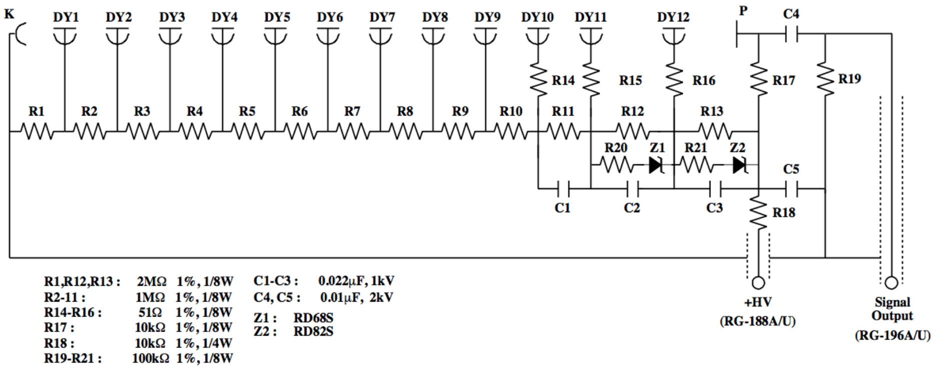

Figure 4.5: Divider circuit for the PMT [29]. Two Zener diodes (Z1 and Z2) keep the voltage distribution uniform even under the high rate beam.

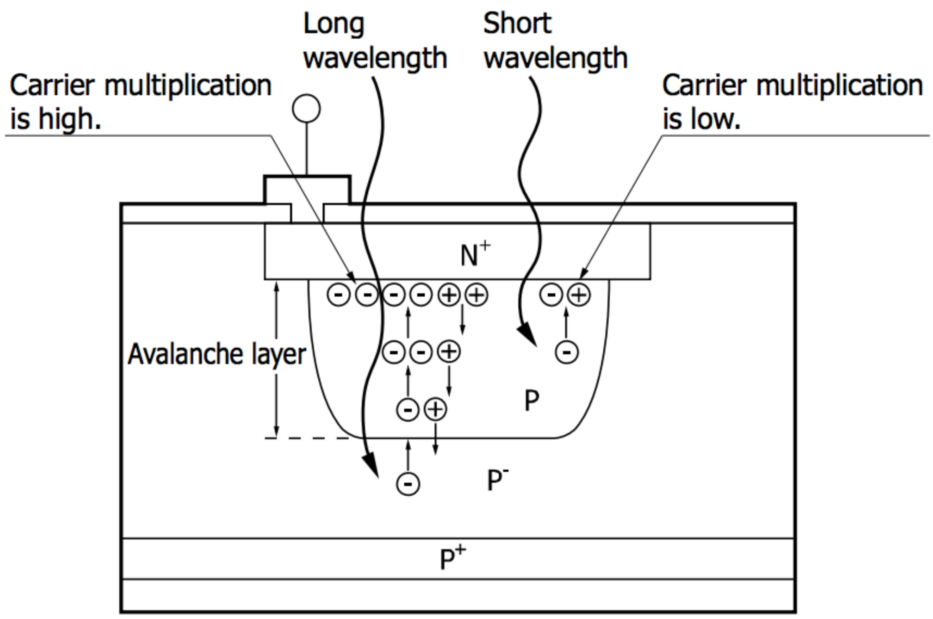

Figure 4.6: Visualization of an avalanche multiplication [30]. An avalanche is caused in a depletion layer.

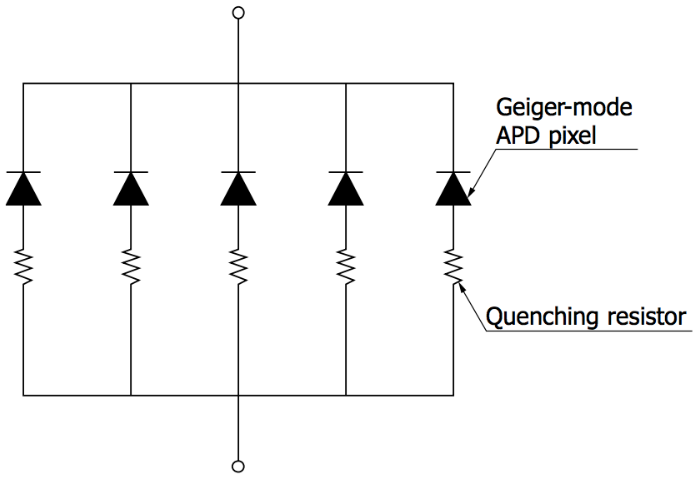

Figure 4.7: Quenching resisters in a SiPM [30]. The voltage drop caused by them finishes the avalanche multiplication.

pixel can detect a photon digitally, the SiPM can count the number of incident photons by connecting pixels in parallel.

Characteristics

The SiPM has the following advantages compared to the PMT.

- good single photon counting ability
- can be operated under a magnetic field
- low bias voltage
- small

On the other hand, the following properties must be carefully treated.

Dark Count Thermal excitation or tunneling effect can generate a one-photoelectron signal even when no photon enters the SiPM. It can be reduced by keeping the SiPM at low temperature as shown in Fig. 4.8. The dark count rate at the LXe temperature is known to be low enough to neglect.

Crosstalk Even when only one pixel makes a Geiger discharge primarily, a photon generated in the avalanche process can cause another Geiger discharge at another pixel, resulting in a two-photoelectron signal. It is called a prompt crosstalk. Sometimes the secondary photon is absorbed in the base and a career scatters, making a Geiger discharge at another pixel later. This is called a delayed crosstalk.

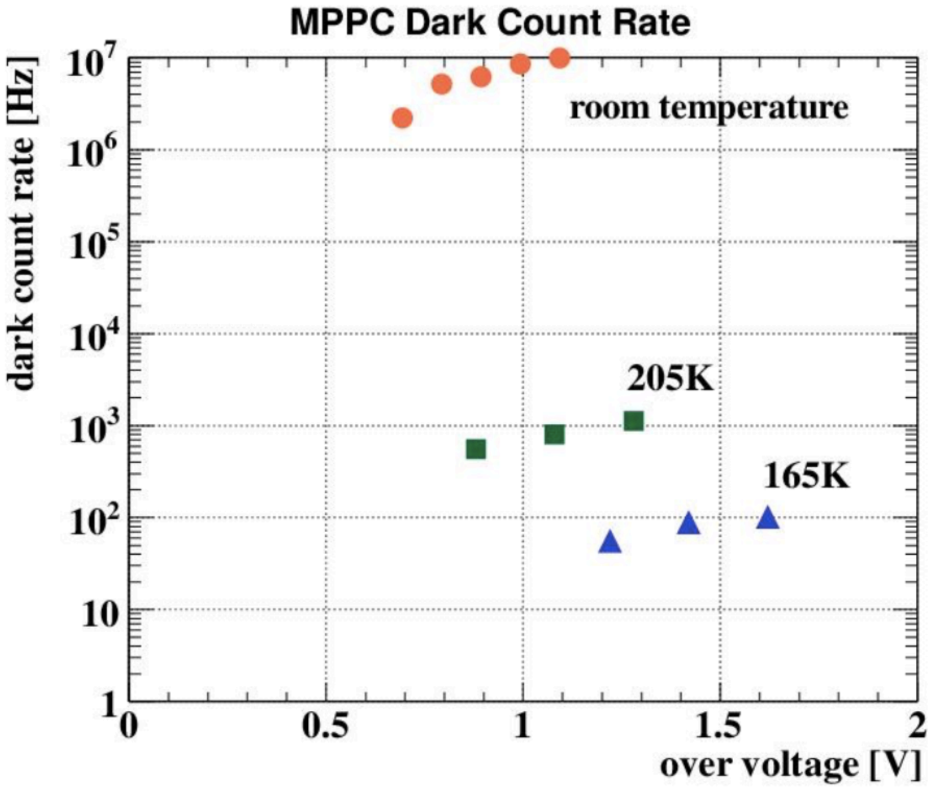

Figure 4.8: Dark count rate at low temperature for 3 mm^2 samples [10]. The dark count rate at the LXe temperature (165 K) is about 100 Hz which can be neglected in the MEG II experiment.

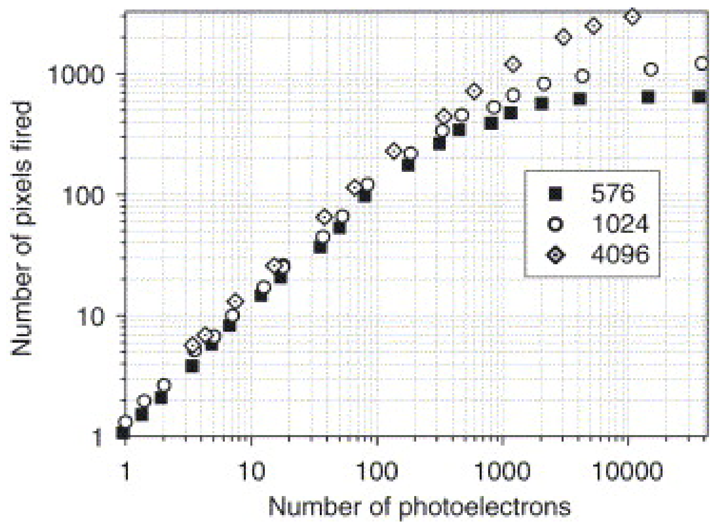

Figure 4.9: Saturation effect of a SiPM. When the number of photoelectrons is comparable to the number of pixels, the response becomes non-linear on account of the saturation.

Afterpulsing When an electron in avalanche multiplication is trapped to an energy level made by a lattice defect or impurity, it can make another avalanche in the same pixel later. It is called afterpulsing. Since it happens in the same pixel with the primary Geiger discharge, the signal height depends on the recovery time of quenching.

Saturation Since a SiPM counts the number of photons by the number of fired pixels, it cannot detect the photons entering simultaneously to the same pixel. Thus the response becomes non-linear when the number of photoelectrons is comparable to the number of pixels as shown in Fig. 4.9. The saturation is not a problem in the MEG II calorimeter because even the events which have conversion points close to the incident face do not generate so many photons as to saturate the SiPM [10].

Temperature Dependence The breakdown voltage of the SiPM depends on temperature because the interaction between the career and the phonon decreases at low temperature and the careers are easily accelerated.

Radiation Hardness Semiconducting detectors generally require careful handling concerning radiation hardness. In particular, the irradiation by the neutron increases the dark count rate. The expected $1.6 \times 10^8\ n/\mathrm{cm}^2$ irradiation during the MEG II experiment [10] will lead to 2–3 times larger dark count rate [31], but it is not a problem at low temperature in LXe. The gamma ray irradiation increases the leak current when the dose is over 200 Gy [32]. Since the expected dose is only 0.6 Gy in the MEG II experiment [10], it is not a problem either.

Development

There are the following requirements for the SiPMs used in the MEG II experiment.

- high sensitivity to the VUV light (175 nm)
- operational under low temperature (165 K)
- large area per channel ($12\,\mathrm{mm} \times 12\,\mathrm{mm}$)
- shorter time constant than that of the scintillation (45 ns)

The high sensitivity to the VUV light was achieved by thinning the contact layer and replacing the protecting layer with a VUV-transparent quartz window. In order to cover the large area by one readout channel, 4 chips are read out as one channel. The size of each chip is $6 \times 6\ \mathrm{mm}^2$. A hybrid connection scheme was developed to apply the bias voltage in parallel while reading the signal in series, and it is shown in Fig. 4.10. The parallel connection of the high voltage line keeps the total high voltage small and prevents from the discharges between chips. The series connection of the readout line makes the time constant of the signal waveform small because it reduces capacitance.

4.2 Event Reconstruction

In this section the reconstruction method of each variable is explained. The goal of the reconstruction of the LXe Calorimeter is to obtain three key variables of a gamma ray; the position of the first conversion point, the timing of the first conversion, the energy of the gamma ray. The reconstruction flow is shown in Fig. 4.11. First the charge and the timing are obtained from the waveform of each sensor. Then the charge is converted to the number of primary photoelectrons (N_{pe}) and the number of incident photons (N_{pho}). From the position distribution of N_{pho} in the incident face, the first conversion point is reconstructed. The energy and the timing are reconstructed using the distribution of N_{pho} and timing, respectively. The reconstructed position of the conversion point is also used for the reconstruction of those variables.

4.2.1 Waveform Analysis

Charge and timing of the signal detected by each photosensors are extracted by waveform analysis. Before that, a baseline slope and coherent noises are reduced by noise reduction.

The baseline of a waveform of a WaveDREAM board has a slope as shown in Fig. 4.12, which is considered to be due to the current leakage at the DRS. The voltage stored in the capacitors are sequently read out. If the voltage decreases at the same speed by a leakage, the bins which are read out later have lower voltage, resulting in the slope of the baseline. Since the slope is correlated to the temperature of the WaveDAQ board, it is corrected using the templates prepared for each temperature by the pedestal data taken periodically.

In order to synchronize all the readout channels, a clock signal is input to one channel in the DRS. The coherent noise synchronized to this clock signal is reduced using a noise

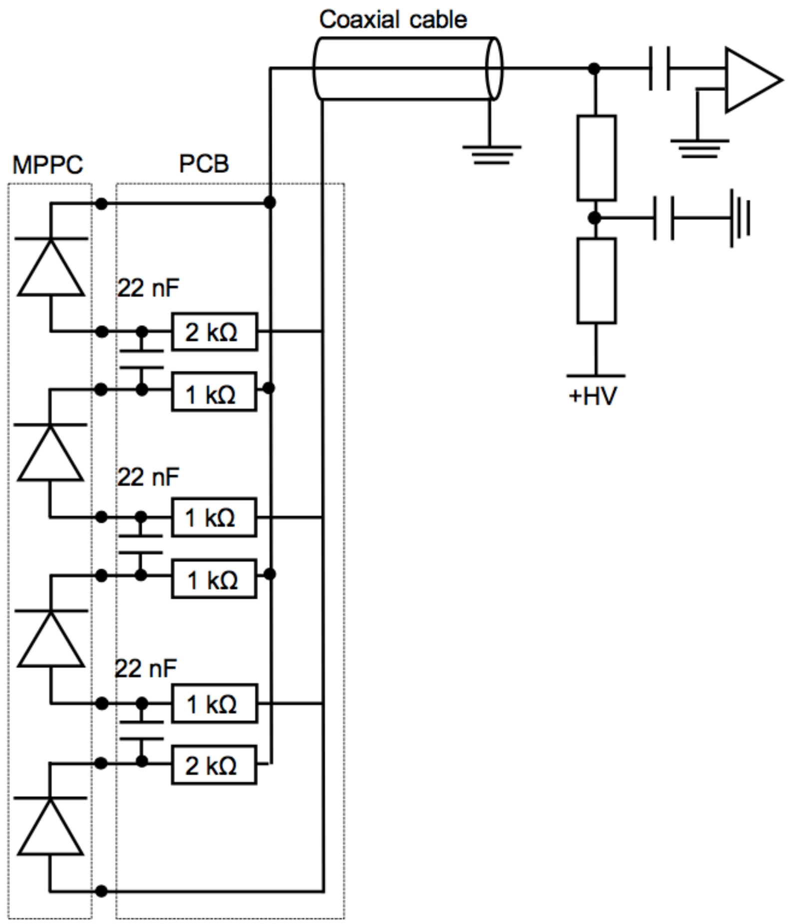

Figure 4.10: Hybrid connection scheme [33]. Parallel connection and series connection is combined incorporating the benefits.

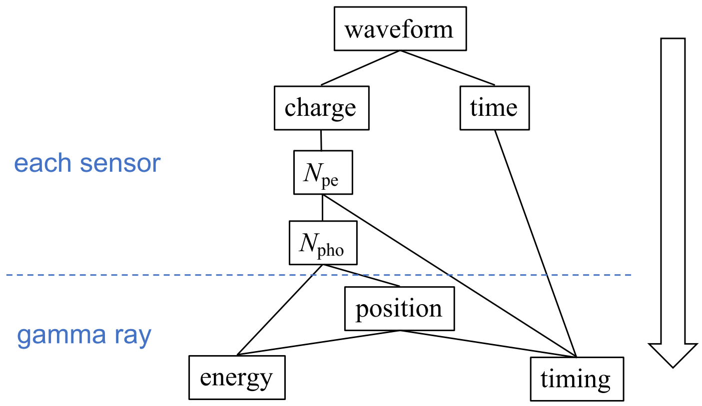

Figure 4.11: Reconstruction flow of the LXe Calorimeter. Charge and timing are obtained from waveforms of each channel, and they are used to reconstruct the position, timing and energy of the gamma ray.

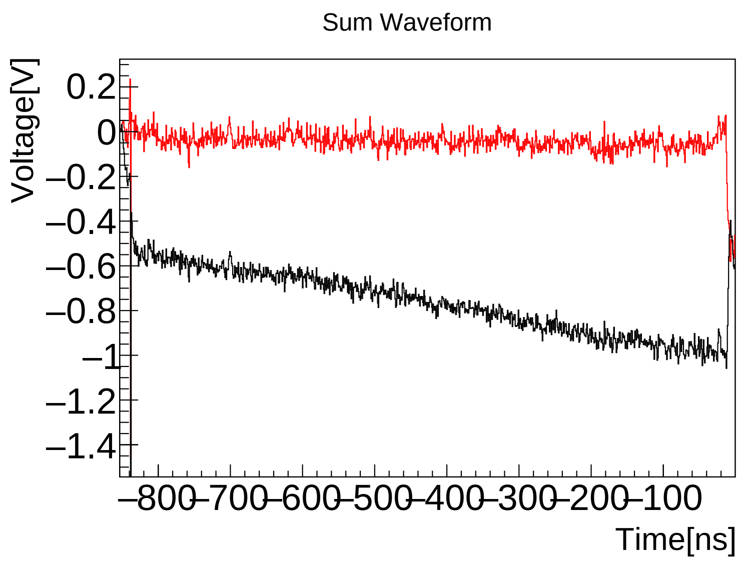

Figure 4.12: Baseline slope of the waveform before (black) and after (red) correction [5]. The slope is considered to be caused by the current leakage at the DRS.

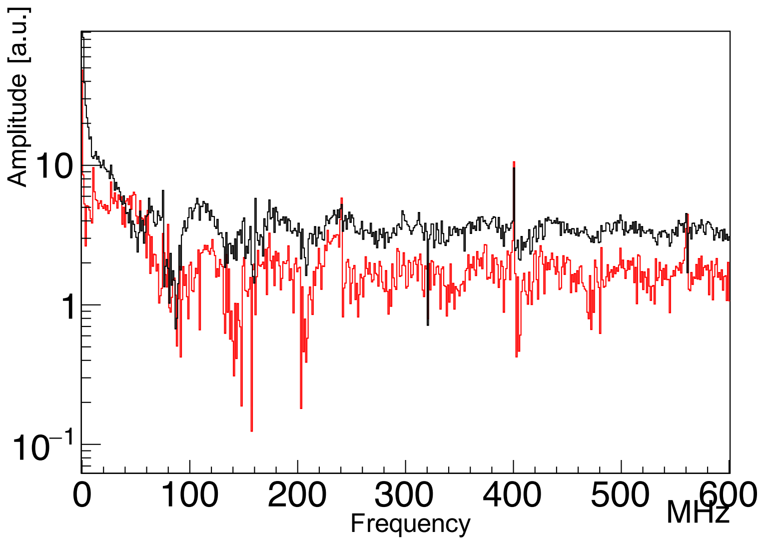

Figure 4.13: Amplitude spectrum of the sum waveform of 640 SiPMs before (black) and after (red) the noise subtraction.

template made from the pedestal runs after the baseline subtraction. Fig. 4.13 shows the performance of the noise subtraction.

The timing is extracted by the constant fraction method to avoid a time-walk effect to make it independent of the signal height.

The charge is extracted by integrating the waveform. The baseline charge is also calculated using the region before the waveform, and subtracted from the signal charge. The obtained charge is transformed to N_{pe}, which denotes the number of photoelectrons (for PMT) or the number of primary Geiger discharges (for SiPM), using a calibration factor $1/(G \cdot ECF)$. Here G denotes the gain, and ECF is the excess charge factor, which corresponds to the charge excess due to crosstalks and afterpulses of the SiPM. N_{pe} is converted to the number of incident photons, N_{pho}, by a calibration factor $1/PDE$, where PDE is the photon detection efficiency. These factors are obtained by different calibration methods and explained in detail in the next section.

4.2.2 Position Reconstruction

The position of the first conversion point $\boldsymbol{x}$ is reconstructed by minimizing the following chi squared;

$$\chi^2 = \sum_{i}^{\text{sensors}} \left(\frac{N_{\text{pho},\,i} - C \cdot \Omega_i(\boldsymbol{x})}{\sigma_{N_{\text{pho},\,i}}} \right)^2, \tag{4.3}$$

where C is a nuisance parameter representing the total light yield, $\Omega_i(\boldsymbol{x})$ is the solid angle of the sensor i viewed from a position $\boldsymbol{x}$, and σ is the statistical uncertainty of the estimation of the $N_{\text{pho},\,i}$. In reality, the photon distribution depends on the direction of the electromagnetic shower development and the effect is corrected.

4.2.3 Energy Reconstruction

The energy is reconstructed basically by summing the number of photons entering each sensor. There are actually some corrections and the equation of the reconstruction is as follows;

$$E_\gamma = C \cdot F_E(\boldsymbol{x}) \cdot \sum_i^{\text{sensors}} (\alpha_i \cdot N_{\text{pho},\, i}), \tag{4.4}$$

where C is a calibration constant to convert the number of photons to the energy, $F_E(\boldsymbol{x})$ is the correction function which correct the position dependence of the detector response, α_i is geometrical weight for each sensor. α_i is fixed by the geometry, and C and F_E is determined by dedicated calibration experiments explained in Sec. 4.3.3

4.2.4 Timing Reconstruction

First of all, the timing of the first conversion is estimated channel by channel using the following equation;

$$t_{\text{conv},\, i} = t_{\text{sensor},\, i} - t_{\text{delay}}(d_i,\, \eta_i,\, N_{\text{pe},\, i}) - t_{\text{offset},\, i}, \tag{4.5}$$

where i denotes each sensor. $t_{\text{sensor},\, i}$ is the constant fraction time obtained by the waveform analysis. $t_{\text{delay}}(d_i,\, \eta_i,\, N_{\text{pe},\, i})$ is a correction function which depends on the distance between the conversion point and the sensor d_i, the angle between the conversion point and the sensor η_i, and $N_{\text{pe},\, i}$. $t_{\text{offset},\, i}$ is a channel by channel offset due to the cable and the electronics synchronization. t_{delay} is described by three components,

$$t_{\text{delay}}(d_i,\, \eta_i,\, N_{\text{pe},\, i}) = t_{\text{ToF}}(d_i) + t_{\text{indir}}(\eta_i) + t_{\text{walk},\, \alpha}(N_{\text{pe},\, i}). \tag{4.6}$$

t_{ToF} is the time of the photon propagation from the conversion point to the sensor. t_{indir} is the effect of a delay of the arrival of photons scattered somewhere and it is a function of η_i, because the number of indirect photons increases with the angle between the light source and the sensor. t_{walk} is the time walk which cannot be completely eliminated by the constant fraction method. Since the waveform is different for the PMTs and the SiPMs, and for the production lots of the SiPM, the time-walk correction function is prepared separately for them as indicated by α in the equation.

The conversion time t_{conv} is estimated by the maximum likelihood method using $t_{\text{conv},\, i}$ of each sensor. The likelihood function is written as follows;

$$L(t_{\text{conv}}) = \prod_i f(t_{\text{conv},\, i} - t_{\text{conv}},\, N_{\text{pe},\, i}), \tag{4.7a}$$

$$f(dt,\, N_{\text{pe}}) = \text{ExpGaus}(dt;\, \sigma(N_{\text{pe}}),\, \tau(N_{\text{pe}})), \tag{4.7b}$$

$$\text{ExpGaus}(dt;\, \sigma,\, \tau) = \begin{cases} \exp\left(-\frac{dt^2}{2\sigma^2}\right) & (dt < \sigma^2/\tau) \\ \exp\left(-\frac{dt}{\tau} + \frac{\sigma^2}{2\tau^2}\right) & (dt > \sigma^2/\tau) \end{cases}, \tag{4.7c}$$

where $\sigma(N_{\mathrm{pe}})$ is the timing resolution, and $\tau(N_{\mathrm{pe}})$ is the effect that scintillation photons do not come probabilistically when the number of photoelectrons is small. Both functions are determined by a dedicated calibration run explained in Sec. 4.3.3.

A simulation study shows that the obtained t_{conv} still depends on the conversion position although the cause is not understood [34]. Thus finally it is corrected by a global correction function which provides a correction factor depending on the conversion position. This global function is also obtained by a calibration run.

4.3 Calibration

The event reconstruction requires various calibration parameters. In the MEG II experiment, the photosensors are calibrated using LEDs and alpha ray sources, and the overall detector response is calibrated by two different gamma ray sources.

4.3.1 Photosensor

When N_{pho} photons enters the sensitive area of the photosensor, the charge Q obtained from the waveform is written as follows;

$$N_{\mathrm{pe}} = N_{\mathrm{pho}} \cdot PDE, \tag{4.8a}$$
$$Q = N_{\mathrm{pe}} \cdot ECF \cdot G \cdot e. \tag{4.8b}$$

The photon goes through the window and is detected generating a photoelectron with Photon Detection Efficiency (PDE). PDE of a PMT is written as the product of the quantum efficiency (QE) and the collection efficiency (CE). QE is the probability of an incident photon producing a photoelectron on the photocathode, and it depends on the wavelength of the photon. CE is the probability of the photoelectron being caught by the first dynode and resulting in the multiplication, and it depends on the applied voltage and the surrounding magnetic field. The photoelectron is multiplied by a gain factor (G), and observed as charge (Q) which can be obtained by multiplying elementary charge (e). In the SiPM case, the number of photoelectrons is larger than the number of primary Geiger discharges (N_{pe}) owing to the existence of the crosstalk and afterpulsing. This effect is represented by Excess Charge Factor (ECF).

In order to estimate N_{pe} and N_{pho}, the calibration factors PDE and $G{\cdot}ECF$ are necessary. $G \cdot ECF$ is obtained by an LED run while PDE is estimated from an α run. The calibration methods are explained in detail below;

Setup

LED $G \cdot ECF$ is measured using photons from blue LEDs. The LEDs are put on the inner wall of the detector as shown in Fig. 4.14. Light from the LEDs which were also used in the MEG experiment is reduced by an aluminum sheet with pinholes and diffused uniformly by teflon as shown in Fig. 4.15. These LEDs are located on the lateral faces, and they are used for the PMT gain calibration. Some LEDs have been newly installed for the MEG II

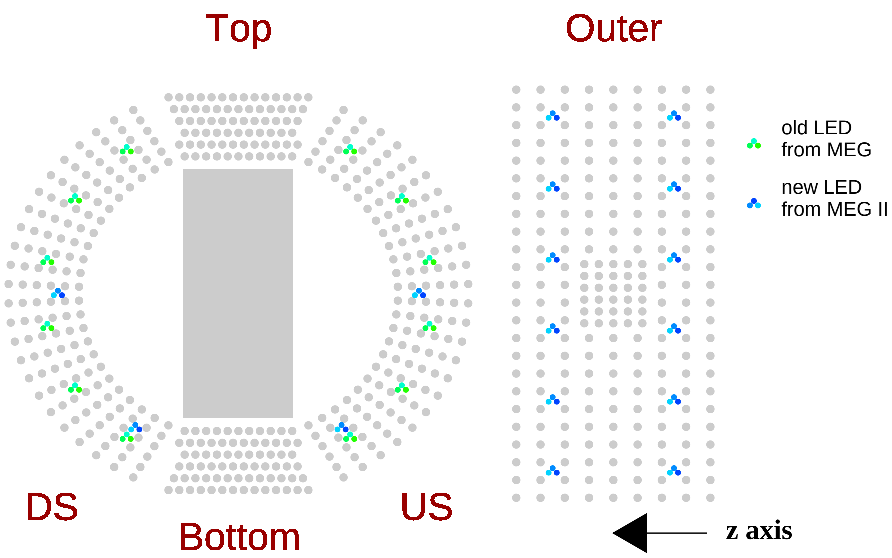

Figure 4.14: Position of the LEDs [5]. The LEDs used from the MEG experiment are shown in green and the others in blue.

Table 4.3: Basic properties of the ^{241}Am sources for calibration.

half-life	432.6 years [36]
activity	200 Bq [35]
energy	5.4856 MeV (84.5%) [36]
	5.4429 MeV (13.2%) [36]

experiment mainly on the outer face to provide more uniform light for the incident face, and they are used for the SiPM calibration. The light from some of them is also reduced and scattered by teflon as shown in Fig. 4.16. The purpose of the light reduction is to reduce the relative fluctuation of LED light intensity by applying large voltage.

Alpha Ray Source Since *PDE* depends on the wavelength of the photons, it should be measured with the xenon scintillation light. For the PDE calibration, five wires with ^{241}Am [35] are put in the detector as alpha ray sources. The basic properties of the ^{241}Am source is summarized in Tab. 4.3. Five sources are on a 100 μm diameter tungsten wire at 12.4 cm interval. Each source is covered by 1.5 μm thick gold as shown in Fig. 4.17. The position of the wires is different in height as shown in Fig. 4.18.

Method

PMT Gain Since gain of the PMTs used in the MEG and MEG II experiment has a large dependence on the incident position on the photocathode, one-photoelectron signals cannot be distinguished from pedestal events. Therefore, gain is measured using the property of the

Figure 4.15: LEDs used from the MEG experiment. The light is reduced by an Aluminum pinhole and scattered by teflon.

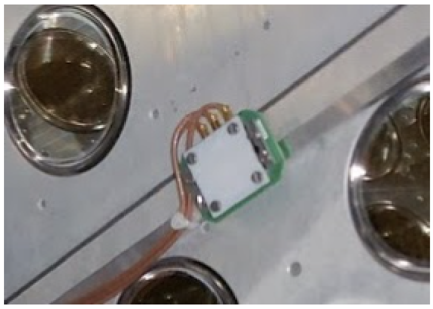

Figure 4.16: Newly installed LEDs. The teflon reduces and scatters the light from the LEDs.

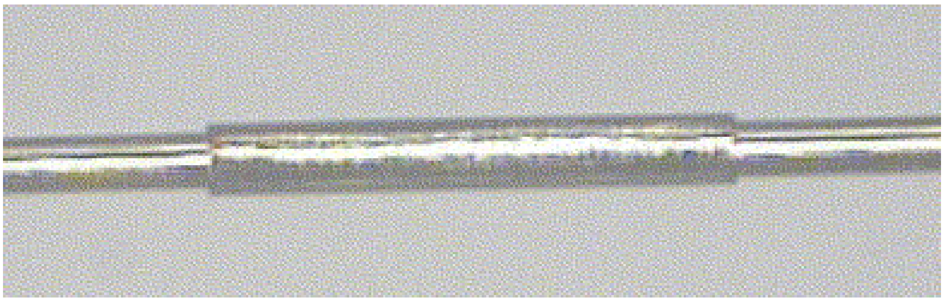

Figure 4.17: ^{241}Am alpha ray source covered in gold [35].

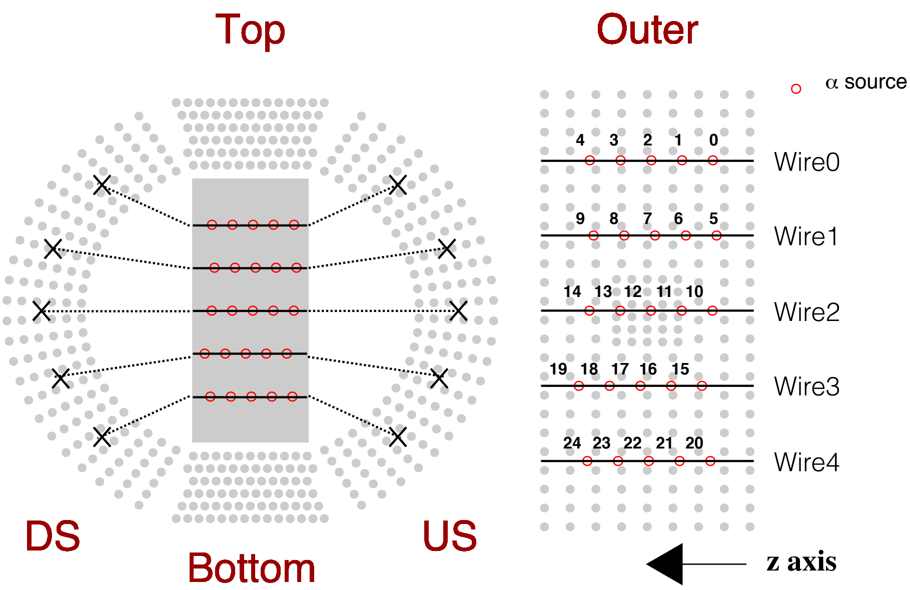

Figure 4.18: Position of the alpha ray sources [5]. 25 sources in total are put on 5 wires in the detector.

Poisson statistics of the number of photoelectrons. Only a small part of the LED photons enters the PMT surface, goes through the quartz window, and makes photoelectrons. Thus the number of photoelectrons N_{pe} follows Poisson distribution if the fluctuation of the LED light is small enough compared to the Poisson variance. The probability of obtaining N_{pe} photoelectrons can be written as follows by denoting the mean by $\bar{N}_{\mathrm{pe}}$;

$$P(N_{\mathrm{pe}}) = \mathrm{Poisson}_{\bar{N}_{\mathrm{pe}}}(N_{\mathrm{pe}}), \tag{4.9a}$$

$$\mathrm{Poisson}_{\lambda}(k) = \frac{\lambda^k \mathrm{e}^{-\lambda}}{k!}, \tag{4.9b}$$

when a certain intensity of LED light is used. Assuming the gain G fluctuate by Normal distribution whose mean is $\bar{G}$ and standard deviation is σ_G, and there is white noise whose mean is Q_0 and RMS is σ_0, the distribution of charge Q is written as follows;

$$P(Q) = \sum_k \mathrm{Poisson}_{\bar{N}_{\mathrm{pe}}}(k) \int dG\, \mathrm{Norm}_{\bar{G},\,\sigma_G}(G) \cdot \mathrm{Norm}_{kGe+Q_0,\,\sigma_0}(Q), \tag{4.10a}$$

$$\mathrm{Norm}_{\mu,\,\sigma}(x) = \frac{1}{\sqrt{2\pi}\sigma} \exp\left(-\frac{(x-\mu)^2}{2\sigma^2}\right). \tag{4.10b}$$

Then the mean $\bar{Q}$ and the variance σ_Q^2 of this charge distribution can be written as

$$\bar{Q} = \bar{N}_{\mathrm{pe}}\bar{G}e + Q_0 \tag{4.11}$$

$$\sigma_Q^2 = \sigma_0^2 + \bar{G}e(\bar{Q} - Q_0)\left\{1 + \frac{\sigma_G^2}{\bar{G}^2}(1 + \bar{N}_{\mathrm{pe}})\right\}. \tag{4.12}$$

When σ_G is small enough compared to $\bar{G}$, the relation between $\bar{Q}$ and σ_Q becomes simple;

$$\sigma_Q^2 = \sigma_0^2 + \bar{G}e(\bar{Q} - Q_0). \tag{4.13}$$

Since the noise level does not depend on the LED intensity, the linear plot like Fig. 4.19 can be obtained by analyzing the charge distributions from different LED intensities. The slope of the plot corresponds to the gain. The gain of the PMTs in the calorimeter has been monitored during pilot runs and is discussed in Chap. 6.

SiPM Gain and ECF The one-photoelectron peak can be resolved in charge distribution of SiPMs after reducing the noise. The typical charge distribution for weak LED light is shown in Fig. 4.20.

ECF is the ratio between the actually measured charge and the charge expected only from the primary Geiger discharge. It is more than one in the SiPM case owing to the correlated noise such as crosstalk and afterpulsing. In order to estimate the number of primary photoelectrons, again the Poisson statistics is utilized. Although the charge distribution is distorted from the Poisson distribution owing to the correlated noise, the number of events in the pedestal peak is not affected. According to the Poisson statistics, the fraction of the pedestal events can be written as

$$f_0 = \mathrm{Poisson}_{\bar{N}_{\mathrm{pe}}}(0) = \mathrm{e}^{-\bar{N}_{\mathrm{pe}}}. \tag{4.14}$$

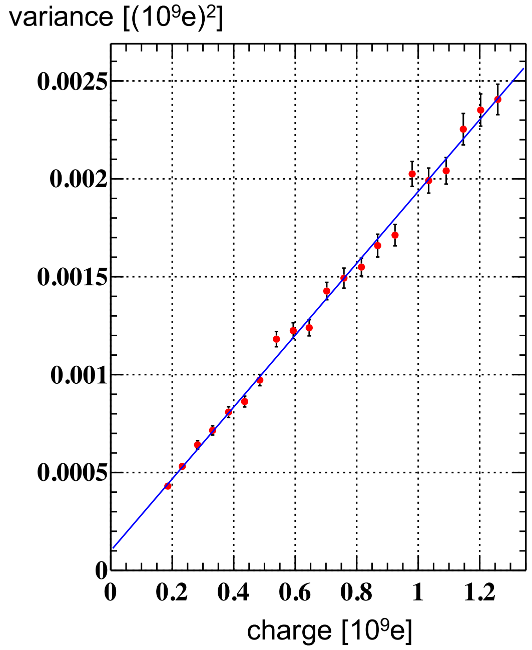

Figure 4.19: Relation between the variance and the mean of the charge distribution from the constant LED signal. The slope of this plot corresponds to the gain of the PMT.

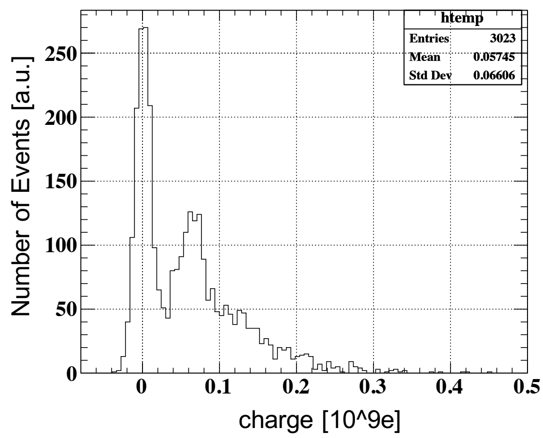

Figure 4.20: Charge distribution of a SiPM for weak LED light [5]. The peak of the one-photoelectron signal is resolved. The fraction of the pedestal events can be used to estimate N_{pe}.

Then, the number of primary Geiger discharge N_{pe} is

$$N_{\mathrm{pe}} = -\ln f_0. \tag{4.15}$$

$G \cdot ECF$ can be calculated by

$$G \cdot ECF = -\frac{\bar{Q}/e}{\ln f_0}. \tag{4.16}$$

Other methods of monitoring SiPM gain are discussed in Sec. 5.

PDE Although the alpha ray from the ^{241}Am source has monochromatic energy, it loses some energy in the gold cover and converts the remaining energy into scintillation photons. Some photons reach a photosensor directly, and some are scattered by LXe and finally are detected, while others are absorbed by LXe or detector walls. The whole process is simulated by Geant4 [37] version 10.4.p02 and the number of photons entering the sensors is calculated. Then PDE is calculated as

$$PDE = \frac{N_{\mathrm{pe}}}{N_{\mathrm{pho}}}, \tag{4.17}$$

where N_{pho} is the calculated value by simulation and N_{pe} is obtained using $G \cdot ECF$ measured in the method described above.

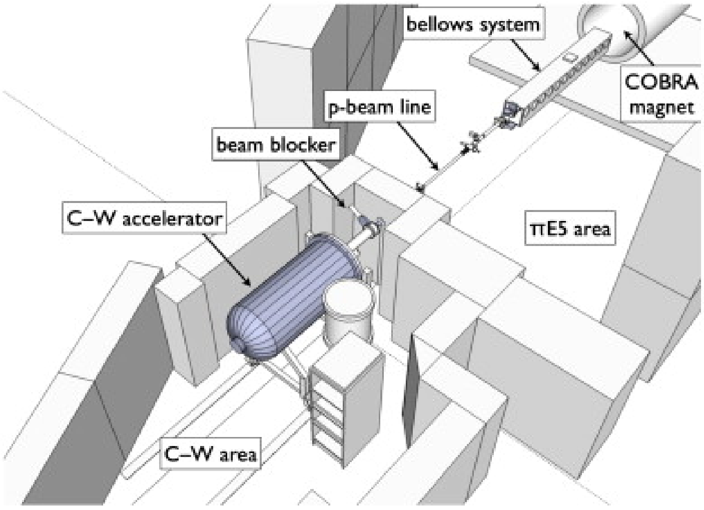

Figure 4.21: CW beam line [38]. Protons are accelerated by Cockcroft-Walton accelerator located at the downstream side of the MEG II detectors.

4.3.2 Cockcroft-Walton-Litheum Calibration

As shown in Fig. 4.21, the MEG II collaboration has a Cockcroft-Walton (CW) accelerator in the downstream side of the detectors. It accelerates protons to 440 keV. When the proton is stopped on a $Li_2B_4O_7$ target, a 17.6 MeV monochromatic gamma ray is generated from the reaction $^7\mathrm{Li}(p,\gamma)^8\mathrm{Be}$. The muon target is replaced with a LiBO target, and it is tilted by 45 degrees so that it will not prevent the gamma ray directing to the xenon calorimeter. The exchange of the beamline can be done easily because CW beam comes from the downstream side and it does not conflict with the muon beam line. It enables the frequent calibration and it was used twice a week in the MEG experiment. This calibration is called the CW-Li calibration. The main purpose of this calibration is to monitor the energy scale stability, which can be affected by the change of the optical property of the LXe (the light yield or attenuation length) due to the purity variation, or by the miscalibration of the photosensors.

4.3.3 Charge Exchange Calibration

The MEG II beam line can switch the beam particle from muon to pion. The negative pion is used for the calibration of the LXe Calorimeter through charge exchange (CEX) reaction;

$$\pi^- p \to \pi^0 n. \tag{4.18}$$

The experimental setup of the CEX calibration is schematically depicted in Fig. 4.22. When a negative pion is injected to a liquid hydrogen target and stops inside it, a neutral pion is generated and decays into two gamma rays immediately;

$$\pi^0 \to \gamma\gamma. \tag{4.19}$$

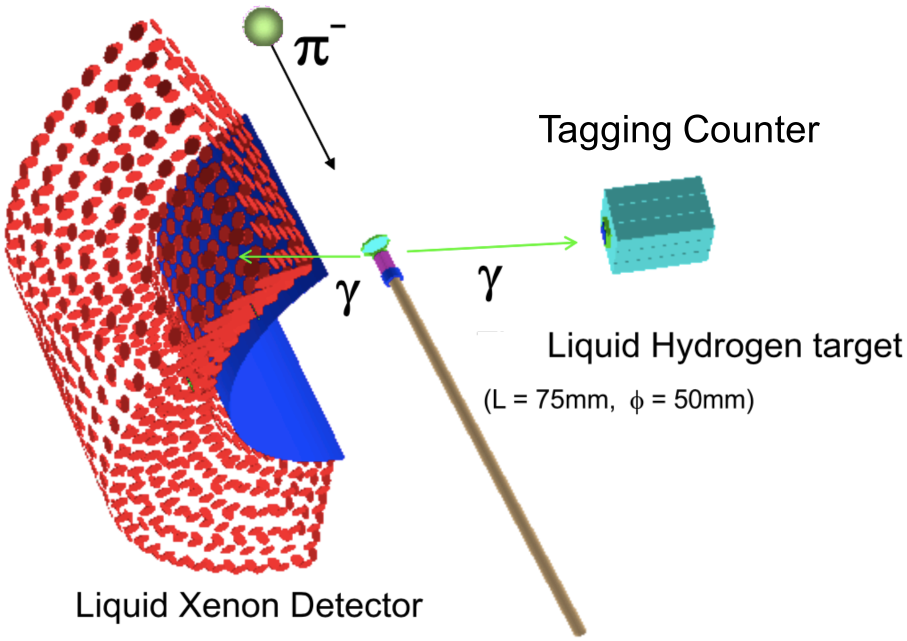

Figure 4.22: Overview of the CEX calibration [29]. A negative pion is converted into a neutral pion in the liquid hydrogen target, and the gamma rays generated from the decay of the neutral pion are detected by the LXe Calorimeter and a tagging detector. The tagging detector is explained in Sec.7.1

These gamma rays are used for the calibration of the calorimeter.

Since the CEX reaction occurs after the negative pion has stopped and the gamma rays are generated from a two body decay, the energy of the gamma ray can be calculated kinematically. By choosing the events where the two gamma rays are emitted into the opposite directions, a specific energy can be obtained; 54.9 MeV and 82.9 MeV. Since 54.9 MeV is near the signal energy (52.8 MeV), important calibration and performance evaluation is conducted using this gamma ray. This calibration method is called CEX calibration. The improvement of the CEX calibration is discussed in Chap. 7.

4.4 Status

Construction of the LXe Calorimeter has been finished in 2017, and the next step is to achieve and confirm the required performance. As explained in this chapter, reconstruction of observables needs calibration. In the following sections three topics on calibration are discussed. First of all, calibration of photosensors is necessary. New calibration methods of gain of SiPMs, which has been newly introduced in the MEG II experiment, was developed. PMTs were also calibrated by the methods used in the MEG experiment, and aging of PMTs which is important in the high beam rate environment was investigated. The CEX calibration is most important for investigating the overall detector performance. In order to improve precision of the CEX calibration corresponding to the improvement of resolution, a new beam monitoring detector was proposed and developed.

Part II

Photosensor Calibration

Chapter 5

Comparison of Gain Monitoring Methods for SiPM

Scintillation photons are detected by photosensors located on the inner wall of the calorimeter. Photosensors convert photons into electrons and multiply them, providing detectable electronic signals. In order to reconstruct the number of incident photons, it is necessary to know the properties of the photosensors. One of the most important parameters is the gain, which represents how many electrons are generated from an initial single electron.

In this chapter, methods of measuring the gain of SiPMs are discussed. A conventional method is explained in the first section with its disadvantages. Two alternative methods which can overcome the disadvantages are discussed in the following sections.

5.1 Gain of SiPM

A SiPM is a photosensor which can detect a single photon. Therefore, the gain can be obtained directly from the size of the single-photon signals. Although this method is simple and powerful, it has some disadvantages. First, this method is available only when a single-photoelectron peak is resolved. In other words, gain cannot be obtained in noisy environment by this method. Second, this method needs a specific setup for the measurement because it is necessary to prepare a light source which provides optimal intensity.

Recently two other methods have been proposed, which might overcome the disadvantages of the standard method. The first one is the statistical method which uses a statistical property of charge distribution obtained by a SiPM. The second one analyzes the shape of the waveform to extract information concerning gain.

5.2 Statistical Method

The statistical method has been used for the PMT gain calibration in the MEG and MEG II experiment. The application of this method to a SiPM has been tested in Ref [39]. In this study, the statistical method is applied to a SiPM (MPPC S13360-3050CS by Hamamatsu [40]) and a solution to a newly found problem is provided.

5.2.1 Previous Study

Photons emitted by an LED generate an electron-hole pair and trigger avalanche multiplication with small probability. Thus, it can be assumed that the number of the primary Geiger discharges follows Poisson distribution. In this case gain can be obtained from the relation between variance and mean of the charge distribution as discussed in Sec. 4.3.1.

However, the SiPM has a peculiar characteristics and additional signals come from correlated noises: the crosstalk and the afterpulsing. A model to include the effect of crosstalk is proposed in Ref. [39]. When the number of photoelectrons made by crosstalks (CT) from one primary Geiger discharge follows Poisson distribution with mean λ_{CT}, the total number of photoelectrons (n) follows Generalized Poisson distribution $\mathrm{GP}_{\bar{N}_{pe},\,\lambda_{\mathrm{CT}}}(n)$. $\bar{N}_{\mathrm{pe}}$ is mean number of primary Geiger discharges, and Generalized Poisson distribution is represented as follows;

$$\mathrm{GP}_{\mu,\,\lambda}(n) = \frac{\mu(\mu+n\lambda)^{n-1}\mathrm{e}^{-(\mu+n\lambda)}}{n!}. \tag{5.1}$$

Mean and variance of the Generalized Poisson distribution are $\mu/(1-\lambda)$ and $\mu/(1-\lambda)^3$, respectively. The number of photoelectrons actually bocomes smaller than this disribution when λ_{CT} is too large, because crosstalks usually occur only in the neighboring cells and there should be limitation in the number of crosstalks in reality. The charge distribution changes from Eq. 4.10b as follows in accordance with the introduction of the crosstalk effect;

$$P(Q) = \sum_k \mathrm{GP}_{\bar{N}_{\mathrm{pe}},\,\lambda_{\mathrm{CT}}}(k) \int dG\,\mathrm{Norm}_{\bar{G},\,\sigma_G}(G)\cdot \mathrm{Norm}_{kGe+Q_0,\,\sigma_0}(Q), \tag{5.2}$$

$$\bar{Q} = \bar{G}e\frac{\bar{N}_{\mathrm{pe}}}{1-\lambda_{\mathrm{CT}}} + Q_0, \tag{5.3}$$

$$\sigma_Q^2 \simeq \sigma_0^2 + \bar{G}^2e^2\frac{\bar{N}_{pe}}{(1-\lambda_{\mathrm{CT}})^3} \tag{5.4a}$$

$$= \sigma_0^2 + \frac{1}{(1-\lambda_{\mathrm{CT}})^2}\bar{G}e(\bar{Q}-Q_0) \tag{5.4b}$$

Once $1/(1-\lambda_{\mathrm{CT}})^2$ is known, the gain can be calculated from the relation between variance and mean of the charge distribution with the same procedure with the case without crosstalks.

The conversion factor $1/(1-\lambda_{\mathrm{CT}})^2$ is needed to convert the slope of variance vs mean plot to the gain. The conversion factor can be obtained from a measurement with weak LED. Using Eq. 5.3 and Eq. 5.4, the conversion factor can be represented as follows;

$$\frac{1}{1-\lambda_{\mathrm{CT}}} = \bar{N}_{\mathrm{pe}}\frac{\sigma_Q^2-\sigma_0^2}{(\bar{Q}-Q_0)^2}. \tag{5.5}$$

$\bar{N}_{\mathrm{pe}}$ can be obtained using the pedestal fraction;

$$f_0 = \mathrm{GP}_{\bar{N}_{\mathrm{pe}},\,\lambda_{\mathrm{CT}}}(0) = \mathrm{e}^{-\bar{N}_{\mathrm{pe}}}. \tag{5.6}$$

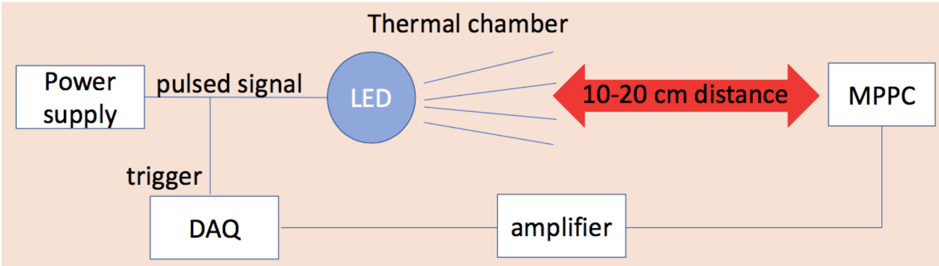

Figure 5.1: Setup for the gain measurement of the statistical method [41]. The SiPM detects constant intensity LED light.

The advantage of this method is that once the conversion factor is known, the gain can be obtained only from a simple statistical property; mean and variance. The gain can be monitored even when a single-photoelectron peak is not resolved, although in order to obtain the absolute value the conversion factor must be known beforehand by counting the number of pedestal events.

5.2.2 Validation Test

A validation test of this principle was conducted. The experimental setup is shown in Fig. 5.1. A blue LED in pulse operation is used as a light source. MPPC S13360-3050CS is used as a SiPM sample, and the MPPC signals are read out by a DRS evaluation board after the amplification by a factor of about 70. The LED, the SiPM and the amplifier are placed in a thermal chamber which keeps the temperature around 25 °C.

Fig. 5.2 shows the charge distribution obtained by a measurement with weak LED light. The conversion factor can be calculated from the fraction of the pedestal events. Fig. 5.3 shows the relation between variance and mean obtained by analyzing charge distributions with different light intensity runs. One point corresponds to one run with constant intensity LED light.

According to the model with Generalized Poisson distribution, variance depends linearly on mean, and the gain can be calculated using the slope. However, the measured relation in Fig. 5.3 is rather quadratic than linear. The reason of this non-linearity is discussed in the next section although the cause has not become clear. In any case, the gain was successfully extracted from the relation between variance and mean as follows. Assuming that the over-linearity is an additional effect on the Generalized Poisson statistics which occurs only when a large number of photoelectrons are generated, the slope around the origin was compared to the gain. What was actually done is fitting the variance vs mean plot by the quadratic function, $\sigma_Q^2 = c_0 + c_1 \cdot \bar{Q} + c_2 \cdot \bar{Q}^2$, and calculating gain multiplying c_1 by $(1 - \lambda_{\mathrm{CT}})^2$ obtained from a measurement using weak LED light. The measurement was repeated with some different overvoltages, and λ_{CT} was 20–40% depending on the overvoltage. The calculated gains were compared with those obtained by the usual single-photoelectron method. As shown in Fig. 5.4, the calculated gains are consistent with those measured by

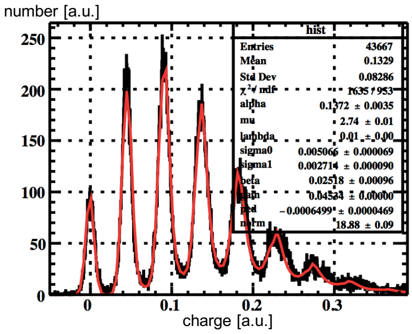

Figure 5.2: Charge distribution obtained by a measurement using weak LED light.

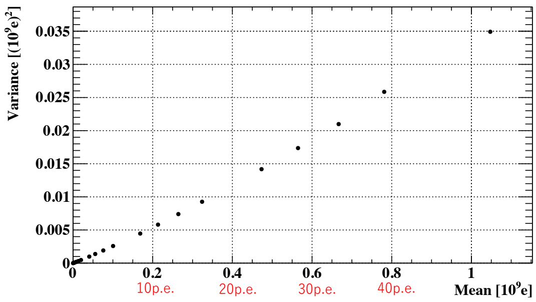

Figure 5.3: Variance as a function of mean [41]. The relation is rather quadratic than linear.

the single-photoelectron method. The precision was 2.5% in RMS.

5.2.3 Relation between Variance and Mean

The measured relation between variance and mean was rather quadratic although it should be linear in principle based on the model using Generalized Poisson distribution. The cause of this relation is investigated as follows.

Linearity of Amplifier Linearity of the readout system was first checked. A DRS Evaluation Board developed by PSI was used as a waveform digitizer and full waveforms were obtained. This board has the dynamic range of 1 V, and the range was set to [−50 mV, +950 mV]. Signals from the SiPM was amplified before being read out. The amplifier is also developed by PSI, and its circuit is shown in Fig. 5.5. The SiPM is biased through the signal line which is AC-coupled to the amplification stage.

The linearity of this amplifier was measured with the setup shown in Fig. 5.6. A signal from the SiPM is divided into two signals after amplification. One goes directly to the DRS and the other is amplified again by an additional amplifier. By comparing the two signals, linearity of the additional amplifier can be obtained.

The result is shown in Fig. 5.7. Considering that the output from the amplifier is attenuated by a factor 4, the linearity is guaranteed when the output signal height is less than 1.6 V.

Effect of Afterpulsing The non-linearity of the relation between mean and variance might come from certain characteristics of the SiPM which is not taken into account in modeling of charge distribution, such as afterpulsing. The assumed Generalized Poisson distribution of the number of photoelectrons takes only the crosstalk into account. The afterpulsing is different from the crosstalk in that the signal size is not constant and it depends on the time difference between the primary discharge and the afterpulse. Since it is rather difficult to take it into account analytically, a waveform simulation was conducted and the effect of afterpulsing on the charge distribution was investigated.

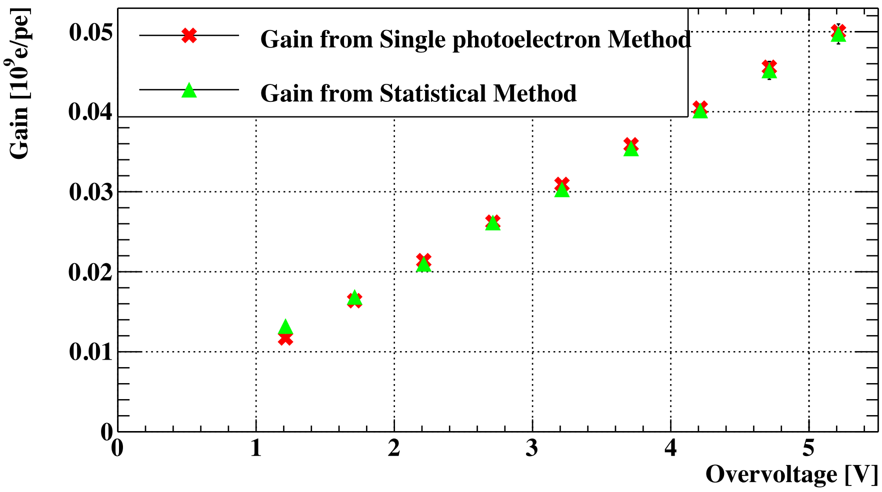

Figure 5.4: Gain obtained from the usual single-photoelectron method and from this statistical method as a function of overvoltage [41]. Statistical uncertainty is shown as error bars.

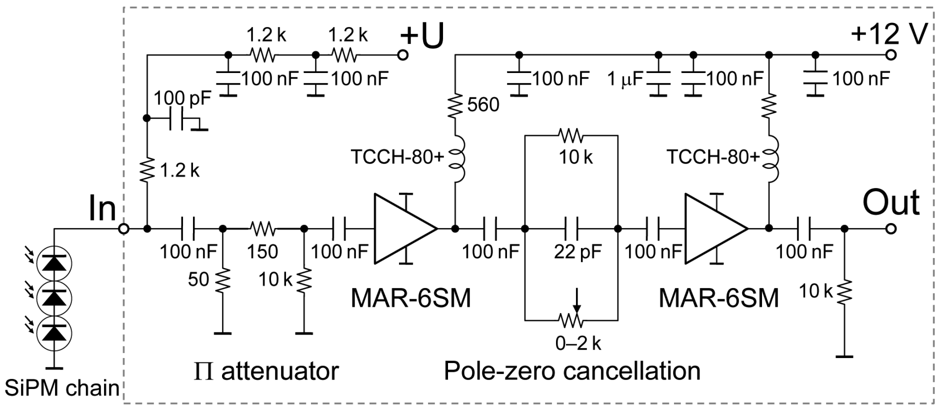

Figure 5.5: Circuit diagram of the amplifier [42].

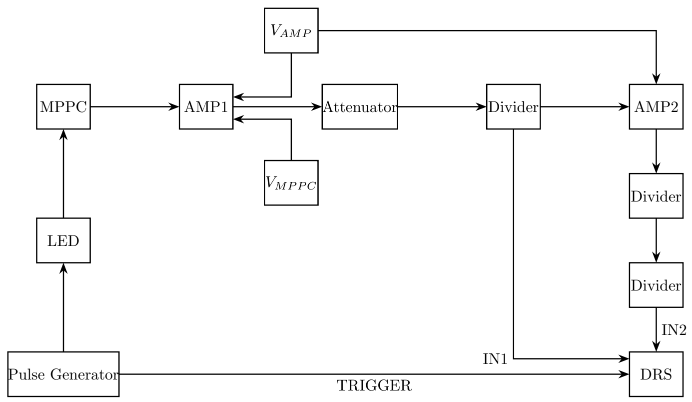

Figure 5.6: Setup for the measurement of the saturation of the readout system. The signals before and after amplified are compared.

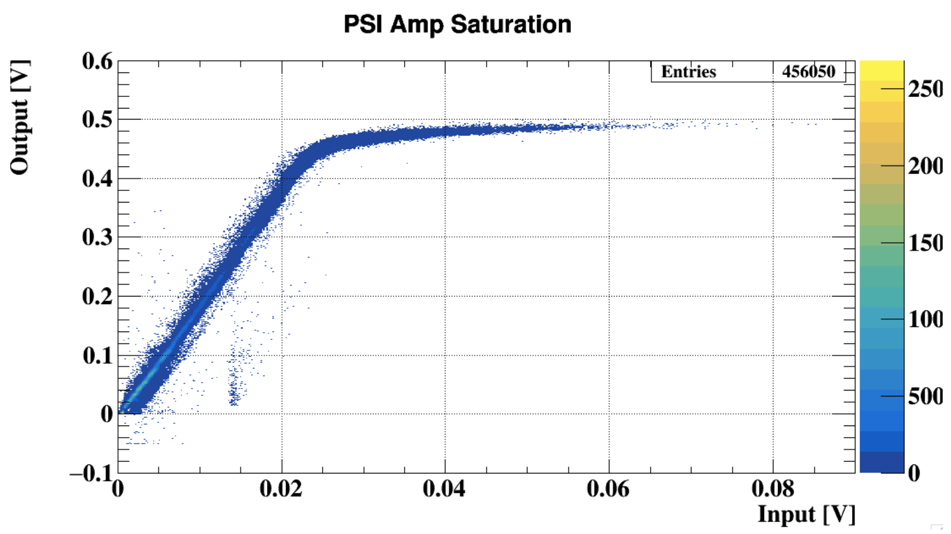

Figure 5.7: Linearity of the amplifier. The input signal (x-axis) is amplified and output as the height in y-axis.

It is necessary to make a model to simulate the SiPM waveform which takes the afterpulsing into consideration. The waveform from a single photoelectron is assumed to rise up instantly and decay exponentially with the time constant τ_{decay}. Time distribution of emission of photons from an LED is also assumed to be exponential with the time constant $\tau_{\text{LED}} = 40$ ns. Since there are quenching resisters in each cell of a SiPM, the size of the pulses which start after a main pulse is smaller. The later the pulse occurs, the larger the pulse becomes, because the voltage recovers gradually. Assuming that time distribution of afterpulsing is exponential with the time constant τ_{AP} and the cell recovers with the same time constant with that of waveform, the timing distribution of afterpulsing and the height of the afterpulse signal are written as follows;

$$\frac{dp}{dt_{\text{AP}}} = \frac{1}{\tau_{\text{AP}}} e^{-t_{\text{AP}}/\tau_{\text{AP}}}, \tag{5.7}$$

$$H_{\text{AP}} = (1 - e^{-t_{\text{AP}}/\tau_{\text{decay}}}) H_{\text{1pe}}, \tag{5.8}$$

where H means the height of the signal and H_{1pe} is that of a one photoelectron pulse.

In the simulation, the number of primary Geiger discharges follow Poisson distribution, and each discharge generates crosstalks whose number is determined also by Poisson distribution. A fired cell can be followed by an afterpulse whose timing distribution and the signal size are defined by the equations above with certain probability. Changing the mean number of the primary Geiger discharges corresponds to changing the intensity of LED light.

By changing the probability and the time constant of afterpusing, the effect on the charge distribution was qualitatively investigated. Since an afterpulse increases the charge by making an addtional pulse which is smaller than the standard one-photoelectron signal, the photoelectron peaks in the charge distribution become to have a tail. The probability of afterpulsing changes the size of the tail, while the time constant of the afterpulsing probability changes the shape of the tail.

To see the effect on the relation between variance and mean, the simulation was repeated with different N_{pe}. The parameters used in the simulation is summarized in Tab. 5.1. τ_{decay} was determined by the waveform shape, and τ_{AP} was selected to reproduce the tail of the charge distribution. The noise RMS is the same with the measured value. The other parameters were obtained by fitting. The resulting charge distribution is shown in Fig. 5.8 and it is comparable with the actual charge distribution (Fig. 5.2). The obtained relation between variance and mean is shown in Fig. 5.9. The points are on a straight line and the quadratic behavior cannot be seen. The relation keeps linear even when increasing the crosstalk or afterpulsing probability deliberately up to 40%.

5.3 Waveform Method

5.3.1 Previous Study

Gain is the number of electrons generated from one photoelectron. Therefore, the gain can be obtained once how many photoelectrons has generated a signal is known. This method extracts information concerning the number of photoelectrons contained in a signal by using a waveform shape.

Table 5.1: Parameter settings for the waveform simulation.

mean number of crosstalks from one pixel	0.01
probability of generating an afterpulse	0.14
gain including an amplifier	4.5×10^7
decay time constant of a waveform τ_{decay}	30 ns
time constant of afterpulsing τ_{AP}	20 ns
noise RMS	0.6 mV

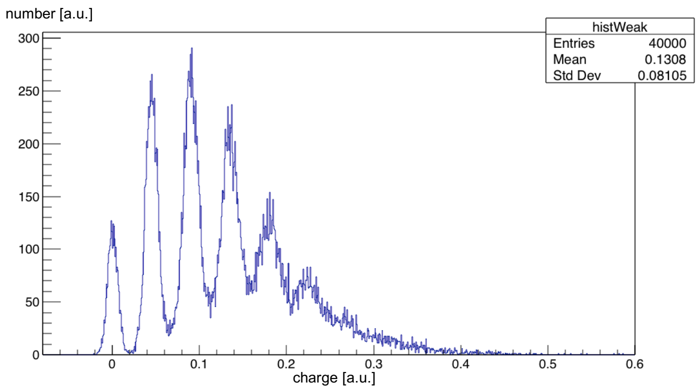

Figure 5.8: Charge distribution obtained by a simulation using the parameters shown in Tab. 5.1.

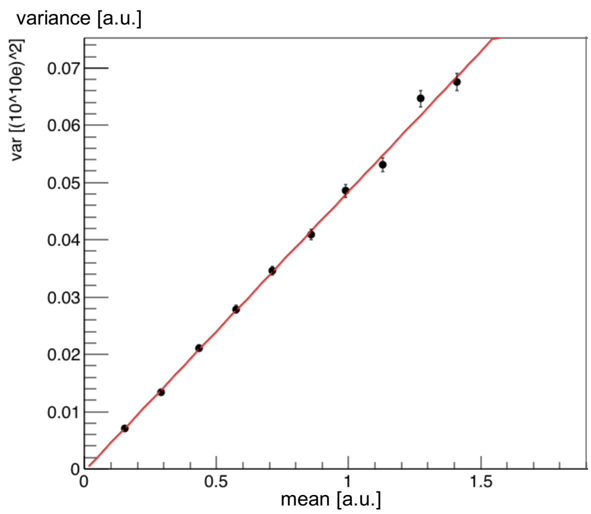

Figure 5.9: Relation between mean and variance of charge distribution obtained by a waveform simulation considering afterpulsing effect.

It is known that in the PMT case a variable proportional to gain can be extracted from the waveforms themselves by analyzing them statistically [43]. The waveform from photosensors such as PMTs or SiPMs is in principle a sequence of single-photoelectron signals. Instead of directly counting each single-photoelectron signal, an integration of signal height squared (HS) is used to represent how jagged the waveform is;

$$HS = \int dt \, \{f(t)\}^2, \tag{5.9}$$

where $f(t)$ is the amplitude of the waveform as a function of time.

As an example, a case in which the signals from each photoelectron are completely separated over time is discussed. When there are two peaks from photoelectrons and they do not overlap with each other, HS is

$$HS = 2 \int dt \, \{f_{1\text{pe}}(t)\}^2, \tag{5.10}$$

where $f_{1\text{pe}}$ is the waveform of one photoelectron. $f_{1\text{pe}}$ does not always have the same form because the distribution of the arrival time of each electron differs from time to time. But when the gain is large enough, the shape of $f_{1\text{pe}}$ is almost same owing to the large statistics of the electrons. Thus $f_{1\text{pe}}$ is assumed to be proportional to the gain;

$$f_{1\text{pe}}(t) \propto G. \tag{5.11}$$

Then,

$$HS = N_{\text{pe}} \int dt \, \{f_{1\text{pe}}(t)\}^2, \tag{5.12}$$

$$Q = N_{\text{pe}} \int dt \ \cdot f_{1\text{pe}}(t), \tag{5.13}$$

and these equations lead to

$$G \propto \frac{HS}{Q}. \tag{5.14}$$

In reality, some signals from electrons overlap with each other. For making HS sensitive to the arrival time difference of the signals, the derivative of the waveform is useful. The second derivative is used in the previous study because the correlation with gain becomes strongest.

The advantage of this method is that a dedicated light source is not needed in constrast to the other methods where one needs LEDs which emit photons following Poisson statistics, or appropriate weak light source which enables you to see a clear one-photoelectron peak.

5.3.2 Validation Test

Before considering applying this method to the SiPM case, the validation test with PMT was conducted. Some PMTs in the LXe Calorimeter were read out by WaveDREAM boards, and LEDs in the calorimeter were used as a light source. The sampling frequency of the

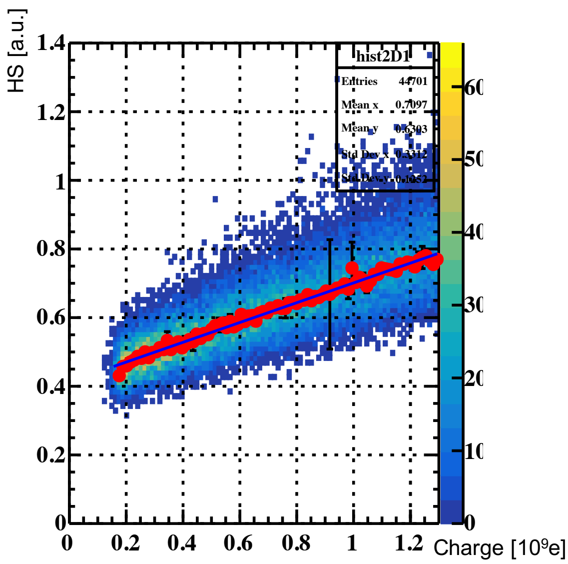

Figure 5.10: Linear relation between the charge and HS obtained by PMTs in the calorimeter. The slope corresponds to the PMT gain.

waveform digitizer was 1.2 GHz. In order to check the linearity between HS and charge in a wide range, LED intensity was changed and roughly 30 to 500 photons entered each PMT. The second derivative was used to calculate HS so that much information of the arrival time difference can be extracted. The linearity was confirmed as shown in Fig. 5.10.

In order to see the correlation with the gain, data must be taken with different gain. Seven different high voltage configurations were used to realize the different gain sets. For each high voltage set, the HS vs charge plot was made and the slope was calculated for each set. Fig. 5.11 shows the correlation between the slope and the gain obtained from the usual variance vs mean relation. The cause of the small discrepancy from the linear relation is not clear, and the dependence is different channel by channel. Although it is not a complete proportional relation, the gain can be monitored once the relation for each channel is measured beforehand.

5.3.3 Application for SiPM

Applying this waveform method for the SiPM is not straight-forward because it has so-called correlated noises as explained in Sec. 4.1.3. A pulse from a crosstalk is almost simultaneous with its primary signal, and the assumption that each pulse can be separated is no longer reasonable. The second effect is afterpulsing and the problem is that the size of the signal from an afterpulse depends on its generation time. In addition, when considering finally applying this gain monitoring method for the LXe Calorimeter, a large noise will change the waveform. How the noise contributes to this method must be examined. For

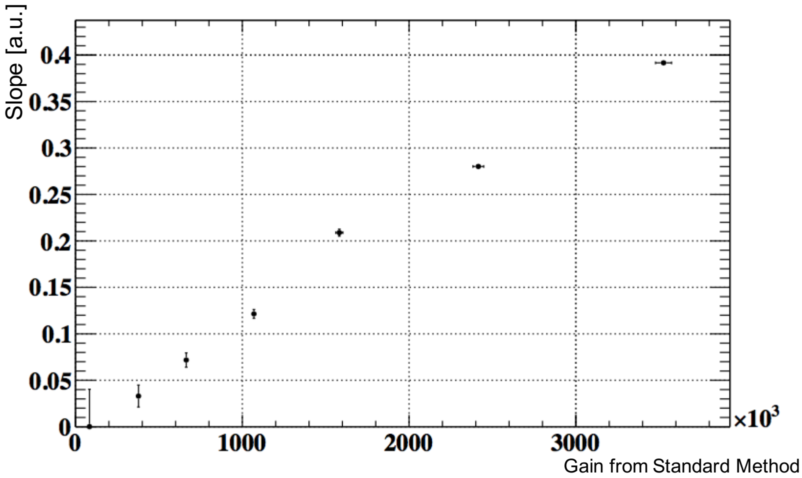

Figure 5.11: Correlation between the obtained slope and the gain.

these reasons, a new modeling of the SiPM waveform is discussed in this section.

First let's discuss how to treat crosstalk. Crosstalk occurs almost completely simultaneously with the original hit. When N_{pe} pulses completely overlap, HS and charge become

$$HS = \int dt\, \{N_{\mathrm{pe}} f_{1\mathrm{pe}}(t)\}^2 \tag{5.15a}$$

$$= N_{\mathrm{pe}}^2 \int dt\, \{f_{1\mathrm{pe}}(t)\}^2, \tag{5.15b}$$

$$Q = N_{\mathrm{pe}} \int dt\, \{f_{1\mathrm{pe}}(t)\}, \tag{5.16}$$

so now the relation between charge and HS is not linear, and HS is quadratically depends on charge.

The signal of an afterpulse is smaller than the one photoelectron signal. When smaller signals come without overlapping, HS and charge does not scale equally and HS is more affected than charge.

The effect of noise is estimated assuming white noise for simplicity. The white noise is cancelled when it is integrated;

$$\int dt\, V_{\mathrm{noise}}(t) = 0, \tag{5.17}$$

where $V_{\mathrm{noise}}(t)$ is the height of the noise waveform at time t. While it does not change the charge of the signal waveform, it affects HS as follows;

$$HS = \int dt\, \{f(t) + V_{\mathrm{noise}}(t)\}^2 \tag{5.18a}$$

$$\simeq \int dt\, [\{f(t)\}^2 + \{V_{\mathrm{noise}}(t)\}^2], \tag{5.18b}$$

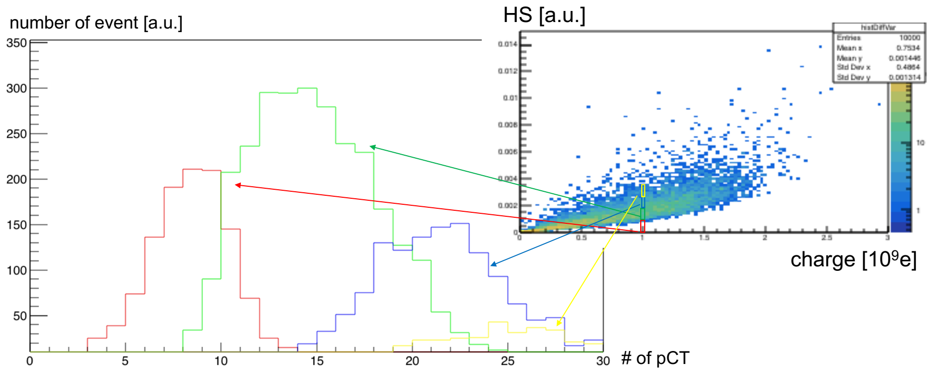

Figure 5.12: Simulated number of prompt crosstalk events for different regions in a HS vs charge plot. The number of prompt crosstalk is large in high HS region.

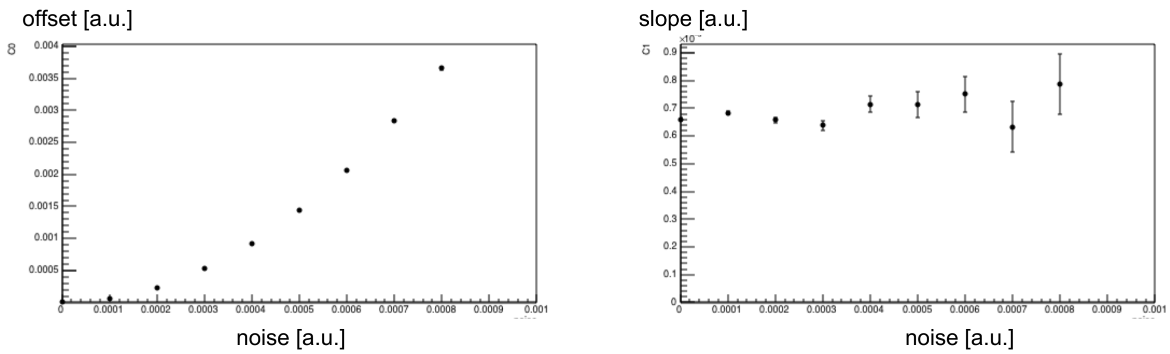

Figure 5.13: Offset (left) and the slope (right) of the HS vs charge plot. Effect of noise can be seen only in offset.

where the term $\int dt\, f(t)V_{\text{noise}}(t)$ is neglected assuming the frequency composition of a signal is slow enough compared to that of noise. Since $\int dt\, \{V_{\text{noise}}\}^2$ does not depend on N_{pe}, the white noise works as a constant term in the HS-charge relation.

Simulation

These effects are validated by a toy Monte-Carlo simulation. First the crosstalk is simulated and it is found that a tail in large HS appears owing to crosstalk. Figure 5.12 shows that the number of prompt crosstalk is actually large in the large HS events.

The noise effect is also confirmed. A random noise which follows Gaussian distribution is added to the signal. With a large noise level, the offset becomes large but the slope does not change as shown in Fig. 5.13.

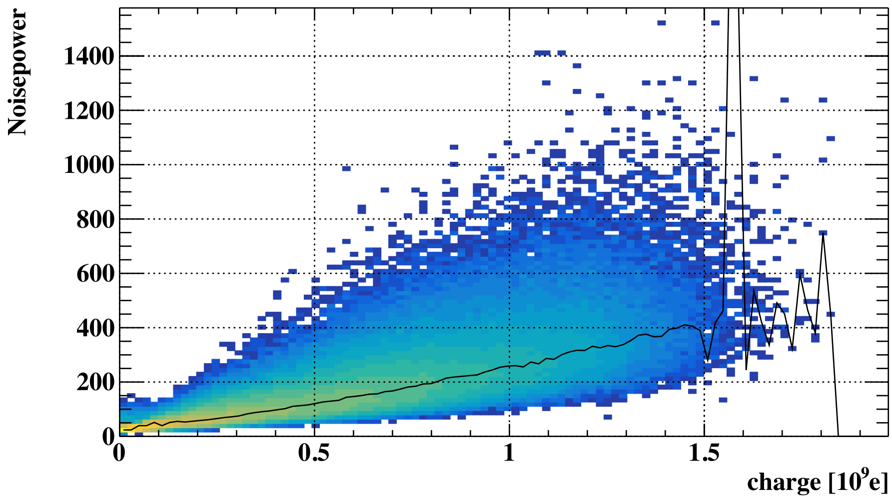

Figure 5.14: HS vs charge plot for data [41]. The blackline describes the peak positions of the histogram projected to the y axis. The 2D histogram is broad owing to the prompt crosstalk and the afterpulsing. The offset is considered to be due to the noise. The distribution is quadratic.

Test

The setup is the same as that for the statistical method which is explained in Sec. 5.2.2. The sampling frequency was 1.6 GHz. The waveform of SiPM was obtained changing LED intensity. The obtained HS vs charge plot is shown in Fig. 5.14. The distribution is broader in HS direction especially in the large charge region, which is considered to be due to the crosstalk effect. The offset exists but it is smaller than the PMT case, because the noise level is lower comparing to the measurement of the PMTs in the LXe Calorimeter. The overlapping makes the quadratic shape.

In order to extract the gain-related information from this plot, the slope around the origin was calculated. First the peak positions at each x bin were estimated by fitting the histogram projected to y axis around the peak with a Gaussian function, and then the peaks are fitted by a quadratic function. The first order coefficient corresponds to the slope at the origin. This measurement was repeated nine times and the bias voltage was changed every time. Since gain is known to have a linear relation with overvoltage, the correlation of the extracted slope and gain can be confirmed by checking the relation between the slope and the overvoltage. A clear linear relation was observed as shown in Fig 5.15. Although the scale cannot be determined only by this waveform method, it can be used as a online monitoring tool.

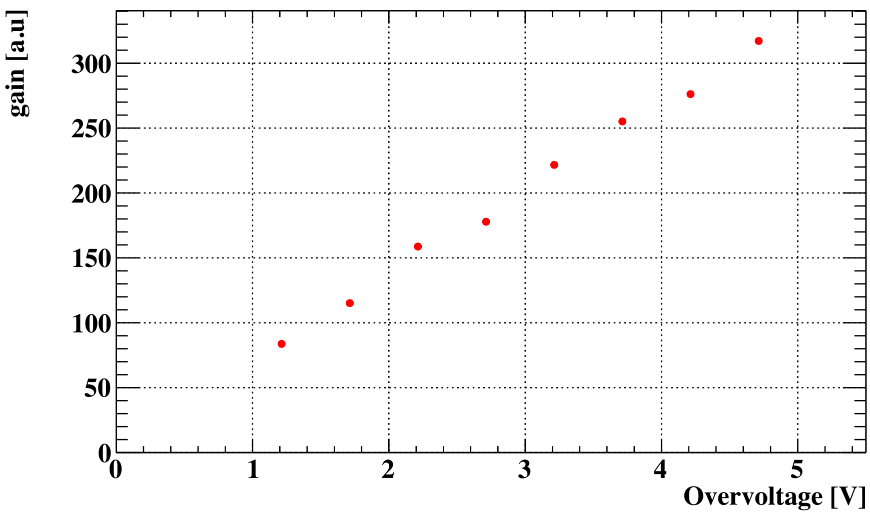

Figure 5.15: Correlation between slope of HS vs charge plot and overvoltage [41]. There is a clear linear relation.

5.4 Conclusion

Two independent methods of monitoring the gain of SiPMs were investigated. The statistical method uses a statistical property of the charge distribution from a Poisson light source. It has an advantage in the robustness to noise, and the gain can be monitored even after it is damaged by irradiation and so the usual one-photoelectron method cannot be applied. However, it still needs a clear separation of the pedestal to calculate the conversion factor and to get the absolute gain. The absolute gain was consistent with the gain from standard single-photoelectron method with the precision of 2.5% in RMS. The waveform method extracts gain-related information directly from the waveform. It does not need any dedicated setup for monitoring the gain and make the in-situ monitoring possible, although the absolute gain cannot be obtained.

Although the gain extracted by the alternative methods is confirmed to be highly correlated with that obtained from the standard one-photoelectron method by changing the overvoltage, it is not guaranteed that these methods are robust. The most important thing to be cared is the variation of the afterpulsing effect. An afterpulse is generated when a carrier is trapped by an energy level made by a lattice defect or impurity. Thus, the probability or other properties of afterpulsing can change independently of overvoltage for example by radiation damage, which means the variation of afterpulsing properties can lead to wrong estimation of the gain. In the statistical method the non-linearity of the relation between variance and mean has not been understood, and the possibility that the change of such properties as afterpulsing affects the result cannot be denied. The waveform method directly uses the waveform and it is very sensitive to afterpulses. These effect should be carefully treated and it would be the next step to do.

Chapter 6

PMT Monitoring

In 2018 and 2019, the MEG II collaboration conducted pilot runs, where the performance of the detectors were evaluated with a limited number of readout electronics in priparation for the coming physics run. A response of the LXe Calorimeter variates owing to a change in a Xe purity or responses of photosensors. In order to achieve 1% energy resolution, photosensor calibration parameters such as gain and QE must be monitored with good precision. The photosensors were monitored by LEDs and alpha ray sources as explained in Sec. 4.3.1 during the pilot runs. It was necessary to deal with some problems for a long-term operation of the detector such as a long-term decrease of PMT gain. This chapter focuses on the PMT monitoring in the pilot runs.

In the first section the purpose of each run is explained and the requirements for the PMT calibration is discussed. Two kinds of calibration, the alpha ray calibration and the LED calibration are compared and the precision is discussed in the second section. Some features in the change of PMT response were observed during the pre-engineering runs, and they are discussed in the third section. Among those features, the investigation of the decrease of the PMT response by muon beam is one of the main objectives for the run in 2019 and it is discussed in the fourth section.

6.1 Pre-Engineering Run

6.1.1 2018

The main purposes of the pilot run in 2018 are as follows:

- measure the energy spectrum of the gamma ray with the nominal intensity muon beam ($7 \times 10^7\,\mu$/s)
- measure the energy resolution at 17.6 MeV by the CW-Li calibration
- measure the position resolution by the CW-Li calibration
- evaluate the performance of the pileup reduction using the muon beam of various intensities

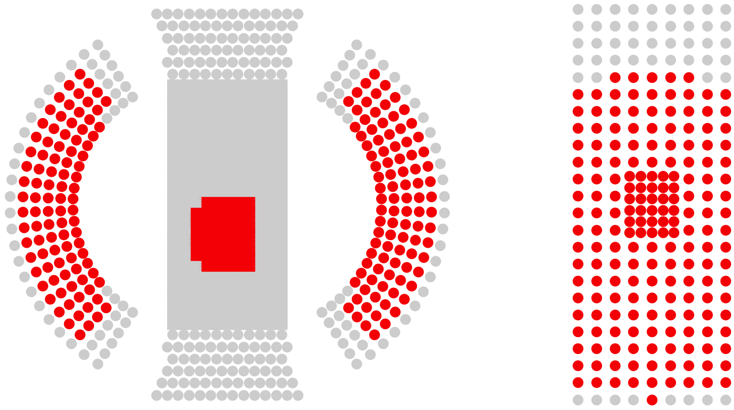

Figure 6.1: Photosensors read out in the pilot runs.

- check the stability of a photosensor response under high muon beam rate environment

The important point for the PMT calibration is that there were many activities in different environments. The PMT response can change when the muon beam intensity or the magnetic field changes. The beam intensity was changed for the study of the pileup reduction. The CW-Li calibration runs were taken under different magnetic field conditions on account of the instability of the magnet for the beam transportation. It was required to follow the change of the environment and connect the gain history with appropriate points.

6.1.2 2019

In 2018, the size of the response of both PMTs and SiPMs decreased. One of the main purpose for the pilot run in 2019 was to investigate the decrease problem. Since the investigation of the photosensors is the target in 2019, a good calibration precision is required. As for SiPMs, what is decreasing is considered to be the PDE for VUV light. In order to measure the VUV response of the SiPMs, optical properties of LXe such as light yield must be known. Since the PMTs provide important information on the optical properties of the LXe, the precision of the calibration was the key point for the study of the SiPM response.

6.1.3 Readout Region

Since the number of electronics was still limited in the pilot runs, only a part of the photosensors were read out. The sensors read out in the pilot runs are shown in Fig. 6.1. 640 SiPMs and 350 PMTs were read out.

6.1.4 Requirement

Channel by Channel Calibration

Wrong calibraiton of the PMTs does not affect the position reconstruction because it is based on the photon distribution on the incident face. However, the reconstruction of energy would depend on the gamma ray position when the PMTs are wrongly calibrated channel by channel. It would result in worse energy resolution, being affected by the fluctuation of the electromagnetic shower development. The effect of the precision of the photosensor calibration on the performance of the LXe Calorimter was studied using Monte Carlo simulation. Signal gamma rays were injected to the LXe Calorimter, and the propagation of the scintillation photons were simulated. A Gaussian fluctuation was added to the detected number of photoelectrons of each sensor. Since the statistical uncertainty of the estimation of SiPM response has already been evaluated in Ref [44], the fluctuation added to the number of photoelectrons detected by SiPMs was fixed to the evaluated value, 4%. The individual difference of the measured PMT QE is relatively 26% in standard deviation, which means the maximum error of the QE calibration is 26%. Therefore, the fluctuation added on the PMTs ranged from 0% to 20% The energy was reconstructed according to the procedure explained in Sec. 4.2.3. The reconstructed energy is shown in Fig. 6.2, and the following function was fitted to the spectrum;

$$f(x) = \begin{cases} A\exp\left(\frac{t}{\sigma^2}\left\{\frac{t}{2}-(x-x_0)\right\}\right) & (x \leq x_0+t) \\ A\exp\left(-\frac{(x-x_0)^2}{2\sigma^2}\right) & (x > x_0+t) \end{cases} \tag{6.1}$$

where A means a scale, x_0 means a peak position, t means a transition point, and σ represents energy resolution. The low energy tail is due to interactions with material in front of the fiducial volume and shower escapes mainly from the inner face. In Fig. 6.3, the resolution parameter σ is shown as a function of the size of the additional fluctuation which corresponds to the calibration precision. When the fluctuation becomes larger than 5%, the resolution becomes worse and the estimated resolution fluctuates much. The large fluctuation of the estimated resolution is considered to be because the position dependence of reconstructed energy becomes larger when wrongly calibrated PMTs accidentally distribute locally. Although systematic errors caused by bad channels or position dependence might have larger impact on the resolution, at least the statistical precision of channel by channel calibration should be under 5%.

Stability of Averaged Response

The averaged response of all the PMTs provides information on the light yield of LXe or energy scale of the calorimeter response.

In the MEG experiment, energy scale was calibrated by the 55 MeV peak of the CEX reaction and monitored by the 17.6 MeV peak of the CW-Li reaction and energy spectrum of background gamma rays. The CW-Li calibration was conducted only about twice a week to save time. The estimation of the energy scale from the gentle slope of the background spectrum has an uncertainty caused by the finite detector resolution. Therefore, the average

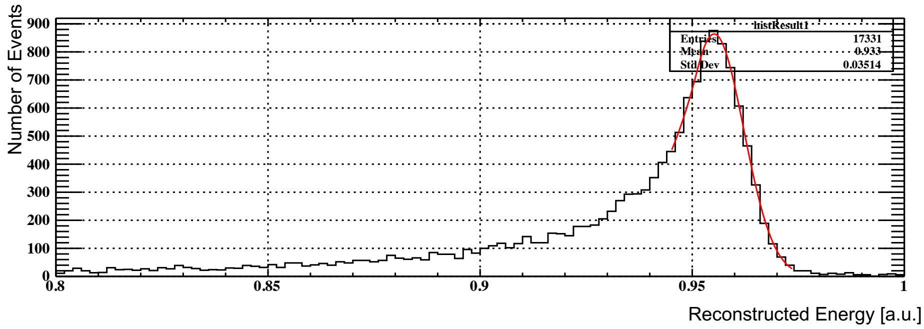

Figure 6.2: Reconstructed energy spectrum without additional fluctuation of detected number of photons for photosensors.

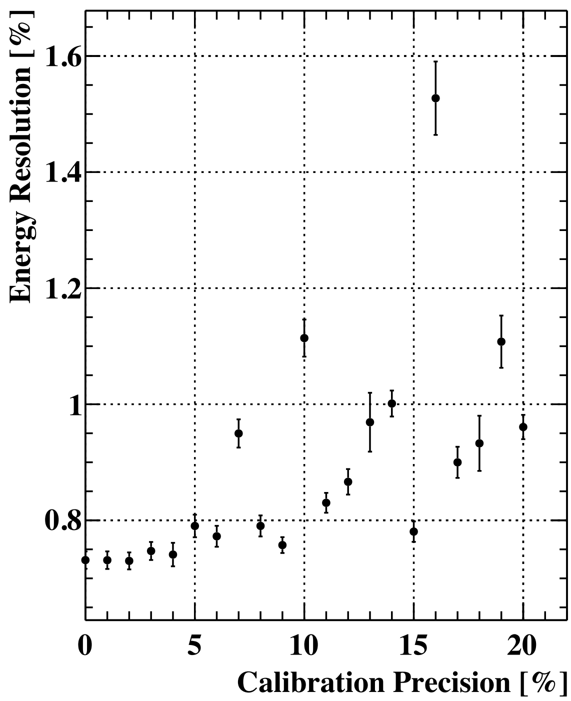

Figure 6.3: Energy resolution as a function of the size of the additional fluctuation of the calibration of photosensors.

of the PMT response to the alpha ray events was used as a auxiliary tool for frequent and accurate monitoring. The uncertainty of the energy scale was estimated to be 0.2% in the MEG experiment [45]. This level of the uncertainty should be achieved also in the MEG II experiment.

As for the pilot run in 2019, the light yield monitoring was also important for the investigation of the problem of the SiPM response to VUV light. Since the response to the VUV light can be measured only using the scintillation of the LXe, VUV response of photosensors and the light yield of LXe cannot be distinguished from each other. If the variation of response to VUV light is consistent with that to LED light, it is natural to think that there is no wavelength dependence of the variation of the response and that the light yield of LXe is constant, because the response to light from LEDs is independent of the LXe property. On the other hand, the distinguishment is impossible if the variation of response to VUV light is inconsistent with that to LEDs. In that case an upper limit of the light yield variation can be set by the inconsistency. The VUV response of the SiPM was found to have decreased by absolutely 3% while no variation of the gain was observed [44] [46]. In order to confirm that it is not the decrease of light yield but the decrease of the SiPM response, the consistency of the PMT response to alpha rays and LEDs should be measured within a precision of 1%.

6.2 Calibration Methods and Precision

There are two kinds of calibration sources for the photosensors installed in the LXe Calorimeter: alpha ray sources and LEDs. The principle of the calibration is explained in Sec. 4.3.1. Here the advantage and the disadvantage of the two calibration methods are compared and the statistical precision and the possible systematic errors of each calibration are discussed.

6.2.1 Alpha Ray

A variation over time and an individual difference of VUV response is calibrated by alpha ray signals. The alpha ray source is ^{241}Am covered by 1.5 μm thick gold, and it emits alpha rays whose energy distribution is always same. The positions of the sources are determined by the position of the wires and they do not move. Thus, they are ideal VUV-photon sources which provide constant photon distribution. Furthermore, the absolute size of the signal for a certain number of photons can be obtained because the absolute light yield is known. Since the energy distribution is not monochromatic on account of the energy loss in the gold cover, the spectrum is calculated by the Geant4 simulation and its mean is compared to that of measured distribution.

The short-term stability of the calibration was estimated by repeating some measurements under the same condition. The mean of the charge distribution for alpha ray events was obtained for each PMT. The measurement was repeated 11 runs in 2 days. The standard deviation of the mean values for 350 PMTs is shown in Fig. 6.4. It shows that the PMT response to the alpha ray is stable within 4% in a short term. The stability of the averaged response of all the PMTs was 0.2%. The required precision has been achieved at least from the point of view of the short-term stability.

It is notable that there may be a systematic error in the calibration. From the point of view of the energy scale monitoring, it is affected by the characteristics of the LXe because the light yield, scattering length or absorption length of LXe depends on the purity and can vary over time. It is therefore difficult to reproduce the detector environment in the simulation. The noise of the readout electronics or the bias caused by trigger threshold can also change over time. From the point of view of a channel-by-channel absolute PDE measurement, those which do not change over time also affect the measurement, such as the reflection by inner walls or PMT surfaces, and the distance between an alpha source and a PMT, because the simulation input can be different from the actual reflectance or the alignment of the components.

6.2.2 LED

Although the absolute number of emitted photon is unknown, the variation of the PMT response can be tracked by the response to LED light. The LED light has three advantages compared to the alpha ray as a calibration source. The first one is that the charge distribution is simply Poisson distribution of the number of photons, and thus the precision of the mean estimation is good compared to the broad distribution of the alpha ray spectrum. The second advantage is that large amount of photons are available, which also leads to good precision. The third advantage is that the data can be taken triggering on the LED flashing, while the timing of alpha ray events is not known. It makes it possible to take calibration data even under muon beam.

The short-term stability of the monitoring by LED was also estimated by repeating the same measurement 17 times. Figure 6.5 shows the standard deviation of mean of charge distribution for constant intensity LED runs. The typical number of photons detected by a PMT is 700. The short-term stability within 1% was confirmed.

Although the stability is better than the alpha ray calibration, it should be noted that it is the response to visible light and it can be different from that to VUV light. It is notable that there could be long-term instablity in the LED output or variation of the baseline of the waveform.

6.3 Cause of Variation

There are some features of the variation of the PMT response which are known from the experience of the MEG experiment. Those variations were investigated and tracked by the alpha ray or the LED light during the pilot runs.

6.3.1 Effect of Magnetic Field

In 2018, the CW-Li calibration runs were taken under three different configurations shown in Tab. 6.1 The magnetic field generated by the COBRA magnet is symmetric for the plane on the target position perpendicular to the beam axis. The upstream side of the LXe detector has a non-negligible effect from the stray field from the BTS, which transports the muon beam to the MEG detector.

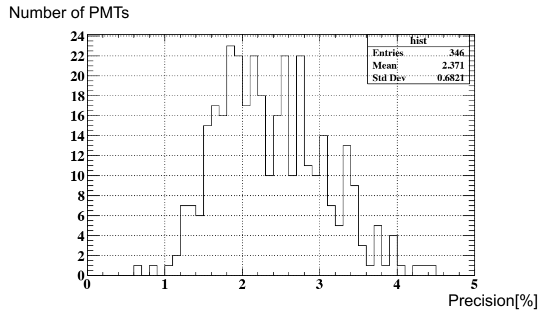

Figure 6.4: Standard deviation of response to alpha ray measured 11 times. In each measurement the mean of the charge distribution is converted to the number of photoelectrons, and then compared to that of simulation.

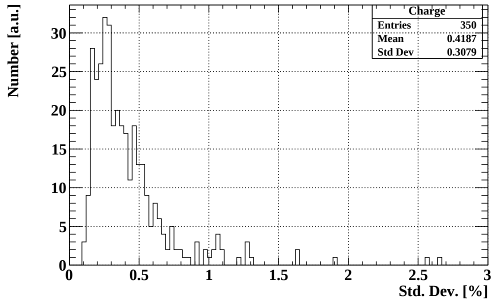

Figure 6.5: Standard deviation of mean of charge distributions for constant intensity LED runs taken 17 times.

Table 6.1: Magnetic field configurations

COBRA	BTS
off	off
on	off
on	on

The dynode structure of PMTs is optimized for the efficient multiplication. The gain and the collection efficiency is expected to decrease under the magnetic field because the electron trajectory will be modified. The tolerance to the magnetic field was measured by the producer, the Hamamatsu Photonics, as shown in Fig. 6.6. The amount of decrease depends on the direction of the magnetic field owing to the metal channel dynode structure. The magnetic field calculated for the different PMT locations is shown in Fig. 6.7. The PMTs are rotated to the direction where the effect from the magnetic field becomes minimal.

The PMT response was measured under different magnetic field configurations. The size of the signal from the nearest alpha source under COBRA and BTS B-field is compared to that without B-field, and it is shown in Fig. 6.8. The response of the PMTs especially at the edge of the outer face decreases by the B-field. The asymmetry between the upstream and downstream side is because the BTS compensates for the B-field produced by COBRA in the upstream side.

6.3.2 Short-term Variation under Muon Beam

The PMT charge for LED light changes under high rate signals of gamma rays from the target. There is a correlation between the size of the charge variation and the intensity of the muon beam as shown in Fig. 6.9. The amount of the change under the nominal intensity (7×10^7 μ/s) muon beam is shown in Fig. 6.10.

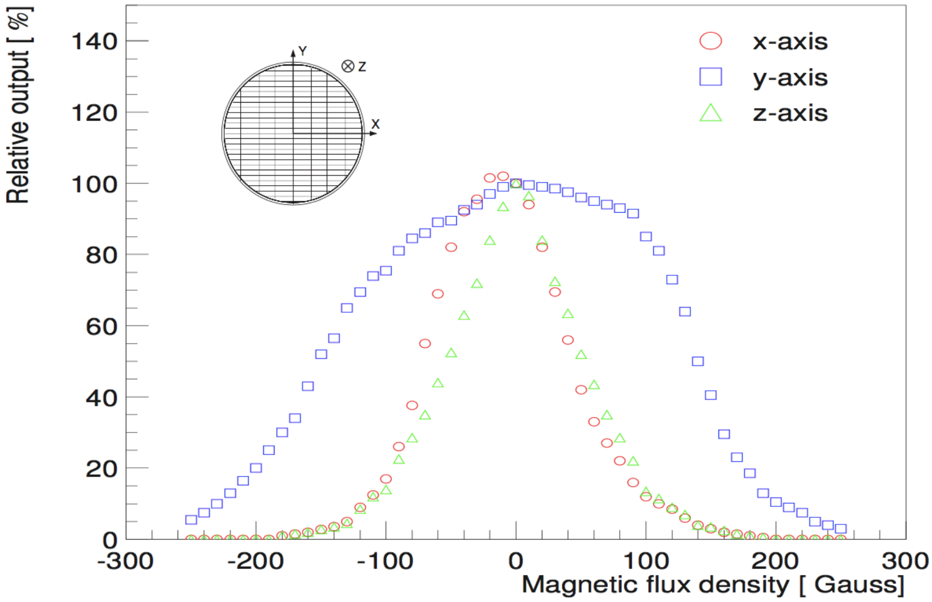

Figure 6.6: Dependence of the PMT response to the magnetic field [47]. The amount of the decrease depends on the direction of the magnetic field because it adapts a metal channel dynode structure.

Correction

The muon beam sometimes stops and restarts again owing to unpredictable stops of the proton supply or the necessity of conducting calibration runs without beam. Therefore, the time constant of the variation by muon beam is important in terms of the tracking of the photosensor response. In order to study the time development of PMT response, LED data were taken for about an hour after the opening/closing of the beam blocker. Figure 6.11 shows the response of a PMT to light from LEDs after the beam blocker is opened (top) and closed (bottom). The variation lasts for about 60 minutes.

Some correction should be applied because it is not efficient to start taking the physics data before the response stabilizes. Assuming that the physics data taking starts ten minutes after the beam blocker opens, template functions were made by fitting the variation with an exponential function,

$$f(t) = a\left[1 + b\left\{1 - \exp\left(-\frac{t - t_0 - t_{\mathrm{BB}}}{\tau}\right)\right\}\right], \tag{6.2}$$

where a and b are scale factors, t_0 is an offset parameter, τ is a time constant parameter, and t_{BB} is the time of the operation of the beam blocker. Since the size of the variation b or the time constant τ is different channel by channel, the template functions were made for each channel. The parameters a and b were determined using the initial region and the final region of the plot. The data taken in initial 10 minutes after the opening of the beam blocker are ignored for now because the variation is especially large.

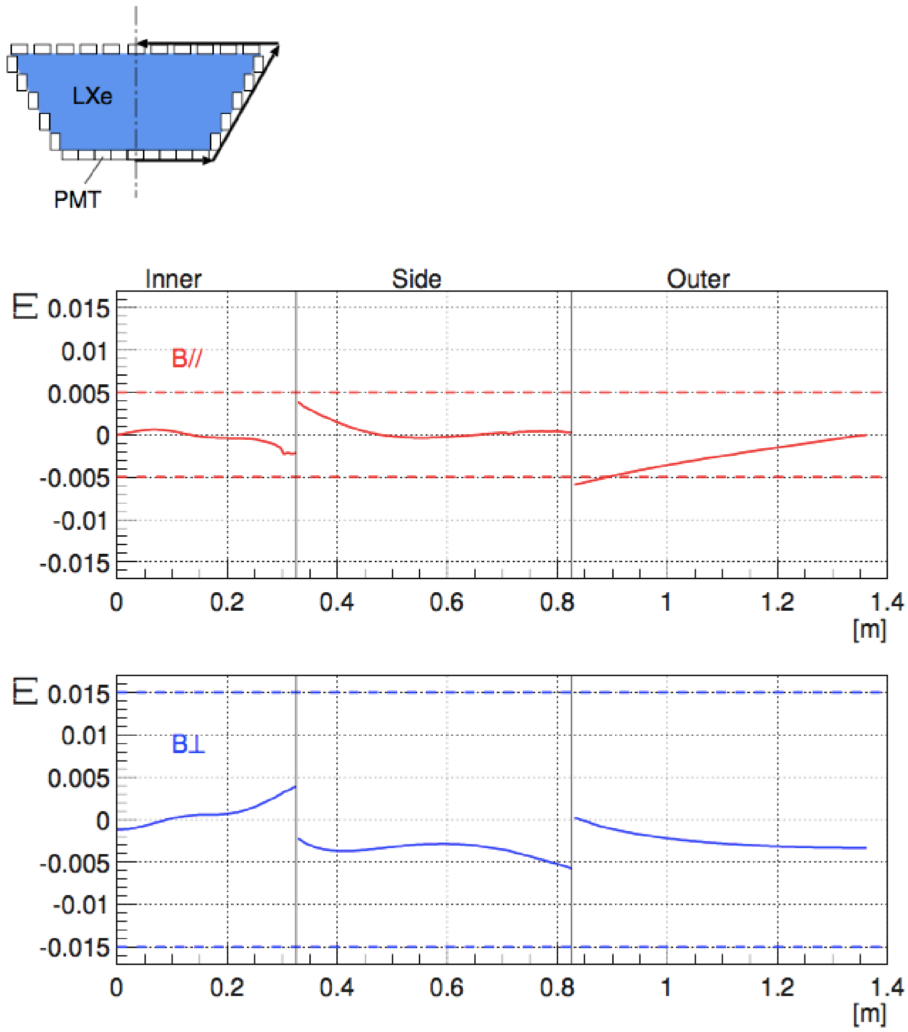

Figure 6.7: Calculated magnetic field along the boundary path of the LXe Calorimter where the PMTs are arranged [47]. The top (bottom) figure is the profile of the component parallel (perpendicular) to the tube axis. The dashed line indicates the field strength where the relative gain of the PMT is reduced by 50%.

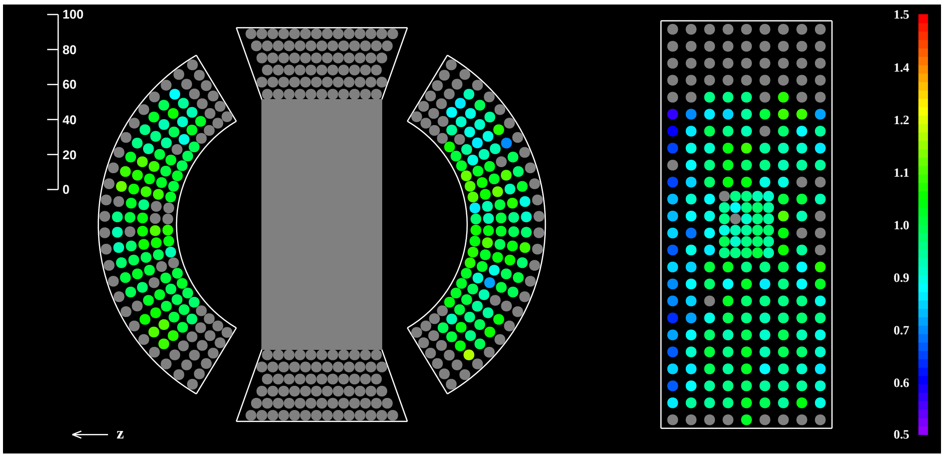

Figure 6.8: Effect of the magnetic field on PMT response to VUV light. The color shows the signal size under the magnetic field relative to that under no field.

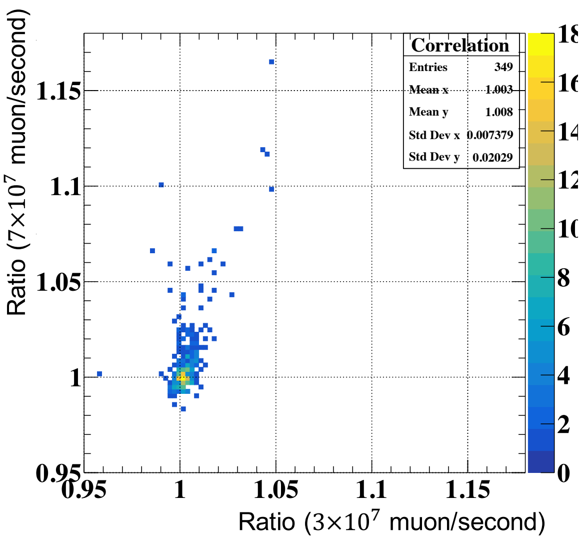

Figure 6.9: Correlation between the change of PMT response under weak and intense muon beam. The larger change can be seen under more intense muon beam.

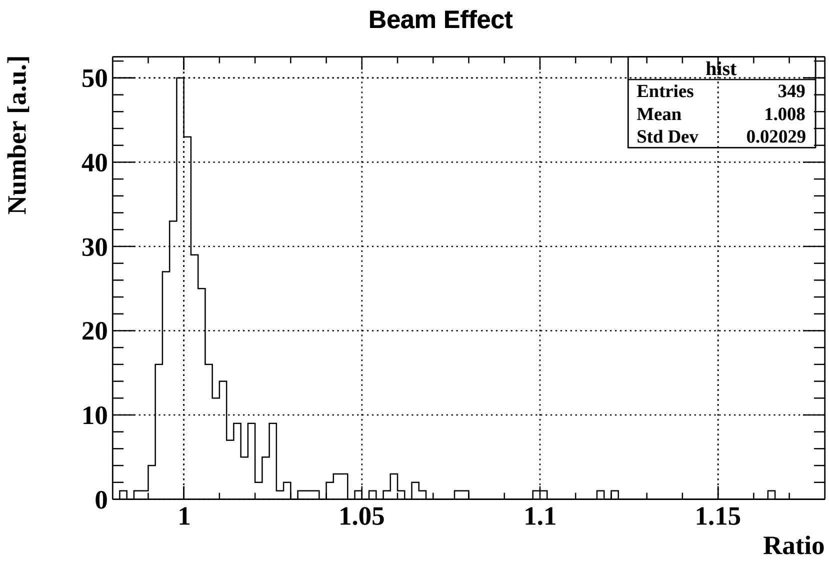

Figure 6.10: Relative change of the charge from LED light due to the high rate signals. The response of some PMTs increase under muon beam.

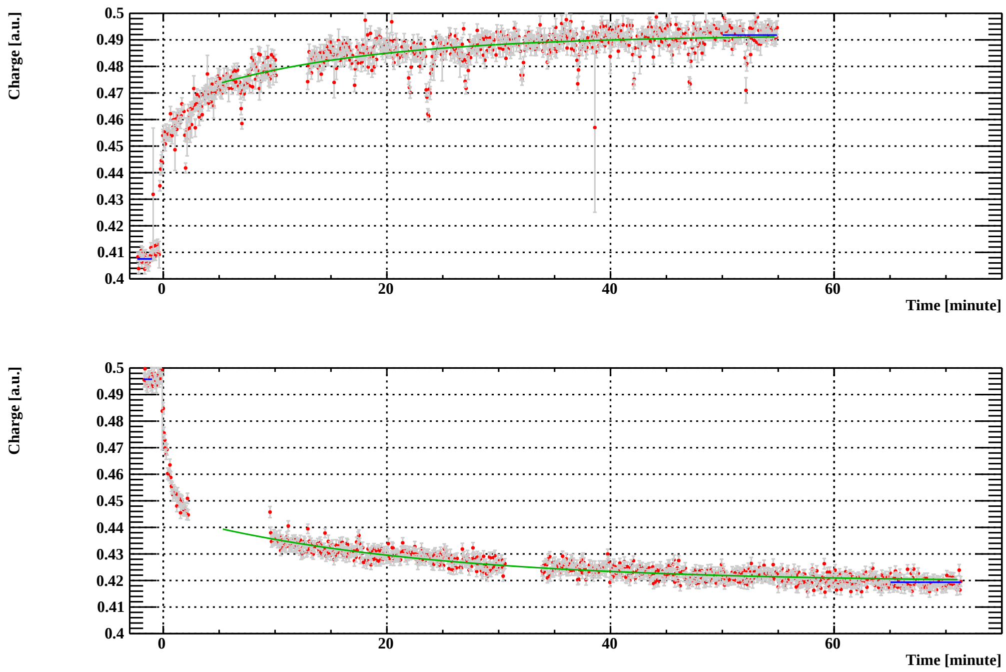

Figure 6.11: LED response after opening (top) and closing (bottom) the beam blocker. Every red point is mean of 100 actual data points. The variation lasts for about 60 minutes.

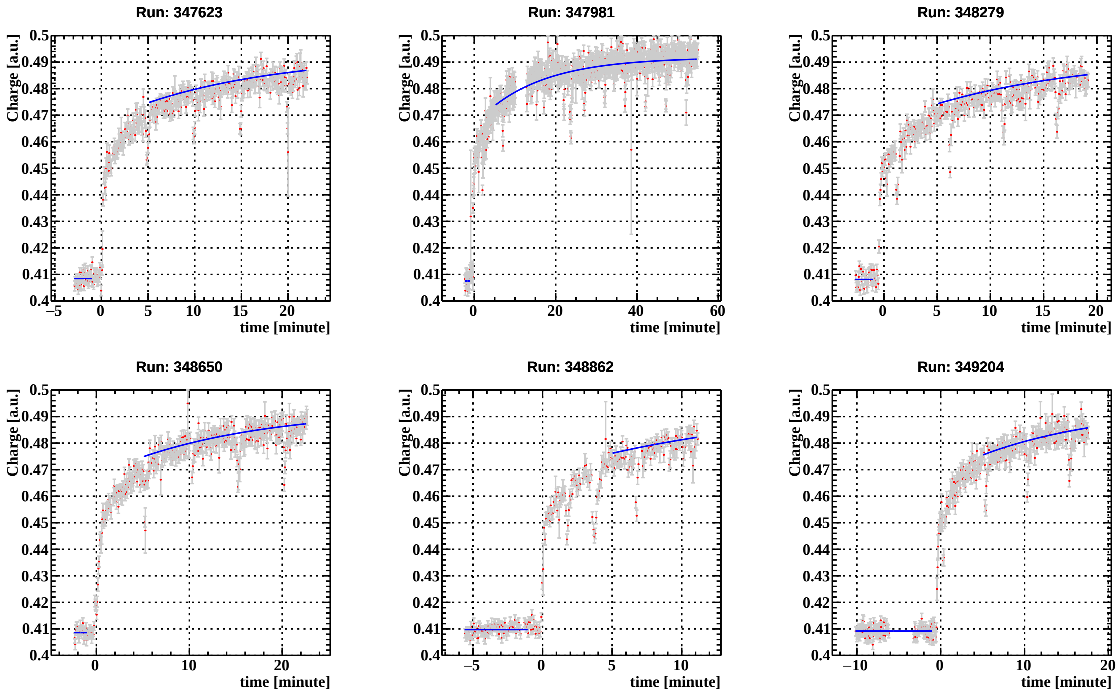

Figure 6.12: Variation of response of a PMT just after opening the beam blocker for different runs under the same intensity muon beam. Each red points is the mean of the charge of 100 events. The blue line is the template function obtained from one long run, and the function is scaled using the events before opening the beam blocker.

The obtained function was compared with the different runs under the same intensity muon beam as shown in Fig. 6.12, in order to confirm that the variation is the same every time. The parameter a was determined using the data points before opening the beam blocker, and the other parameters were fixed with those obtained from the long run. Although there is still a small discrepancy whose cause is yet to be understood, the rough shape of the time dependent variation is almost same every time. Therefore, the variation can be corrected using this template function.

However, it is possible that the change of the response to the VUV light is different from the response to LED light. The effect of the muon beam on the VUV light detection has not been studied and this would be a future task. Since the time constant of the variation is long, it might be possible to compare the response to the gamma rays from a muon decay, beween just after opening the beam blocker and an hour after the operation.

6.3.3 Aging Caused by Muon Beam

The charge response of the PMT is known to decrease under muon beam, and a rapid decrease was observed in the pilot runs. Figure 6.13 shows the variation of three observables; gain, charge for LEDs, and charge for alpha rays.

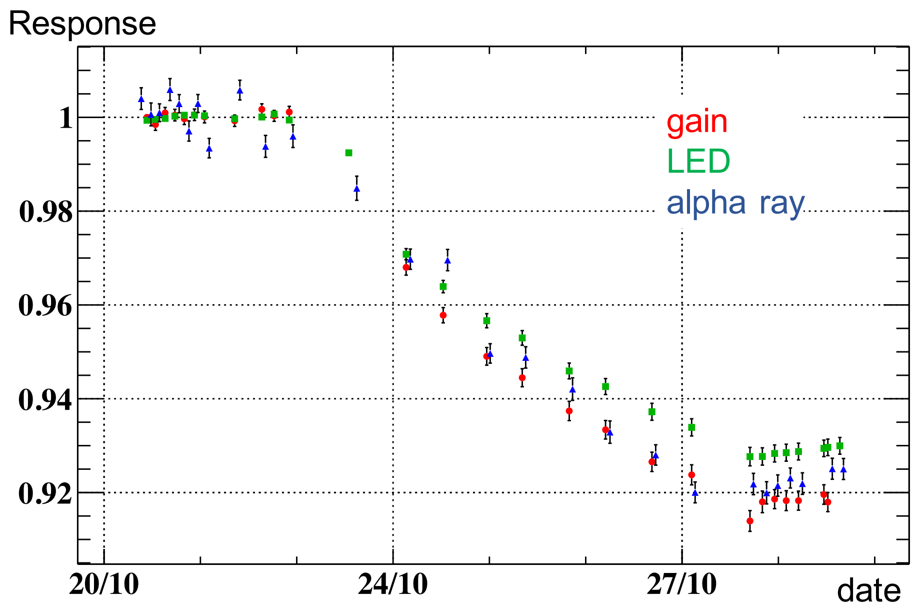

Figure 6.13: Variation of PMT gain (red circle), charge for LED (green square) and charge for alpha ray (blue triangle) under muon beam. They are normalized channel by channel, and the average of about 350 PMTs is plotted.

In a few days the response decreased by about 8%. The decreases observed for the three observables were consistent within 1% over a week. It means that the main cause of the decrease of the PMT total response is the gain decrease. If the decrease of the VUV response is caused only by the gain decrease, the alpha ray calibrations can be interpolated by LED calibration, which needs less time. However, it is also possible that there is an additional wavelength dependent QE variation. There is in fact 1% inconsistency between gain decrease and charge decrease, and it should be carefully investigated for longer period.

The decrease speed was more rapid than expected from the MEG experiment, and it is a serious problem The problem is discussed in the next section.

6.4 Gain Decrease

6.4.1 Expectation from MEG

The PMT response is known to decrease with muon beam irradiation as can be seen in the gain history during the MEG experiment shown in Fig. 6.14.

Although the decrease of the gain can be compensated by increasing high voltage, too much voltage would lead to severer damage on the PMT and would finally result in breakdown. Using the dependence of the gain on the voltage shown in Fig. 6.15, the final voltage necessary at the end of the MEG II experiment was estimated in 2013 [49]. The assumptions were as follows;

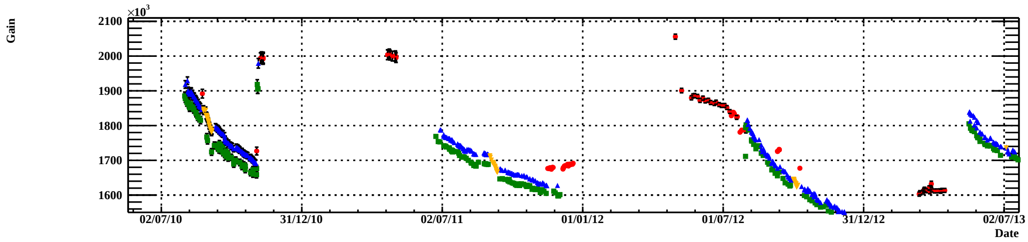

Figure 6.14: PMT gain history during the MEG I experiment from 2010 to 2013 [48]. Red circles were taken without operation of magnets. Blue triangles (green squares) were taken under (without) muon beam. Yellow inverse triangles were taken under pion beam. The high voltage was adjusted every year so that the PMTs would have high enough gain.

- Voltage is adjusted for the gain to become 1.8×10^6 at the beginning of every year.
- $G = a(V - V_0)^k$, where G is gain and V is applied voltage.
- V_0 and k does not change by irradiation.
- The decrease is exponential and the rate is proportional to the muon beam rate.
- The voltage cannot exceed 1400 V.

The result is shown in Fig. 6.16. After running for three years, the required voltage would be still below the upper limit of 1400 V for most PMTs, although for some PMTs it would have already been beyond the limit. The PMTs whose decrease rate was small were selected to be used also in the MEG II experiment because the number of PMTs decreases by 216 owing to the introduction of SiPMs on the incident face. An important point here is that it is assumed that the gain decrease rate is proportional to the muon beam rate. It has to be validated under higher beam rate.

6.4.2 Beam Rate Dependence

Figure 6.17 shows the history of response of a PMT monitored by LED in 2017. Since three different muon beam rates were tested during this period, the dependence of the decrease speed on the beam rate can be extracted. Although the decrease rate seems to decrease with irradiated time, the initial slope is fitted by linear function and the speed is extracted. In 2018 muon beam rate reached the MEG II nominal intensity ($7 \times 10^7 \mu$/s) and the decrease rate at this high irradiation environment was also extracted. As a result, the dependence is found out not to be proportional to the beam rate, and the decrease under MEG II nominal intensity is much faster than expected in 2013 as shown in Fig. 6.18.

For now there is basically no method of increasing the gain except for applying higher voltage. Decreasing the beam rate is one solution for the PMT survival, but the doubling of the muon beam rate from the MEG experiment is necessary to reach the sensitivity goal in three years. Based on the observed speed of gain decrease, the high voltage necessary after a three-years run was calculated for each PMT and it is shown in Fig. 6.19. Most PMTs would

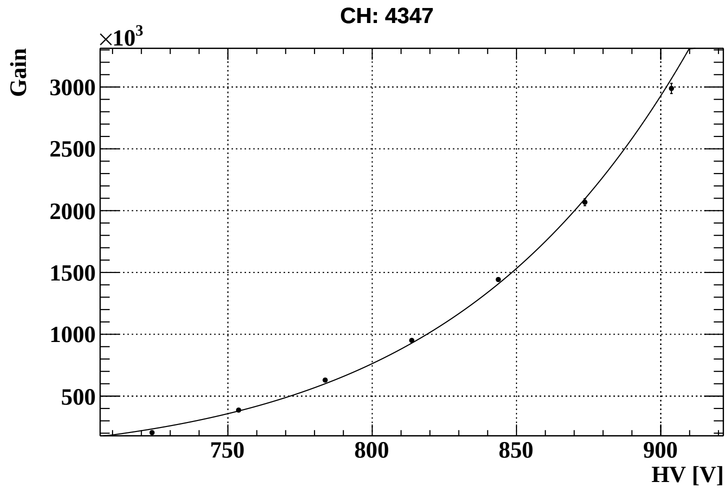

Figure 6.15: High voltage dependence of the PMT gain. The points are data including statistical uncertainty, and the line is the fitted power function. The gain is proportional to the power of applied high voltage.

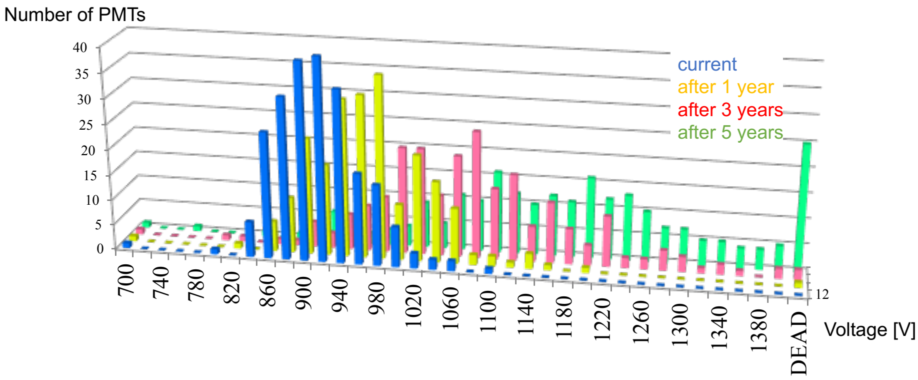

Figure 6.16: PMT high voltage necessary to keep enough gain simulated in 2013 (labels and legends replaced for visibility from [49]). Most PMTs would not need more than 1400 V after the 3 years run.

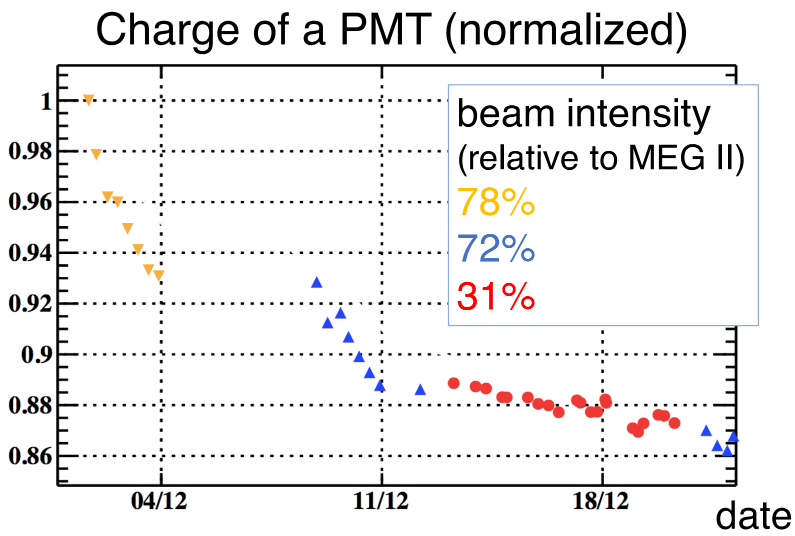

Figure 6.17: Response of a PMT monitored by LED in 2017 [48]. The yellow inverted triangles are points taken under 78% of the MEG II nominal beam rate. The blue triangles and the red circles correspond to 72% and 31%, respectively.

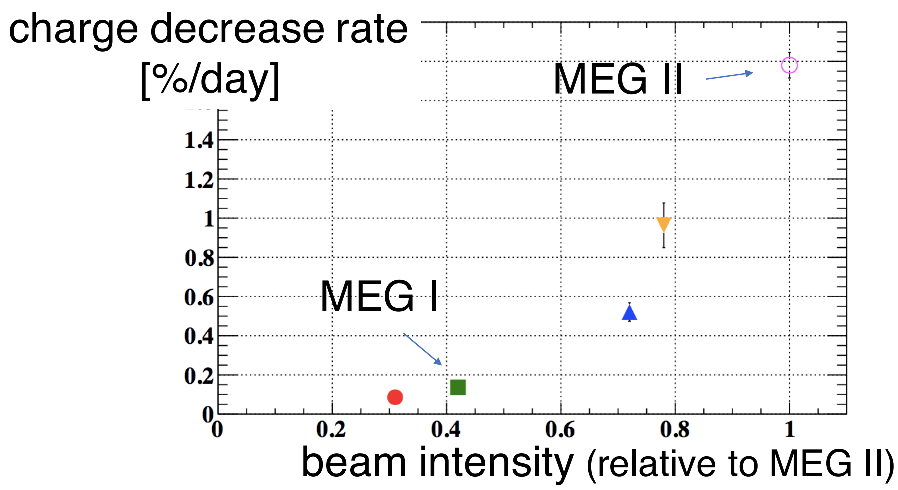

Figure 6.18: Beam rate dependence of the gain decrease rate [48]. The relation is not proportional and the decrease under MEG II intensity is much faster than expected. Note that not all of the PMTs shown in Fig. 6.1 is used in this plot because some of them were not read out in the MEG experiment or in 2017.

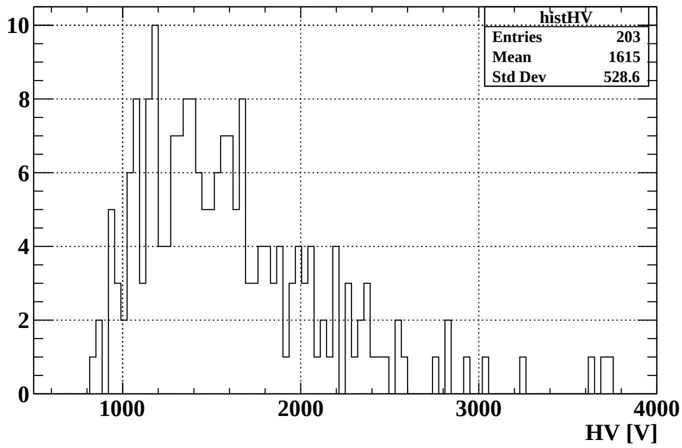

Figure 6.19: High Voltage necessary at the end of a three-years run estimated from the gain decrease speed observed with the same intensity muon beam with that in the MEG II physics run.

require more tha and they would be in dahave a risk of failure. To overcome the problem, the possibility of operating the PMTs with lower gain to prolong thir lives was studied at pilot run in 2019.

6.4.3 Gain Dependence

One possibility of the cause of the gain decrease is a degradation of dynodes in the PMT. The damage can possibly be mitigated when the number of electrons hitting the dynodes is reduced by a lower gain operation. The decrease rate of the average gain of 200 PMTs was compared under different high voltages. As shown in Fig. 6.20, the decrease rate became small under the halved gain. A recovery of the gain was observed after leaving the PMTs for several month at room temperature, but it was very small (a few percent). Using the slope of the gain decrease curve and the high voltage dependence of the gain, the high voltage necessary after the three years run was estimated channel by channel. The result is shown in Fig. 6.21 and most of the PMTs can be operated with reasonable voltage.

6.4.4 Discussion

In order to keep the applied high voltage in the safe region, it seems necessary to operate the PMTs with lower gain. The largest disadvantage of using lower gain is that the signal-to-noise ratio (S/N) becomes worse. One possible solution for this problem is to increase the gain of the amplifier of WaveDREAM boards from 1. If the major component of the noise arises between the amplifier and the waveform digitizer, the loss of the signal size can be compensated by the amplifier because the noise level does not change by the amplifier.

The noise level was actually compared between the cases with gain 1 and gain about 2.3 [50]. The result is shown in Fig. 6.22 and the total noise level increased only 13% after

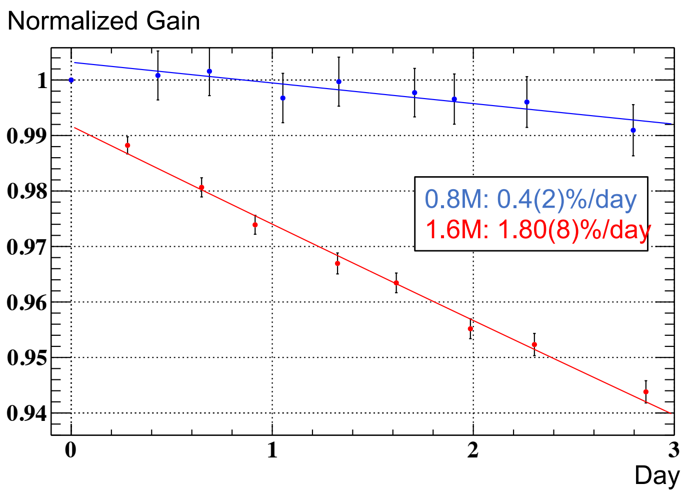

Figure 6.20: Gain decrease under the different voltage as a function of the irradiation days. Average gain of about 200 PMTs measured by LED. The decrease rate is smaller when smaller voltage is applied.

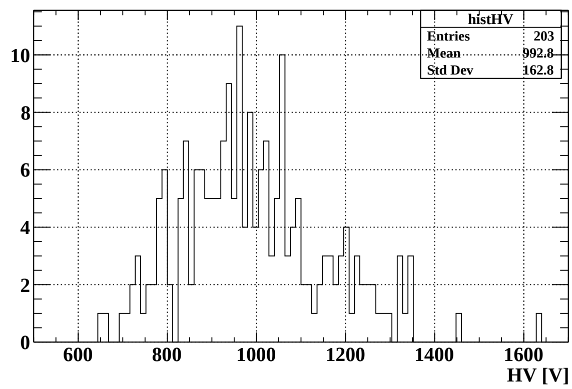

Figure 6.21: High voltage necessary after a three years run estimated from the gain decrease rate and the high voltage dependence of gain.

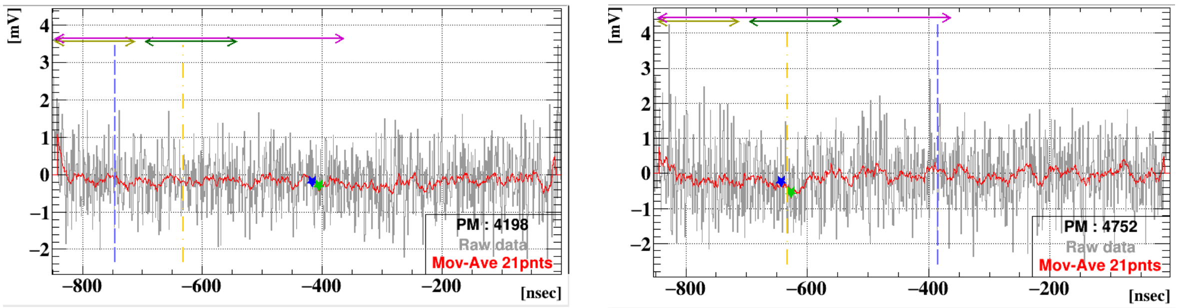

Figure 6.22: Noise waveform without an amplifier (left) and with an amplifier gain about 2.3 (right) [50]. The total noise level differs only about 13%.

inserting an amplifier. This imply that the lower gain operation of PMTs does not affect the performance of the detector.

The effect of the lower gain operation on the detector performance should be investigated using signal-like gamma rays and it is planned to be done by the charge exchange experiment in 2020.

6.5 Conclusion

The PMT response was monitored during the MEG II pre-engineering runs conducted in 2018 and 2019. The dependence on the magnetic field and muon beam was carefully investigated. The response of one PMT to alpha rays was calibrated with 4% precision. The precision of the estimation of the average of 350 PMTs was 0.2%. The response of one PMT to LED light was calibrated with 1% precision. The aging by the muon beam irradiation was found to be severer than expected from the experience in the MEG experiment, but a solution of lower gain operation was found out to be effective. The effect of the lower gain operation on the detector performance will be investigated by the CEX calibration in 2020.

Part III

Calibration of Detector Response

Chapter 7

Improvement of Charge Exchange Calibration

7.1 Motivation

Global calibration parameters necessary for the event reconstruction (see Sec. 4.2) will be extracted using the gamma rays generated in the charge exchange (CEX) reaction of pions explained in Sec. 4.3.3. For example, the position dependence of the total number of photons detected by photosensors must be corrected in order to reconstruct energy, and the correction function is made by the CEX calibration. The detector performance will be evaluated also in the CEX calibration using the extracted calibration parameters. From these points of view, the CEX calibration is the most important calibration and the precision of the calibration is the key to the best performance of the LXe Calorimeter.

In order to calibrate something, the reference value has to be more precise than the target precision of the calibration. In the case of LXe Calorimeter, the position, energy and timing of the gamma ray should be known very precisely.

A lead collimator has been developed to restrict the region where gamma rays enter for the position study [5].

The timing of the gamma ray injected into the LXe Calorimeter is estimated from that of the other gamma ray. It is detected by the pre-shower counter which consists of lead conversion plate and two plastic scintillators read out by SiPMs, whose timing resolution is 40 ps [33]. The pre-shower counter is shown in Fig. 7.1. The timing at the pion decay vertex position is calculated using the flight length of the gamma ray, and then the measured generation time of the two gamma rays is compared to each other. However, there is another uncertainty from the vertex position because the pion beam is broad in the direction perpendicular to the beam axis. It makes an uncertainty in the time of flight estimation (2×10 mm/$c \sim 70$ ps in sigma).

The energy of the gamma ray is around 55 MeV when selecting the events where two gamma rays are emitted in the opposite direction in the laboratory frame and lower energy one enters the LXe Calorimeter. More precise estimation is possible using the opening angle of the two gamma rays from a neutral pion decay because there is a relation determined by

Figure 7.1: Pre-shower counter [33]. A plastic scintillator read out by SiPMs is wrapped by a light shield.

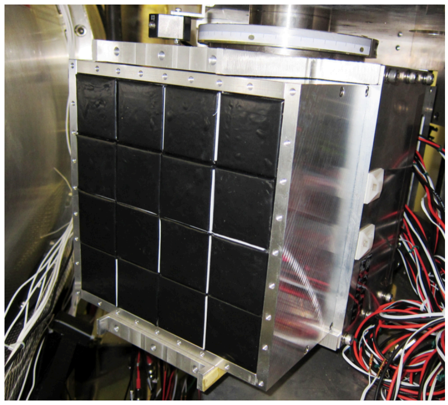

Figure 7.2: BGO counter [51]. 4×4 BGO crystals are optically connected to PMTs.

the kinematics between the opening angle and the gamma ray energy as shown in Fig. 7.3. The precision of the angle is determined by the position resolution of the LXe Calorimeter (a few mm) and the tagging detector ($\sim$ 10 mm), and the variance of the vertex position ($\sim$ 10 mm). It corresponds to an uncertainty of several hundred keV. The BGO calorimeter (Fig. 7.2) is used as the tagging detector in the energy calibration. It is a 4×4 array of BGO crystals ($46 \times 46 \times 200$ mm^3 each), each of which is optically connected to a fine mesh PMT (H8409-70 by Hamamatsu).

Thus, the estimation of the energy and the timing of the gamma ray suffer from the uncertainty of the vertex position of the neutral pion decay. In order to overcome the problem, two types of detectors were considered. The first one is a scintillating fiber detector for the charged pion beam, and the second one is an active target which made of scintillating material. They are explained in detail below.

7.2 Requirement

The role of this detector is to measure the vertex position of the neutral pion decay. The required position resolution depends on the resolution of the other detectors, and the detector geometry is optimized using simulation as described below. Since this position measurement should be done event by event, timing resolution and pileups should also be taken into account. The maximum charged pion beam rate is 1.4 MHz, which means the requirement for the timing performance is not severe, $O(\mu s)$. Another concern is the contamination in the beam. There are 26 times more electrons than pions in the beam, and they must be distinguished from the pions. In addition, the detector must be radiation hard. The CEX calibration was conducted for 10 days per month in the MEG experiment. Therefore, 50 days irradiation is assumed in the following study.

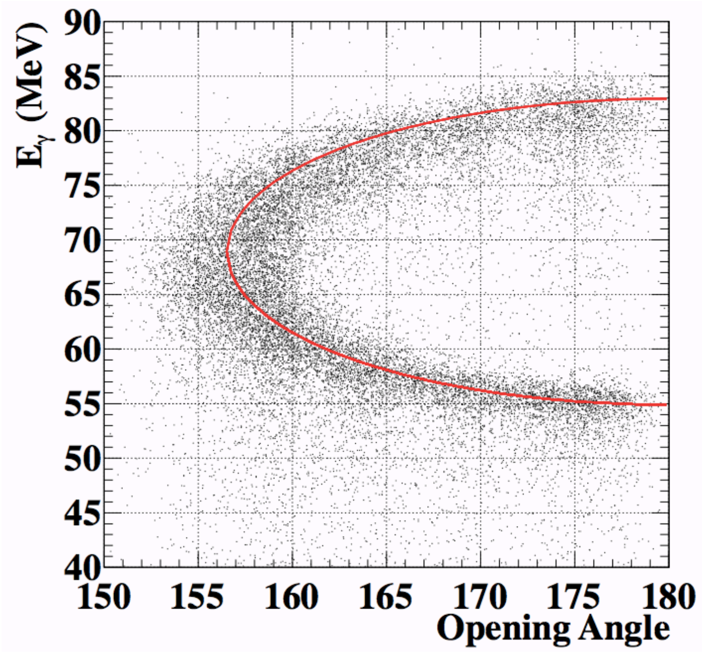

Figure 7.3: Relation between the opening angle and the energy of a gamma ray [29]. The black points are data taken in 2009 and the line is the theoretical prediction based on the kinematics.

7.3 Scintillating Fiber

7.3.1 Concept

Since the lifetime of the neutral pion is very short, the x-y position of the decay vertex is almost equal to the beam position at the target. This detector is designed to measure the beam position just in front of the target as shown in Fig. 7.4. When the charged pion goes through the scintillating fiber, the pion deposits some energy on the fiber and some scintillation photons are emitted. By detecting the photons by the SiPMs attached at the end of the fibers, discrete information of the beam position is obtained. Since scintillating fibers are very thin ($\sim 250\ \mu$m), some fibers are put together to make a bundle to read many fibers by one SiPM. One layer can measure only one dimensional position. Therefore, the next layer is put orthogonally to the previous layer to enable a two-dimensional measurement. The small thickness of scintillating fibers reduces influence on the pion beam. If the charged pion is scattered too much by the detector, the vertex position will be different from the detected position.

The detector performance was simulated using Geant4 vesion 10.3.1 [37]. In the simulation a pion beam is generated imitating the actual beam used in the CEX calibration at the MEG experiment, and the momentum and the width of the pion beam are normally distributed. The expected resolution of the calorimeter and the tagging detector is also reproduced in the simulation. The simulation setting is summarized in Tab. 7.1. The effect on the energy

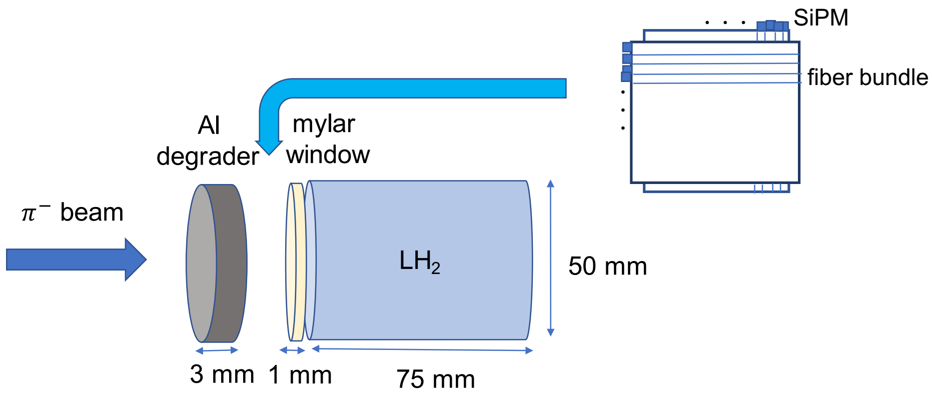

Figure 7.4: Schematic design of a pion beam monitor. Scintillating fibers detect the pion beam without affecting the beam property so much.

Table 7.1: Settings in the simulation of a pion beam position detector.

central value of beam momentum	70.5 MeV/c
fluctuation of beam momentum	3%
beam width in horizontal direction	8.5 mm
beam width in vertical direction	7.5 mm
timing resolution of pre-shower counter	40 ps
position resolution of pre-shower counter	7 mm
position resolution of BGO calorimeter	10 mm
position resolution of LXe Calorimter	O(mm) (depends on conversion depth)
physics model	`FTFP_BERT`

estimation and the timing estimation was studied for different thicknesses of the bundles. The energy and the timing of the gamma ray injected to the LXe Calotimeter were reconstructed using the reconstructed information of tagged gamma ray and the vertex position. The simulation is repeated for different bundling configurations of the fiber detector, and the reconstructed variables were compared with the true values. Accuracy was defined as the standard deviation of the distribution of the difference between the reconstructed variable and its true value. The result is shown in Fig. 7.5.

Since this type of detectors provide discrete information, highly segmented bundles lead to better position resolution. In our case, however, the improvement saturates at around 10 bundles, which corresponds to the thickness of 5 mm per bundle, because the effect of the resolution of other detectors becomes donimant.

7.3.2 Particle Identification

The negative pion beam is contaminated by 26 times larger number of electrons. These can be eliminated by the timing and the signal size.

The pions are generated from protons accelerated by a large proton cyclotron, and the

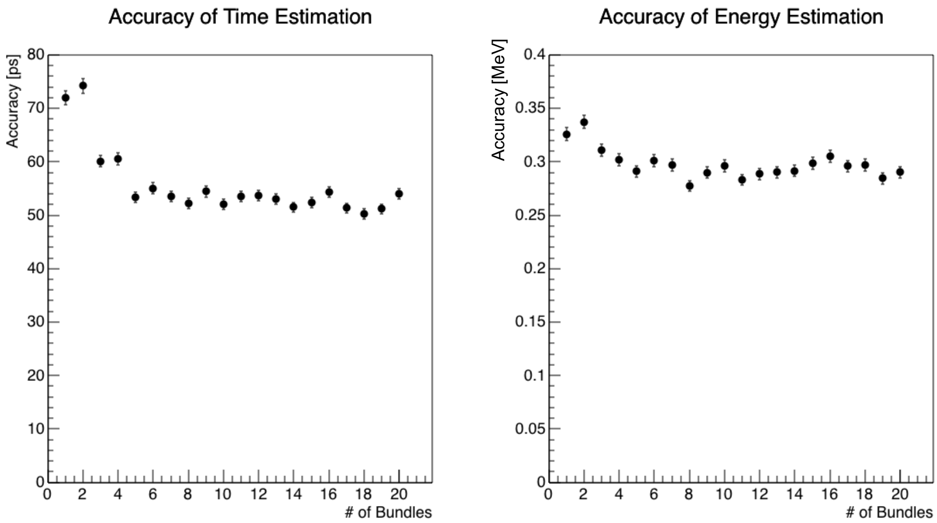

Figure 7.5: Accuracy of the estimated energy and timing of the gamma ray [52]. Although the large number of bundles leads to better estimation, ∼10 bundles (5 mm/bundle) are enough owing to the resolution of other detectors.

ejected protons have a bunch structure. Since a pion is heavier than an electron, the velocity of a pion is different from that of an electron when the momentum is the same. Thus the pions can be distinguished from the electrons by the arrival time.

The energy deposit of the pion is also different from that of the electron. The electron behaves like a minimum ionizing particle at the beam momentum of 70.5 MeV/c, while the pion does not and it deposits larger energy. The simulated difference of the energy deposit is shown in Fig. 7.6.

These methods of particle identification have been already verified using a different beamline at PSI as shown in Fig. 7.7 [53] although the momentum of the particles is $\sim$ 60% larger than our case.

7.3.3 Radiation Hardness

Since the pion beam monitor will always be irradiated by the beam, some radiation damage is expected. In addition to the charged pion beam and the electron contamination, neutrons from the CEX reaction or gamma rays from the neutral pion decay should be also taken into account. The possible effect of the radiation is discussed separately for each component; the scintillating fiber and the SiPM.

Scintillating Fiber

The light yield and the transmittance of the scintillating fiber are expected to decrease by radiation damage. It can lead to small signals and bad S/N.

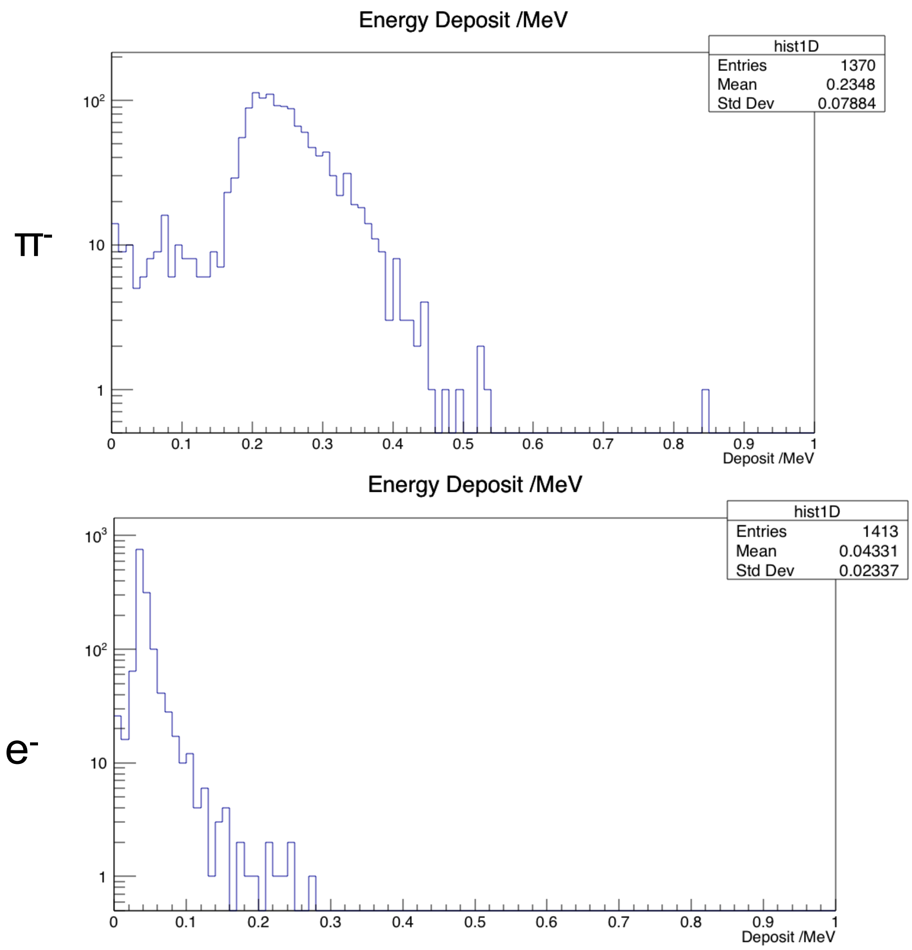

Figure 7.6: Energy deposit on 250 μm thick scintillator from pions (top) and from electrons (bottom). The signal from a pion is larger than that from an electron.

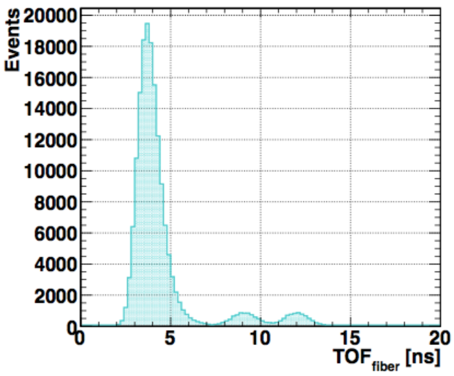

c) 500 µm fibers

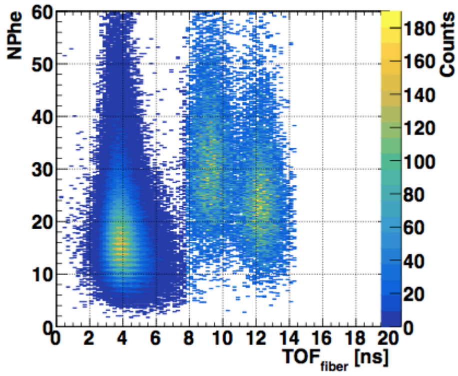

d) 500 µm fibers

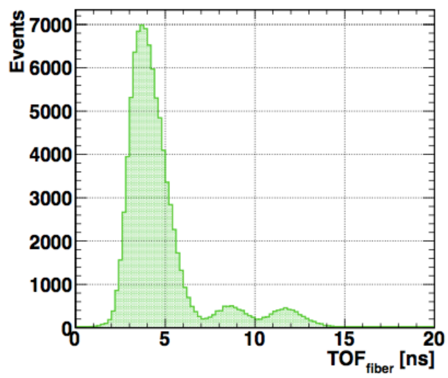

e) 250 µm fibers

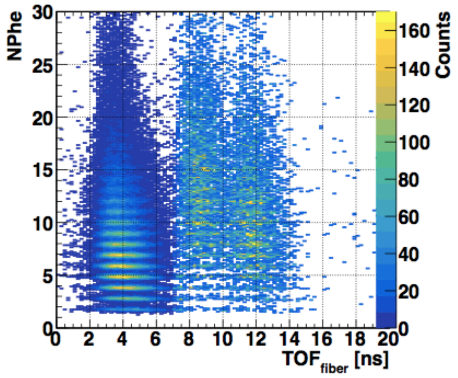

f) 250 µm fibers

Figure 7.7: Result of the particle identification test performed at the πM1 beamline at PSI using 115 MeV/c beam [53]. The three clusters are associated to electrons, pions and muons, reading the spectrum from left to right. The charge spectra of the muons and pions are scaled by a factor of twenty for visibility.

Table 7.2: Scintillation light yield of different type of plastic scintillators before and after irradiation [54].

N	Scintillator	I_0 [%]	I/I_0 [%] (3.4×10^4 Gy)	I/I_0 [%] (1×10^5 Gy)	I/I_0 [%] (after 23 days of recovery)
1	PS [a]	100	48	23	52
2	PSM-115 [b]	90–100	92	60	72
3	NE-102a [c]	120	60	45	61
4	NE-110 [c]	120	63	48	59
5	BC-400 [d]	126	56	39	61
6	BC-404 [d]	126	63	53	57
7	BC-408 [d]	124	61	46	57

[a] Bulk-polymerizated polystyrene (2% pTp + 0.05% POPOP), IHEP, Protvino, Russian Federation.
[b] PSM-115-based polystyrene made by injection into the mold technology (2% pTp + 0.03% POPOP), IHEP, Protvino, Russian Federation.
[c] Nuclear Enterprises Ltd., Edinburgh, Scotland.
[d] Bicron Corp., Newbury, Ohio, USA.

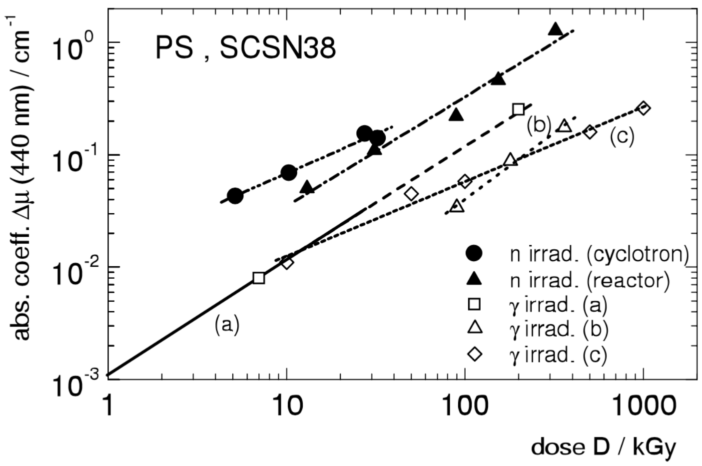

Figure 7.8: Radiation-induced optical absorption coefficients at 440 nm [55].

Light Yield The light yield of scintillating fibers decreases by irradiation. Table 7.2 shows the light yield of various scintillators after irradiated by the gamma ray. In our case the dose is 1.5×10^4 Gy at the center fiber, and the irradiation source is negative pions, which makes it difficult to directly compare them with each other. If it is assumed that the radiation effect by negative pions is not so much different from that of gamma rays, the light yield of BC series scintillators will be 60% even after suffering from twice larger dose.

Transmittance Figure 7.8 shows the radiation effect to the absorption coefficient of a scintillator for the neutron and the gamma ray. The fraction of light which reaches the end of the scintillator after 5 years run was calculated using the absorption coefficient. More than 40% of light can be detected after propagating 10 cm even after the irradiation.

Effect on Signal Size The initial performance of the photon detection is estimated using the energy deposit and the transmittance. The number of photon N_{pho} is written as follows;

$$N_{\text{pho}} = W \cdot E \cdot \frac{\Delta\Omega}{4\pi} \exp\left(-\frac{d}{\lambda}\right) \cdot PDE, \tag{7.1}$$

where $W \sim 8,000$ photons/MeV [56] is the scintillation performance of the scintillating fiber, $E \gtrsim 0.2$ MeV is the energy deposit on the scintillator, $\Delta\Omega/4\pi \sim 7\%$ is the fraction of the solid angle looking into SiPM, $d < 10$ cm is the distance between the scintillation position and the sensor, $\lambda \sim 15$ cm [56] is the attenuation length of the fiber, and $PDE \sim 40\%$ [40] is the photon detection efficiency of the SiPM. The solid angle was calculated assuming the photons are generated at the end of a $5 \times 5 \times 100$ mm^3 scintillator, and only those directly reach a SiPM at the other end of the bar are considered. About 23 photons are expected to be detected. Even after the experiment of 50 days, more than 10 photons can be detected based on the radiation damage estimation above and it is large enough to distinguish signals from dark noise.

SiPM

The radiation damage on SiPM can be classified into two types: ionizing process and bulk damage.

Ionizing Process When SiPM is irradiated with ionizing particles such as gamma rays, the p-n structure changes and leak current increases. A significant increase of leak current after 160 Gy/h gamma ray irradiation is reported in Ref. [32]. In our case, the width of the pion beam is about 8 mm in sigma and if the length of a scintillating fiber is 100 mm, almost no beam particles enters SiPM directly. Then only possible ionizing particle is a gamma ray from a pion decay. The expected dose on the silicon is calculated and it is only 0.48 Gy after 50 days calibration. Thus this effect will be negligible.

Bulk Damage The other type of damage is called bulk damage and it is induced typically by neutron. The increase of dark noise caused by 53 MeV proton is reported in Ref. [57] and the broadening of the one photoelectron peak was observed after 9.1×10^9 1 MeV-n_{eq}/cm^2.

In order to estimate the radiation level of the neutron in our case, the energy spectrum of the neutron was simulated. The kinetic energy of the neutron generated in the CEX reaction is 420 keV, and the energy distribution after 25 mm flight in the liquid hydrogen target is like Fig. 7.9. $10^{9\text{-}10}$ 1 MeV-n_{eq}/cm^2 is expected during the calibration run of 50 days, and it will worsen the energy resolution. In our case the precise energy is not required to distinguish a signal hit from background. Thus the worsening of the resolution in this level is not a problem.

7.4 Active Target

The beam monitor can provide information of the beam position only in the plane perpendicular to the beam axis, and cannot provide the information on z position of the vertex,

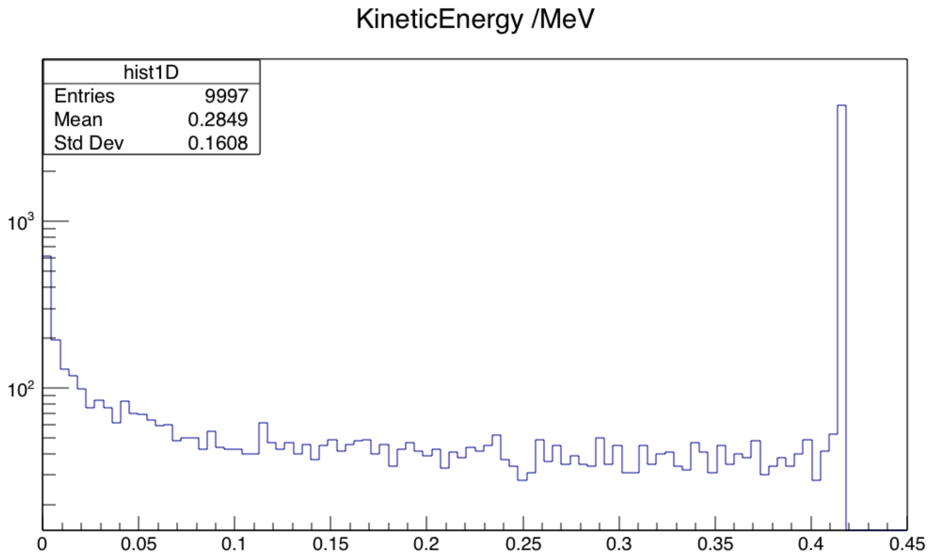

Figure 7.9: Energy distribution of the neutron generated by charge exchange reaction after the flight of 25 cm, simulated by Geant4.

which is most important for the energy estimation because it is sensitive to the opening angle of two gamma rays. An active target is one solution which makes it possible to measure the vertex position along the beam axis. By replacing the passive liquid hydrogen target by an active scintillating target, three dimensional position information of the vertex can be extracted.

7.4.1 Concept

The detector concept is depicted in Fig. 7.10. The basic idea is shared with the scintillating fiber beam monitor. It is made of some layers and each layer detects only the one-dimensional position. The significant difference is that each layer is designed to be thick so that the charged pion can stop in the scintillator while the beam monitor was designed to be thin enough not to affect the beam.

The detector performance is compared with the case of using scintillating fiber beam monitor, for the case where the width and the thickness of the scintillating materials are 5 mm. The result is summarized in Tab. 7.3. Not only the timing estimation but also the energy estimation improves thanks to the capability of estimation of the position along the beam axis.

The radiation hardness of the plastic scintillator is similar to that of the scintillating fiber, while the light yield is larger thanks to the large thickness.

On the other hand, there are two possible disadvantages discussed below.

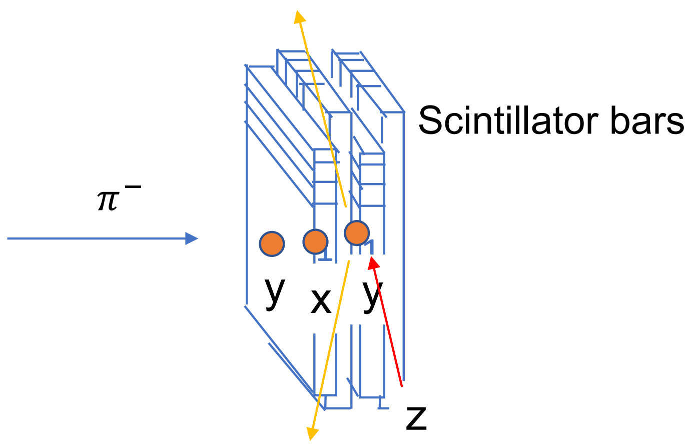

Figure 7.10: Design of an active target. Each layer is thicker than the scintillating fiber and some layers are piled up to obtain the position along the beam axis.

Table 7.3: Performance of the estimation of the gamma ray timing and energy using different type of detectors.

Detector type	Timing	Energy
No Detector	73 ps	320 keV
Scintillating Fiber	51 ps	300 keV
Scintillating Target	39 ps	230 keV

7.4.2 Charge Exchange Reaction in Scintillator

While the liquid hydrogen target consists of purely hydrogen atoms, a scintillator contains carbon atoms. Therefore, the reaction of the charged pions in the target is different. The negative pion causes two types of reaction in a scintillator.

The first one is coherent reaction [58]. A stopped negative pion is captured by a molecule which consists of C and H with probability proportional to Z^{-1}, where Z indicates the atomic number. Then the captured pion moves from a molecular orbital to an atomic orbital. This probability is proportional to Z^2, which means that the probability that the pion moves to the hydrogen orbital is 100 times smaller than that to the carbon orbital. The CEX reaction does not happen in a pionic carbon owing to the energy difference between the carbon and the boron. This will probably result in a significant decrease of the reaction rate.

The second type is incoherent reaction. The moving pion can directly collide with a nucleus with small probability. When a moving pion causes CEX reaction with a proton in the carbon nucleus, the momentum of generated neutral pion is no more 28 MeV/c because the negative pion is moving and the proton has Fermi momentum in the carbon atom. The different momentum of the neutral pion leads to the different energy of the gamma ray. This might result in changing the energy spectrum of the gamma ray.

7.4.3 Rate

The rate of the charge exchange reaction on various materials has been studied as shown in Fig. 7.11. It shows the probability of a pion charge exchange reaction on different materials compared to that on liquid hydrogen. When using CH_2 as target material, the probability of reaction becomes around 1% of that with liquid hydrogen target. The minimum rate of the charge exchange reaction on CH_2 which has been found in the literature is 0.77% of that on liquid hydrogen [60], and the maximum is 1.45% [61]. In the MEG experiment, the DAQ rate of the charge exchange calibration with a LH_2 target was 12.5 Hz and it took 2.5 hours to store the necessary statistics for a particular region defined as a patch. The decrease of the probability of the charge exchange reaction demands 250-500 hours with an active target and it is unreasonable. However, in the charge exchange calibration of the MEG experiment, the beam rate was intentionally reduced to prevent from pileups and radiation damage on detectors. By fully opening the beam slit, 20 times larger beam rate can be obtained. It improves the reaction rate up to 1.5-3 Hz, which leads to 10-20 hours/patch. Although it is still longer, it is worth investigating more because it is instead possible to save the target preparation time which is necessary in the liquid hydrogen target case. The cumbersome low temperature operation is not needed anymore with the scintillator active target.

7.4.4 Energy Spectrum

The active target for the pion charge exchange reaction has been already used in the MEGA experiment [62]. Fig. 7.12 shows the energy spectrum obtained in the MEGA experiment using a scintillating target. The tail events in the low energy region is explained as the charge exchange reaction in flight on carbon nuclears, and the tail in the large energy region is explained as events which have small opening angle. High energy tail can be eliminated by

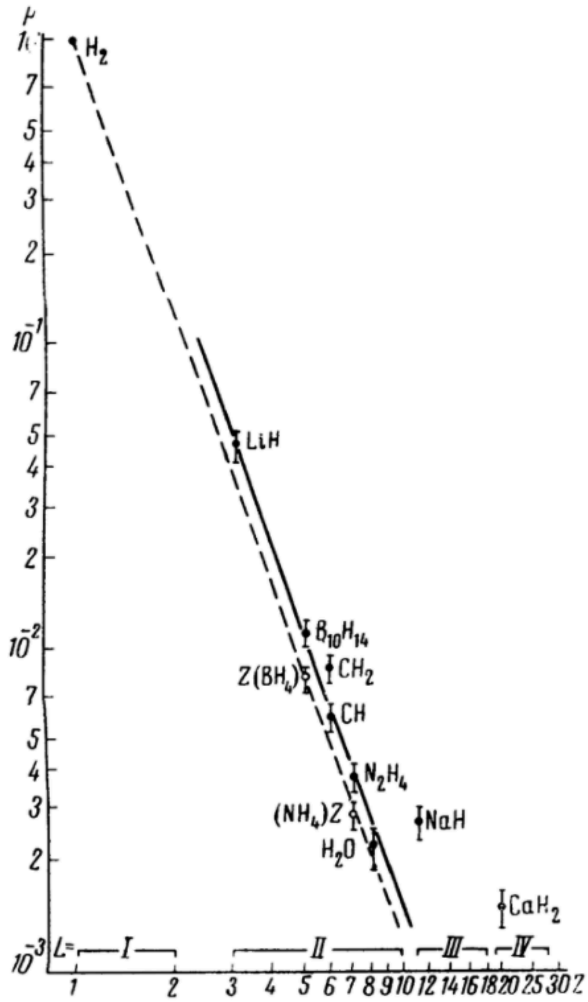

Figure 7.11: Probability of a pion charge exchange reaction on different materials compared to that on liquid hydrogen [59]. The probability of the reaction is around 1% of that on liquid hydrogen target when using CH_2 as a target.

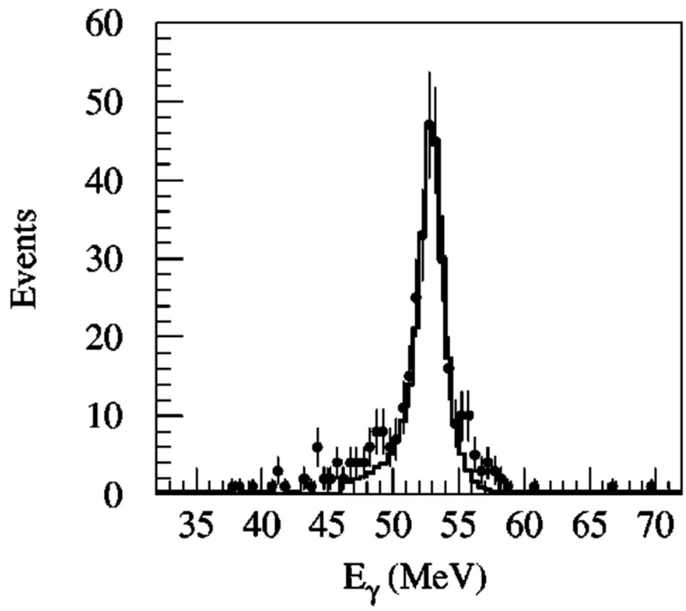

Figure 7.12: Energy spectrum of reconstructed photons which converted in the outer layer in the MEGA experiment [62]. The points come from data and the solid line shows reconstructed energy from simulated events.

the improved angle reconstruction owing to the vertex information. The lower energy events coming from the CEX reaction on carbon nuclears cannot be separated from those due to detector response. It disturbs the extraction of the detector response function, and need to be investigated by experimental test.

7.5 Test of Active Target

In the previous two sections, two types of vertex detectors were considered. The active target provides more precise estimation of the properties of the gamma ray although it has two possible disadvantages. In order to investigate the possible problems, a test experiment was planned to be conducted in December 2019.

7.5.1 Purpose

The main purpose is to check the rate of gamma ray from the charge exchange reaction with an active target, and to compare the energy spectrum with that obtained from the normal liquid hydrogen target. In addition, the improvement of the timing and energy estimation should be confirmed using the vertex reconstruction.

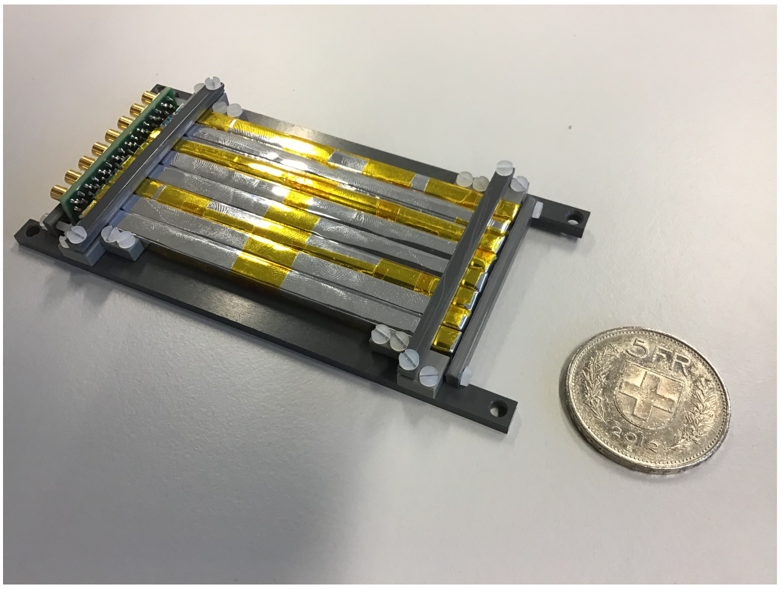

Figure 7.13: One layer of the active target before wrapped by shading cloth.

7.5.2 Construction of Prototype

In order to achieve these purposes, a prototype target has been developed. Figure 7.13 shows one layer of the constructed target. The support structure is made of plastic, and it can fix the scintillators in three dimensions. Plastic scintillators EJ-232 provided by Eljen [63] cut into pieces with a size of 90 mm $\times$ 4.8 mm $\times$ 4 mm are used as a scintillating target.

The scintillation photons are read out by a SiPM attached at the end of the scintillator, which is optically connected by optical cement. One layer consists of eight scintillators and they are optically separated by reflectors (3M ESR, 65 μm-thick [64]) with each other. The SiPMs are only at one end to reduce the number of readout channels, and the other end is covered by the reflector. Four layers are stacked up to provide enough material to stop the pion beam. Each layer is wrapped by shading cloth. In front of first layer, a degrader made of 3 mm thick aluminum is placed. The thickness of the degrader was determined by a flight length simulation shown in Fig. 7.14.

7.6 Conclusion

Obtaining information on the position of the neutral pion decay vertex leads to better estimation of the energy and timing of the gamma ray entering the LXe Calorimeter, resulting in more precise calibration and performance estimation. Two different types of modules were considered as a vertex position detector, the scintillating fiber beam monitor and the plastic scintillator active target, and the performance and the radiation hardness were inspected. The active target provides the position information along the beam axis although there are some possible disadvantages which should be tested experimentally. A prototype of the

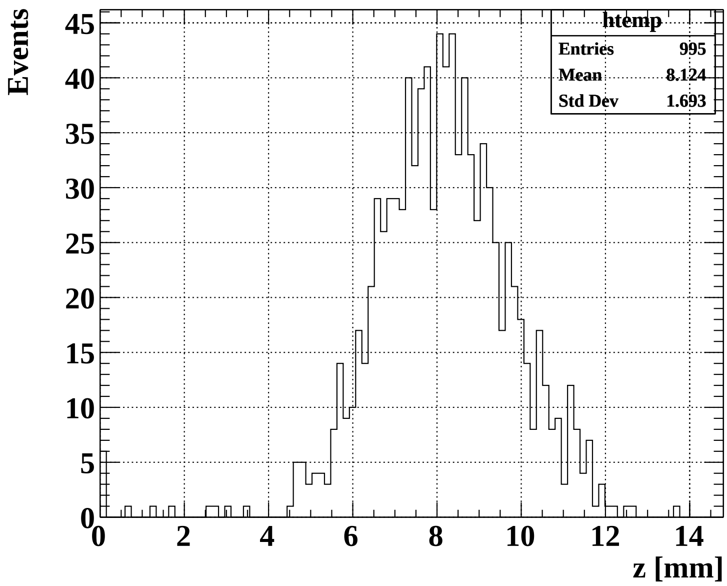

Figure 7.14: Simulated flight length of the negative pion in the plastic when a 3 mm thick Aluminum degrader is placed in front of the scintillators.

active target has been developed for the test experiment which was planned in December 2019, although the test was postponed on account of a failure of a beam transport solenoid. It will be repaired and the test of the active target is planned in 2020.

Part IV

Conclusion

Chapter 8

Conclusion

Several studies concerning the calibration of the LXe Calorimeter were conducted. The photosensors were successfully calibrated and monitored during the pilot runs. The new calibration methods of the photosensors and the new detector for the coming CEX calibration have been studied, which are expected to contribute to the more convenient or precise calibration after some more sophisticated studies.

8.1 SiPM Gain Monitoring

Two independent methods of monitoring the gain of SiPMs were studied to compensate for some disadvantages of the standard method. One method uses a statistical property of the charge distribution from a Poisson light source. It has an advantage in the robustness to noise, and the gain can be measured even after heavily irradiated where usual one-photoelectron method cannot be applied, although a conversion factor has to somehow be obtained to calculate the absolute gain. The behavior of the statistics was different from expected one, but the gain was successfully extracted.

The other method extracts gain-related information directly from the waveform and it does not need special setup for measuring the gain. Although this method was originally developed for PMT gain monitoring in the previous study, it was successfully applied to SiPMs in this study with a method improved by taking into account the effect of overlapping waveforms.

The gain extracted by these methods is confirmed to be highly correlated to the one obtained from the standard one-photoelectron method. However, it must be checked that changes in other properties such as afterpulsing does not affect these methods, and it would be the next step to do.

8.2 PMT Monitoring during Pilot Run

The PMT response was monitored during the MEG II pilot runs conducted in 2018 and 2019. The effects of high rate muon beam were especially carefully investigated because the beam rate is more than twice larger than in the MEG experiment. The response to alpha rays was calibrated with 4% precision channel by channel, and the precision of the average of 350 PMTs was 0.2%, which fulfills the requirement. The response to LED light was calibrated with 1% precision channel by channel, and the variation of response to LED light caused by aging seems correlated with that to alpha rays. The gain decrease by the muon beam irradiation was found to be severer than expected from the experience in the MEG experiment, but a solution of lower gain operation was found out to be effective. The effect of the lower gain operation on the detector performance will be investigated by a calibration run with the CEX reaction in 2020.

8.3 Development of Pion Beam Detector

Obtaining information on the position of the neutral pion decay vertex leads to better estimation of the energy and timing of the gamma ray entering the LXe Calorimeter, resulting in more precise calibration and performance estimation. Two different types of modules were considered as a vertex position detector, the scintillating fiber beam monitor and the plastic scintillator active target, and the performance and the radiation hardness were inspected. The active target provides the position information along the beam axis although there are some possible disadvantages which should be tested experimentally. A prototype of the active target has been developed for the test experiment which was planned in December 2019, although the test was postponed on account of a failure of a beam transport solenoid. It will be repaired and the test of the active target is planned in 2020.

Acknowledgement

First, I want to thank Prof. Toshinori Mori for giving me the chance for this study. I had a precious experience of taking part in an international collaboration locally at PSI and studying together with overseas researchers. He gives us essential comments at the right time and makes us collaborators brace ourselves. Prof. Wataru Ootani has given me important advice in every meeting. I am grateful of his equal interest to all the studies of students and pointed questions. Dr. Toshiyuki Iwamoto has given me kind support both on research and on life in Switzerland. He always kindly answers my questions despite being very busy with work as a run coordinator. Dr. Yusuke Uchiyama always points out critical points I missed in my study. I was often moved by his presentations or questions which get straight to the point. I always rely on Dr. Kei Ieki for technical support both in hardware and software. I respect that he tries a lot of new ideas himself while paying attention to students' work. Mr. Shinji Ogawa, Mr. Satoru Kobayashi and Ms. Rina Onda were necessary for proceeding my study. I could not have conducted my study at all without their kind support.

Dr. Satoshi Mihara gave me important insight on the PMT gain decrease and the pion charge exchange reaction ina scintillator. Dr. Peter-Raymond Kettle, Dr. Giovanni Signorelli and Dr. Angela Papa provided me necessary information on making a prototype target. Dr. Akos Schreiber and Dr. Florian Barchetti made a support on making the target. The discussion with Mr. Kosuke Yanai and Mr. Atsushi Oya was necessary on the SiPM gain study, and they have also always supported me as good friends.

I want to thank the member of the laboratory, Dr. Miki Nishimura, Mr. Mitsutaka Nakao, Mr. Masashi Usami, Mr. Linghui Liu, Mr. Nobuo Matsuzawa, Mr. Naoki Tsuji, Mr. Tatsuro Torimaru, Mr. Kohei Shimada, Mr. Taku Yonemoto, Mr. Kensuke Yamamoto and Mr. Ryunosuke Masuda, for advice in the meeting and for enjoyable research life. I would like to thank all the people in the MEG II collaboration and my friends in Japan and Switzerland.

Finally I would like to thank my family for accepting my decision in studying abroad and for their warm support throughout my life.

Bibliography

[1] Y. Fukuda et al. (Super-Kamiokande Collaboration), Evidence for oscillation of atmospheric neutrinos. Phys. Rev. Lett. **81**, 1562–1567 (1998). doi:10.1103/PhysRevLett.81.1562. https://link.aps.org/doi/10.1103/PhysRevLett.81.1562

[2] CERN website. https://home.cern/science/physics/standard-model, cited 22nd December 2019

[3] Y. Fukuda et al., Evidence for oscillation of atmospheric neutrinos. Physical Review Letters (1998). doi:10.1103/PhysRevLett.81.1562, arXiv:9807003

[4] European Strategy for Particle Physics Preparatory Group, Physics Briefing Book (2019). arXiv:1910.11775. http://arxiv.org/abs/1910.11775

[5] S. Kobayashi. Research on precise gamma-ray position measurement with MEG II liquid xenon detector. Master's thesis, The University of Tokyo (2019). https://www.icepp.s.u-tokyo.ac.jp/download/master/m2018_kobayashi.pdf

[6] S. M. Bilenky, S. T. Petcov, B. Pontecorvo, Lepton mixing, $\mu \rightarrow \mathrm{e} + \gamma$ decay and neutrino oscillations. Physics Letters B (1977). doi:10.1016/0370-2693(77)90379-3

[7] L. Calibbi, G. Signorelli, Charged Lepton Flavour Violation: An Experimental and Theoretical Introduction. Riv. Nuovo Cimento **41** (2017). doi:10.1393/ncr/i2018-10144-0, arXiv:1709.00294. https://arxiv.org/abs/1709.00294

[8] The MEG Collaboration et al., Measurement of the radiative decay of polarized muons in the meg experiment. The European Physical Journal C **76**(3), 108 (2016). doi:10.1140/epjc/s10052-016-3947-6. https://doi.org/10.1140/epjc/s10052-016-3947-6

[9] M. Tanabashi et al., Review of Particle Physics. Physical Review D **98**(3), 030001 (2018). doi:10.1103/PhysRevD.98.030001. https://link.aps.org/doi/10.1103/PhysRevD.98.030001

[10] A. M. Baldini et al., The design of the MEG II experiment. The European Physical Journal C **78**(5), 380 (2018). doi:10.1140/epjc/s10052-018-5845-6. https://doi.org/10.1140/epjc/s10052-018-5845-6

[11] A. M. Baldini et al., Search for the lepton flavour violating decay $\mu^+ \rightarrow \mathrm{e}^+\gamma$ with the full dataset of the MEG experiment. The European Physical Journal C **76**(8), 434 (2016). doi:10.1140/epjc/s10052-016-4271-x. https://doi.org/10.1140/epjc/s10052-016-4271-x

[12] PSI website. https://www.psi.ch/en, cited 22nd December 2019

[13] A. M. Baldini et al., Muon polarization in the MEG experiment: predictions and measurements. The European Physical Journal C **76**(4), 223 (2016). doi:10.1140/epjc/s10052-016-4047-3. https://doi.org/10.1140/epjc/s10052-016-4047-3

[14] J. Adam et al., The MEG detector for $\mu^+ \rightarrow e^+\gamma$ decay search. European Physical Journal C (2013). doi:10.1140/epjc/s10052-013-2365-2, arXiv:1303.2348

[15] S. Ritt, The DRS chip: cheap waveform digitizing in the GHz range. Nuclear Instruments and Methods in Physics Research Section A: Accelerators, Spectrometers, Detectors and Associated Equipment **518**(1), 470 – 471 (2004). doi:https://doi.org/10.1016/j.nima.2003.11.059. http://www.sciencedirect.com/science/article/pii/S016890020302922X

[16] MIDAS webpage. https://midas.triumf.ca/MidasWiki/index.php/Main_Page, cited 22nd December 2019

[17] G. Cavoto et al. A photogrammetric method for a periodic monitoring of the target position in MEG-II. Technical report, MEG II colaboration (2018)

[18] M. Nishimura, Positron Timing Mesurement to Seach for Lepton Flavor Violating Decay in MEG II. PhD thesis, The University of Tokyo. https://www.icepp.s.u-tokyo.ac.jp/download/doctor/phD2018_nishimura.pdf

[19] Y. Uchiyama, The MEG II experiment in search of $\mu \rightarrow e\gamma$. in *The APS Division of Particles and Fields Meeting* (2019). https://indico.cern.ch/event/782953/contributions/3441675/attachments/1887140/3111341/APS-DPF2019.pdf

[20] D. R. Lide, Handbook of Chemistry and Physics, 85th. Boca Raton, FL: CRC (2004). https://archive.org/details/B-001-003-529/page/n1019

[21] T. Doke et al., Absolute scintillation yields in liquid argon and xenon for various particles. Japanese Journal of Applied Physics **41**(Part 1, No. 3A), 1538–1545 (2002). doi:10.1143/jjap.41.1538. https://doi.org/10.1143%2Fjjap.41.1538

[22] T. Doke, K. Masuda, Present status of liquid rare gas scintillation detectors and their new application to gamma-ray calorimeters. Nuclear Instruments and Methods in Physics Research Section A: Accelerators, Spectrometers, Detectors and Associated Equipment **420**(1), 62 – 80 (1999). doi:https://doi.org/10.1016/S0168-9002(98)00933-4. http://www.sciencedirect.com/science/article/pii/S0168900298009334

[23] K. Fujii et al., High-accuracy measurement of the emission spectrum of liquid xenon in the vacuum ultraviolet region. Nuclear Instruments and Methods in Physics Research, Section A: Accelerators, Spectrometers, Detectors and Associated Equipment (2015). doi:10.1016/j.nima.2015.05.065

[24] A. Baldini et al., Liquid xenon scintillation calorimetry and Xe optical properties. in *IEEE Transactions on Dielectrics and Electrical Insulation* (2006). doi:10.1109/TDEI.2006.1657967, arXiv:0401072

[25] E. Aprile, T. Doke, Liquid xenon detectors for particle physics and astrophysics. Reviews of Modern Physics (2010). doi:10.1103/RevModPhys.82.2053, arXiv:0910.4956

[26] R. Sawada, A liquid xenon scintillation detector to search for the lepton flavor violating muon decay with a sensitivity of 10^{-13}. PhD thesis, The University of Tokyo. https://www.icepp.s.u-tokyo.ac.jp/download/doctor/phD2008_sawada.pdf

[27] A. Hitachi et al., Effect of ionization density on the time dependence of luminescence from liquid argon and xenon. Physical Review B (1983). doi:10.1103/PhysRevB.27.5279

[28] Hamamatsu Photonics Web page. https://www.hamamatsu.com/, cited 9th December 2019

[29] Y. Nishimura, A Search for the Decay $\mu^+ \to e^+\gamma$ Using a High-Resolution Liquid Xenon Gamma-Ray Detector. PhD thesis, The University of Tokyo. https://www.icepp.s.u-tokyo.ac.jp/download/doctor/phD2010_nishimura.pdf

[30] MPPC handbook. https://www.hamamatsu.com/resources/pdf/ssd/03_handbook.pdf, cited 22nd December 2019

[31] T. Matsumura et al., Effects of radiation damage caused by proton irradiation on Multi-Pixel Photon Counters (MPPCs). Nuclear Instruments and Methods in Physics Research, Section A: Accelerators, Spectrometers, Detectors and Associated Equipment (2009). doi:10.1016/j.nima.2009.02.022, arXiv:0901.2430

[32] T. Matsubara et al., Radiation damage of MPPC by γ-ray irradiation with 60Co. in *Proceedings of Science* (2007). https://www.researchgate.net/publication/293079737_Radiation_damage_of_MPPC_by_g-ray_irradiation_with_60Co

[33] R. Onda. Research and Development on Time Calibration and Background Reduction for γ-ray Detection in MEG II Experiment. Master's thesis, The University of Tokyo (2019). https://www.icepp.s.u-tokyo.ac.jp/download/master/m2018_onda.pdf

[34] S. Ogawa. MEG II 実験のための真空紫外光に感度のある大型 MPPC を用いた高精細読出し液体キセノンガンマ線検出器の開発. Master's thesis, The University of Tokyo (2016). https://www.icepp.s.u-tokyo.ac.jp/download/master/m2015_ogawa.pdf

[35] A. Baldini et al., A radioactive point-source lattice for calibrating and monitoring the liquid xenon calorimeter of the MEG experiment. Nuclear Instruments and Methods

in Physics Research, Section A: Accelerators, Spectrometers, Detectors and Associated Equipment (2006). doi:10.1016/j.nima.2006.06.055

[36] M.-M. Bé et al. *Table of Radionuclides*, volume 5 of *Monographie BIPM-5*. Bureau International des Poids et Mesures, Pavillon de Breteuil, F-92310 Sèvres, France (2010). http://www.bipm.org/utils/common/pdf/monographieRI/Monographie_BIPM-5_Tables_Vol5.pdf

[37] Geant4 webpage. https://geant4.web.cern.ch/, cited 6th December 2019

[38] J. Adam et al., Calibration and monitoring of the MEG experiment by a proton beam from a CockcroftWalton accelerator. Nuclear Instruments and Methods in Physics Research, Section A: Accelerators, Spectrometers, Detectors and Associated Equipment (2011). doi:10.1016/j.nima.2011.03.048

[39] V. Chmill et al., On the characterisation of SiPMs from pulse-height spectra. Nuclear Instruments and Methods in Physics Research, Section A: Accelerators, Spectrometers, Detectors and Associated Equipment **854**, 70–81 (2017). doi:10.1016/j.nima.2017.02.049, arXiv:1609.01181

[40] Hamamtsu Photonics. MPPC S13360 series datasheet (2016). https://www.hamamatsu.com/resources/pdf/ssd/s13360_series_kapd1052e.pdf

[41] A. Oya et al., A comparative study on various methods for SiPM gain calibration. in *Proceedings of the 5th International Workshop on New Photon-Detectors (PD18)*. (Journal of the Physical Society of Japan) (2019). doi:10.7566/PD18, arXiv:https://journals.jps.jp/doi/pdf/10.7566/PD18. https://journals.jps.jp/doi/abs/10.7566/PD18

[42] P. W. Cattaneo et al., Development of high precision timing counter based on plastic scintillator with sipm readout. IEEE Transactions on Nuclear Science **61**(5), 2657–2666 (2014). https://ieeexplore.ieee.org/document/6898046

[43] J. Stein et al., Experiment and modeling of scintillation photon-counting and current measurement for pmt gain stabilization. Nuclear Instruments and Methods in Physics Research Section A: Accelerators, Spectrometers, Detectors and Associated Equipment **782**, 20 – 27 (2015). doi:https://doi.org/10.1016/j.nima.2015.01.101. http://www.sciencedirect.com/science/article/pii/S0168900215001515

[44] S. Kobayashi et al., Calibration of VUV-sensitive MPPCs of MEG II Liquid Xenon Gamma-ray Detector. in *Physics of fundamental Symmetries and Interactions*, number 133 (2019). https://indico.psi.ch/event/6857/contributions/18967/attachments/15252/20923/kobayashi_2019PSI_v2.pdf

[45] F. Yuki, Search for the Lepton Flavor Violating Muon Decay $\mu^+ \to e^+\gamma$ with a Sensitivity below 10^{-12} in the MEG Experiment. PhD thesis, The University of Tokyo. https://www.icepp.s.u-tokyo.ac.jp/download/doctor/phD2013_fujii.pdf

[46] S. Kobayashi, XEC: MPPC PDE & WD2G in PreEng2019. internal meeting report (2020)

[47] W. Ootani et al. Technical Report on the COBRA Magnet. Technical report, MEG Collaboration (2002)

[48] K. Toyoda et al., Study on Aging of Photomultiplier Tubes for MEG II Liquid Xenon Calorimeter. in *Physics of funcdamental Symmetries and Interactions* (2019). https://indico.psi.ch/event/6857/contributions/18974/

[49] D. Kaneko. Internal meeting report (2013)

[50] K. Ieki. Internal meeting report (2019)

[51] D. Kaneko, The final result of $\mu^+ \to e^+\gamma$ search with the MEG experiment. PhD thesis, The University of Tokyo. https://www.icepp.s.u-tokyo.ac.jp/download/doctor/phD2016_kaneko.pdf

[52] K. Toyoda on behalf of the MEG II Collaboration, The Development of a π Beam Position Detector for the Calibration of the MEG II Liquid Xe Detector. in *Japan Physics Society Annual Meeting* (2019). https://kds.kek.jp/indico/event/30559/contributions/112372/attachments/88184/104724/17aK104-2.pdf

[53] G. Rutar, In search of charged lepton flavor violating decays at psi. PhD thesis, ETH Zürich. http://meg.icepp.s.u-tokyo.ac.jp/docs/theses/giada_phd.pdf

[54] Y. Protopopov, V. Vasil'chenko, Radiation damage in plastic scintillators and optical fibers. Nuclear Instruments and Methods in Physics Research Section B: Beam Interactions with Materials and Atoms **95**(4), 496 – 500 (1995). doi:https://doi.org/10.1016/0168-583X(94)00599-0. http://www.sciencedirect.com/science/article/pii/0168583X94005990

[55] B. Bodmann, U. Holm, Neutron-irradiated plastic scintillators. Nuclear Instruments and Methods in Physics Research Section B: Beam Interactions with Materials and Atoms **185**(1), 299 – 304 (2001). doi:https://doi.org/10.1016/S0168-583X(01)00762-5. http://www.sciencedirect.com/science/article/pii/S0168583X01007625

[56] Saint-Gobain Crystals. Fiber product sheet. https://www.crystals.saint-gobain.com/products/scintillating-fiber, cited 22nd December 2019

[57] T. Matsumura, 高感度光検出器 MPPC の放射線耐性. in *Japan Physics Society Autumn Meeting* (2008). http://www.nda.ac.jp/cc/radiation/presen/JPS200809_toru.pdf

[58] S. S. Gershteĭn et al., MESOATOMIC PROCESSES AND MODEL OF LARGE MESIC MOLECULES. Soviet Physics Uspekhi **12**(1), 1–19 (1969). doi:10.1070/pu1969v012n01abeh003914. https://doi.org/10.1070%2Fpu1969v012n01abeh003914

[59] Z. V. Krumshtein et al., INVESTIGATION OF π^--MESON CAPTURE BY HYDROGEN IN HYDROGENOUS SUBSTANCES **27**(6), 906 (1968). http://jetp.ac.ru/cgi-bin/dn/e_027_06_0906.pdf

[60] A. F. Dunaitsev, V. I. Petsukhin, Y. D. Prokoshkin, Measurements of stopped π- meson absorption probability by bound hydrogen nuclei. Il Nuovo Cimento (1955-1965) **34**(3), 521–528 (1964). doi:10.1007/BF02749995. https://doi.org/10.1007/BF02749995

[61] V. Petrukhin, V. Suvorov, Study of atomic capture and recapture of pions minus in mixtures of hydrogen with other gases. Zhurnal Ehksperimental'noj i Teoreticheskoj Fiziki **70**(4), 1145–1151 (1976). https://inis.iaea.org/search/search.aspx?orig{_}q=RN:9355912

[62] M. Ahmed et al. (MEGA Collaboration), Search for the lepton-family-number nonconserving decay $\mu^+ \to e^+\gamma$. Phys. Rev. D **65**, 112002 (2002). doi:10.1103/PhysRevD.65.112002. https://link.aps.org/doi/10.1103/PhysRevD.65.112002

[63] Eljen Technology. Data sheet of EJ-232. https://eljentechnology.com/products/plastic-scintillators/ej-232-ej-232q, cited 9th December 2019

[64] 3M. Vikuiti Enhanced Specular Reflector (ESR). https://www.digikey.ch/Site/Global/Layouts/DownloadPdf.ashx?pdfUrl=AFE70E6B414C436184B8A9900F1C4831, cited 22nd December 2019